Design and Development of a Lab-on-Chip for Biomedical Analysis Based on ElectroWetting On Dielectric Technique

by

Nicola Lovecchio

A thesis submitted
in partial fulfillment of the requirements for the degree of
Doctor of Philosophy in Information and Communications Engineering

at

Sapienza University of Rome

February 2018

Cycle XXX

Author ....
Department of Information Engineering, Electronics
and Telecommunications

Certified by ....
Domenico Caputo
Professor
Thesis Supervisor

This thesis was evaluated by the two following external referees:

Vittorio Ferrari, Professor, University of Brescia, Italy

Valerio Vignoli, Professor, University of Siena, Italy

Design and Development of a Lab-on-Chip for Biomedical Analysis Based on ElectroWetting On Dielectric Technique
Ph.D. thesis. Sapienza – University of Rome

This thesis has been typeset by LaTeX and the Sapthesis class.

Author's email: nicola.lovecchio@uniroma1.it

Dedicated to my love

Abstract

The purpose of this thesis research project has been the development of a compact and versatile optoelectronic platform able to implement all the functionalities needed for a lab-on-chip operation. The project includes also the development of the electronics needed for the control of the system.

In particular, the proposed platform includes three different modules designed for the fluid handling through the ElectroWetting On Dielectric (EWOD) technique, the thermal sample treatment and optical detection. These modules incorporate thin film microelectronic devices (such as photosensors and interferential filters for the optical detection, or heaters and temperature sensors for the sample treatments) on glass substrates connected to the electronic microcontrollers. Moreover, the use of handling techniques which avoid the use of pumps and syringes led to a portable, high-sensitive and low-power consumption lab-on-chip device.

All of the modules have been designed, fabricated and tested separately. Finally, a device integrating all of the functionalities mentioned before has been designed for the development of a multifunctional platform able to perform a "true" lab-on-chip biomolecular system.

Contents

List of Figures

Introduction

This thesis work presents the development of a portable, miniaturized and highly automated lab-on-chip (LoC) for clinical tests, that enables reliable and low-cost point-of-care analysis, and this project involves the amorphous Silicon Devices and Systems Group (aSiDaS) at "Sapienza" University of Rome. In particular, the experiments have been performed at the Laboratory of Microelectronic Technologies and the Characterization Laboratory at DIET-Sapienza (Department of Information, Electronics and Telecommunication Engineering) in collaboration with the Department of Chemistry at Sapienza.

A lab-on-chip [1, 2] is a device that integrates macroscale laboratory functions on a single chip [3], typically from a few millimeters to centimeters in size [4, 5, 6]. These devices arise from the need in the field of biology and chemistry of miniaturization and parallelism in order to improve analysis throughput and sensitivity [7].

The miniaturization of processes was facilitated in the late 1990s thanks to the growth of microfabrication technology [8]. First LoC devices were made of silicon and glass using standard fabrication techniques employed by the semiconductor industry. With the development of new possible applications, the demand for inexpensive materials and simpler fabrication methods grew, and led to the appearance of LoCs built from polymers [9]. Soft lithography with polydimethylsiloxane (PDMS) has become a very popular technique for the fabrication of microfluidic channels, even if glass and silicon are still preferred for commercial or specialized devices thanks to their chemical and mechanical properties [10, 11, 12]. PDMS is a soft elastomer that has been one of the key materials in the development of LoCs because it is optically transparent, inexpensive, chemically inert, and easy to mold [13, 14].

Over the past few decades, many LoC devices and systems have been developed for various chemical and biological applications, such as analyte detection for clinical diagnostics, high-throughput genomic sequencing platforms, chemical screening for drug detection, chemical synthesis, development of a chip-scale platform for cell biology, and tissue engineering. For these purposes, on-chip devices and control schemes for each stage of analysis have been demonstrated [15, 16, 17].

Typical LoC assay processes include the following steps: sample preparation, injection, sorting, reaction, and detection. Biological or chemical samples need to be properly analyzed and prepared before being injected into the device. Then the analytes have to be delivered to a specific location at the desired time through a guided flow. After the controlled reaction of analytes, the products should be interpreted to understand the results. Microfluidic and microelectronic components act as microscale versions of laboratory equipment, and perform each action on a single chip [18]. The implementation of such tools on a chip is still today extensively

studied. Miniaturization and integration are thus two important aspects for successful LoC systems [19, 20, 21].

Miniaturization of chemical and biological processes provides several advantages over macroscale laboratory processes [22]. In fact, miniaturized systems reduce reagent cost and generate less waste because of the small volumes of samples handled. This is particularly advantageous in diagnostics and forensics, where less sample consumption is preferred [23]. Moreover, there is a lower energy consumption owing to the fractioning of a bulk sample into smaller volumes and the subsequent surface-to-volume ratio increase, which provides a smaller heat capacity and faster heating or cooling.

The strength of lab-on-chip devices relies in the integration of multiple functionalities in a single chip [24]. In fact, it is possible to precisely monitor and control operating condition of the device, such as local temperature or analyte concentration, by embedding different functional devices, like a microheater or a flow controller, in a fluidic channel, providing a precision that is very high compared to conventional laboratory equipment [25]. This reduces error, increases uniformity, and allows for precise experiments that are not possible with bulk-scale equipment. Moreover, multiple steps in the analysis, such as sample preparation, reaction, and detection, can be integrated in one device, allowing for massively parallel analysis with automated control, which can reduce user operations. Parallelization greatly increases throughput compared to serial macroscale laboratory processes [26].

Because of their numerous advantages over macroscale processing, LoCs are expected to revolutionize chemistry and biology laboratories in the near future. Additionally, in commercial products, cheap and disposable LoC devices can be manufactured in mass, which could drastically change the drug discovery process by high-throughput screening and provide low-cost point-of-care devices [27]. Eventually, LoC systems can have a large social impact when they are applied to home diagnostics.

Proposed multifunctional platform

The proposed device is a multifunctional platform which integrates on the same chip three different modules for the microfluidics, sample treatment and detection. In particular, microfluidic module considers electrowetting phenomena for the analytes movement; sample treatment deals with a thin film heater and amorphous silicon temperature sensors, while detection is obtained with amorphous silicon photosensors, as it will exhaustively be explained in the following sections.

Microfluidics

The integration level of the LoC devices is constantly growing, and, as a consequence, the number of reaction sites for single chip increase. Within this framework, efficient movement techniques are required. Different approaches have been used during the last few decades, and most of them require extensive equipment reducing LoCs compactness. Among the handling systems that do not require the use of off-chip actuators, as mechanical pumps or syringes, there is the capillarity [28, 29]. A chip based on this technique is easy to develop and to integrate with sensors and actuators usually present on lab-on-chip systems [30], but allows the fluids to

move in only one direction. An alternative that allows to overcome this issue is the ElectroWetting-On-Dielectric (EWOD) method, also known as droplet- or digital-microfluidics[31, 32, 33, 34]. In this technique, an external electric field changes the contact angle of an electrically conductive liquid droplet lying on a hydrophobic surface, modifying the droplet shape and leading to fluidic movement [35].

In literature, there are two possible EWOD configurations, called open and closed electrowetting [36]. The first one, schematically depicted in the figure below, moves the liquid droplets on a single substrate. This configuration does not allow separation of droplets, but only merging, and has some disadvantages including evaporation of solutions. In the closed configuration, the fluid handling occurs between two coupled glasses, and permits, respect to the open one, also the dispensing and the splitting operations [37, 38].
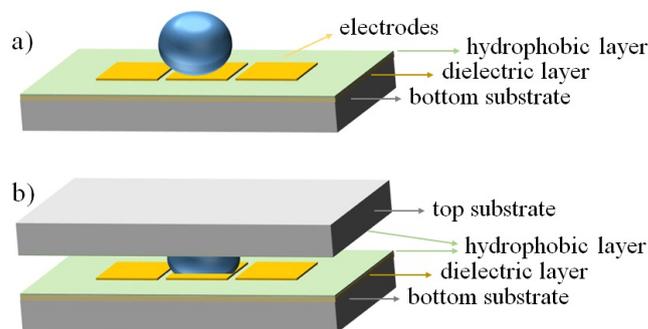
Classical configurations of electrowetting: open (a) and closed (b).

Different solutions have been exploited to couple the two glasses of the closed configuration [39]. Conventionally, a double-sided tape is used as the spacer [40]. The thickness of a layer of the standard commercially available double-sided tape is roughly 50-75 µm and therefore the gap height cannot be easily adjusted to optimize the system performance. Furthermore, since the tape covers only the edges of the substrate, a low viscosity silicone oil is used to avoid fluid evaporation. Oil reduces also the contact angle hysteresis of the droplets and their interfacial tension, making easier the fluidic operations [41]. However, silicone oil complicates fabrication of the EWOD devices since it is difficult to place microfabricated walls around the chip to confine the oil and to fill the reservoirs without introducing air bubbles. This thesis proposes a low-temperature technology relying on the microelectronic definition of the microfluidic channel directly in a top glass and on the microelectronic fabrication of the EWOD electrodes in a bottom glass [42]. With this new approach, the following advantages are obtained: (a) the microfluidic channel is defined exactly by the EWOD electrode geometry avoiding fluid evaporation and dispersion; (b) the height of the microfluidic channel can be precisely controlled and (c) the fabrication and handling is easier and more reliable.

Another advantage of EWOD technique is the possibility to automate the handling and to verify the correctness of the fluid manipulation [43]. This automation can be achieved using sensors that determine the drop position measuring the equivalent capacitance of the EWOD electrode, since the presence of the fluid over the pad increases the capacitance value [44]. This method can be also used to

quantify the volume of each droplet during the dispensing, and then to detach drops of specified size from the reservoir [45].

Finally, this new microfluidic chip based on EWOD technique also allows to integrate thin film sensors and actuator on the external surfaces of the LoC, in order to develop a very compact multifunctional platform suitable for biomolecular analysis.

Sample treatments

Several clinical diagnostics techniques, such as Polymerase Chain Reaction (PCR) or cell lysis, require thermal treatments of the analyte [46], and therefore the temperature control is a critical parameter in managing many physical, chemical and biological applications[47, 48]. The thermal power can be provided by a bulky metal block thermally coupled with the LoC or by an integrated thin film heater. The latter solution is receiving a lot of attention as substitute of the bulky external heaters due to the compactness, which can further improve miniaturization of the devices [49].

The heater temperature could be simply monitored performing a preliminary calibration by varying the driving voltage (or current) of the heater. However, the relation between heater biasing and actual heater temperature depends on environmental conditions (as ambient temperature and/or air fluxes). Another standard on-chip heating approach, which permits to obtain a real time control of temperature, uses a thin metal film (i.e. platinum) as both heater and temperature sensor, taking advantage of the resistance temperature dependence [50, 51]. This method presents many advantages but is limited by the resistance temperature coefficient (TCR) of the heater: for some conductors, the TCR is very low and, in these cases, is hard to obtain a good sensitivity. Furthermore, it is impossible to infer local information as the temperature in different points of the heated area since the resistor variation depends on the average temperature of the whole heater surface. Another technique relies on the integration of thin film temperature sensors and thin film heater in the same LoC [52] to achieve high sensitivity regardless of the heater material [53, 54].

In this context, the chosen approach was the integration on the proposed LoC of hydrogenated amorphous silicon (a-Si:H) p-i-n structure and thin film heaters, combined with a compact electronic board able to drive the heaters and monitor the temperature measuring the drop voltage across the diodes [55, 56]. Indeed, a-Si:H diodes are appealing as thin film temperature sensor since the voltage across them varies linearly with the temperature when they are biased with a constant current, with a sensitivity greater than those found in crystalline silicon [57].

Detection

Optical detection methods, performed by integrated thin film devices, are the most common for LoCs [58]. In particular a-Si:H based devices, which can be used as physical, electronic and optical devices, have received a lot of attention by different research groups for optical biomolecule detection [59, 60], such as stimulated fluorescence detection, optical absorption measurements and chemiluminescence or

thermochemiluminescence detection [61, 62, 63]. The hydrogenated amorphous silicon is one of the most promising materials due to the low deposition temperature (below 300°C) and its physical characteristics prompt the use of this material in different devices such as solar cells, electronic switching, temperature sensors and photosensors [64].

Among the different optical mechanisms, fluorescent molecules are widespread tools for detection and quantification of biomolecules, genotyping and gene expression profiling [65, 66]. They are a golden standard in the clinical and diagnostic fields thanks to their high sensitivity and specificity[67, 68]. These two features make their use very attractive also in LoC systems. However, a system for detection of fluorescence includes a radiation source, a band pass filter for the selection of the excitation wavelength, a long pass filter for the transmission of the fluorescence and simultaneous rejection of the excitation radiations, focusing optics and, finally, a photodetector for the fluorescence quantification. Of course, the presence of all these components reduces the compactness of the system and its effective miniaturization [69]. In order to obtain a fluorescence detection system fully integrated on chip, it is possible to use a thin film interferential filter, which allows to reject the excitation source [70, 71]. This proposed solution, therefore, features a high miniaturization degree thanks to the on-chip detection performed by the a-Si:H photosensors and to the reduced distance between the fluorescent and the detection sites, which avoids the use of focusing optics.

Schematic view of the proposed system

A schematic view of the proposed multifunctional platform, including all the modules previously described, is shown below.
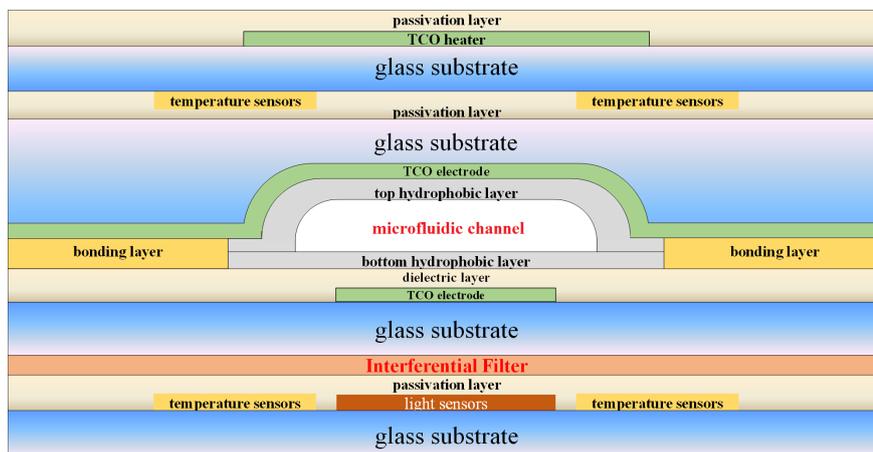
Section view of the proposed device

As it can be seen in the figure, there are four glass substrates constituting the platform: the top one includes a thin film heater and a-Si:H temperature sensors for thermal treatments of the sample; the middle one hosts the microfluidic chamber between two glass chips bonded together; finally, the bottom one integrates the optical detection scheme including photosensors and a thin film interferential filter.

Thesis outline

The thesis is organized into six chapters: Introduction, (1) Electrowetting on dielectric system, (2) Thermal control system, (3) Optical detection system, (4) Final device project and Conclusion.

The *Introduction* presents the state of the art regarding lab-on-chip devices, a brief description of the proposed platform and, finally, thesis outline. *Chapter 1* describes the new handling technique developed to easily integrate sensor and actuator needed to perform biomolecular analysis. *Chapter 2* presents the thermal control system developed to reach temperature stability during sample treatments. In *Chapter 3* the optical detection system is presented. The project of the whole system including all developed modules is described in *Chapter 4*.

Finally the Conclusion summarizes the achievements of the thesis alongside the suggestions for future work.

Chapter 1

Electrowetting on dielectric system

1.1 Classical EWOD configurations

The ElectroWetting-On-Dielectric (EWOD) technique, also known as droplet- or digital- microfluidics, is a movement technique through the changes of the contact angle of an electrically conductive liquid droplet lying on a hydrophobic surface by applying an external electric field.

Thanks to EWOD technology is possible to digitally control the transport of isolated samples of fluid, also favoring operations such as dispensing or mixing. In general, electrowetting allows to switch from a hydrophobic to a hydrophilic status by applying voltage and varying it between a liquid and a solid phase. Control of the degree of wetting, or wettability, of a surface is then possible thanks to the redistribution of the charges and dipoles that, in turn, changes the surface energy of the interface. Varying the surface energy implies a change in surface tension and, hence, a new state of equilibrium that needs a new angle of contact. Modulating the equilibrium, or the angle of contact, by varying the voltage applied permits to render a hydrophobic surface hydrophilic. It is important to underline the fact that there is no electrical current through the fluid. However, the applied voltage could be high depending on the chosen materials leading to associated problems such as electrical breakdown.

Typically, there is a triple interface between two immiscible fluids (i.e. a liquid filling a conduit and the gas that already occupies it) and the walls of the conduit (usually in a solid state, but it could be a third fluid). Each interface has its own surface energy and the wettability depends on the balance of forces acting at the triple phase contact line, as it can be seen in Fig. 1.1. In particular, γ represents an interfacial tension and the subscripts L, V and S stand for liquid, vapor and solid, respectively.

It is important to clarify that it is not necessary to have three different states of matter, as there could be two different liquids and a gas, or three different liquids, etc. As it can be seen, there are three surface tensions, two of them in the same plane and a third one that forms the so called "contact angle" with the solid-liquid interface force. Analyzing the horizontal equilibrium of forces, the *Young's equation*
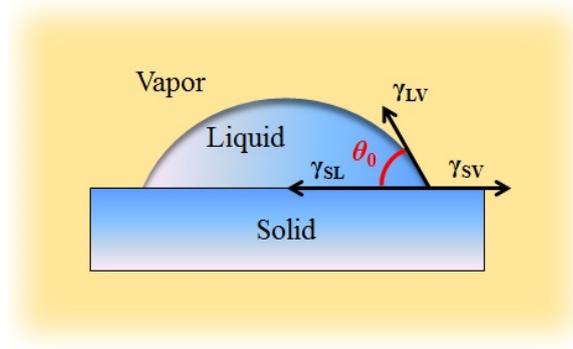
Figure 1.1. Forces acting at the triple interface line.

is reached:

$$\gamma_{SV} - \gamma_{SL} - \gamma_{LV} \cdot cos\theta_0 = 0 \tag{1.1}$$

Since the surface energy in an interface is a physical constant that depends on the nature of the substances involved (it depends on the attraction forces between molecules), the droplet has to change shape and reach the contact angle that permits static equilibrium. Molecules at an interface are subjected to both cohesion forces (molecules attracting each other) and adhesion forces (attraction to the other side surface). Hydrophilic, or wettable, surfaces are characterized by adhesion forces greater than cohesion ones and a contact angle lower than 90°. On the other hand, a hydrophobic, or not wettable, surface experiences cohesion forces stronger than adhesion forces. In this case, the contact angle is greater than 90°.

In an electrolytic solution-metallic electrode interface, a variation of the applied voltage ∂V causes an infinitesimal variation of the surface tension that is expressed as:

$$\partial\gamma_{SL} = -\sigma_{SL} \cdot \partial V \tag{1.2}$$

where σ is the surface charge density and V is the applied voltage.

When applying a voltage to the system, an Electrical Double Layer (EDL, two separated layers on every side of the interface with opposite charges) appears, whose thickness d_{EDL} has an associated specific capacitance given by:

$$C_{EDL} = \frac{\varepsilon_0 \cdot \varepsilon_L}{d_{EDL}} \tag{1.3}$$

In the previous equation ε_L is the relative dielectric constant of the liquid and ε_0 the vacuum's dielectric constant. Integrating equation (1.2), using equation (1.3), the modulable surface tension can be obtained using the next equation:

$$\gamma_{SL} = \gamma_{SL_0} - \frac{\varepsilon_0 \cdot \varepsilon_L}{2 \cdot d_{EDL}}(V - V_0)^2 \tag{1.4}$$

In the previous equation γ_{SL_0} is independent of the applied voltage V, since it refers to the contribution of the surface energy depending only on the chemical contribution. V_0 is the voltage corresponding to null charge. Substituting

equation (1.4) into equation (1.1) the contact angle can be obtained through the
Lippmann-Young equation, where θ_0 is the contact angle when no voltage is applied:

$$cos\theta = cos\theta_0 + \frac{\varepsilon_0 \cdot \varepsilon_L}{2 \cdot d_{EDL} \cdot \gamma_{LV}}(V - V_0)^2 \qquad (1.5)$$

As electrical insulation is desired, a thin dielectric film is placed in between the
electrode and the electrolyte. This kind of electrowetting is known as electrowetting-
on-dielectric and needs higher voltages to operate. In EWOD the electrical double
layer is given by the dielectric thickness, in which neglecting the electric field
penetration inside the liquid, this one can be considered as a perfect electrical
conductor. When studying EWOD V_0 has a zero value and since the dielectric
thickness, d, is much greater than d_{EDL} the capacity per unit of area is much smaller,
so the potential disappears entirely in the dielectric layer. The contact angle can
then be obtained by:

$$cos\theta = cos\theta_0 + \frac{\varepsilon_0 \cdot \varepsilon_L}{2 \cdot d \cdot \gamma_{LV}} \cdot V^2 \qquad (1.6)$$

When voltage is applied to a droplet, through the EWOD effect, there is a change
in the contact angle of a part of the droplet, and therefore a change in its shape. In
this situation, the two different contact angles are unbalanced and the droplet tends
to move in the smaller angle of contact direction because of its lesser charge density.
The droplet will move towards the active electrode looking for an equilibrium state
in which charge density per unit of area is uniform all over the contact surface.

EWOD can be performed in an open configuration (Fig. 1.2a), where the
electrodes are placed only in a bottom wafer, or in a closed configuration (Fig. 1.2b),
where there are electrodes in a bottom wafer and a continuous electrode in a top
plate which acts as the ground connection. Both plates are covered by a hydrophobic
material [72]. In the case of the closed EWOD system, the generated electric field is
stronger than in the open configuration and, thus, it is easier to move the sample
droplets (a smaller voltage is needed).
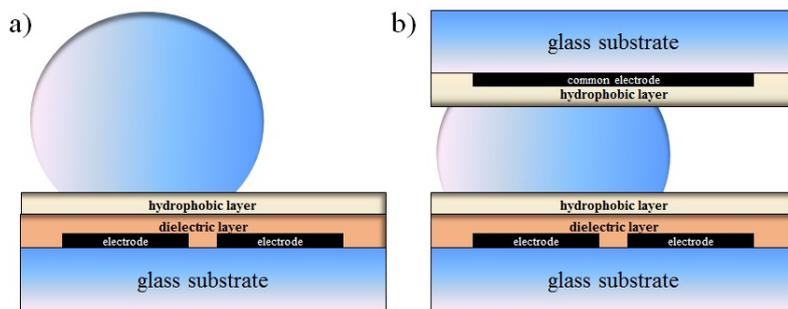
Figure 1.2. Classical configurations of electrowetting: open (a) and closed (b).

Despite its higher complexity, closed configuration provides several advantages,
such as splitting (division of a droplet into two equal ones) or dispensing (separation of
droplets from a reservoir), both needed for lab-on-chip application. Those operations
are not possible in the open configuration owing to the surface tension of the fluid,
which is much smaller when it is included between two plates.

1.2   Electrowetting based microfluidic network

The use of closed EWOD-based lab-on-chip is often laborious due to the necessity of spacers between the bottom and top glasses as well as of oil to confine the solution droplets and to avoid fluid evaporation. In order to overcome these issues, it has been developed a new technology which integrates a closed EWOD configuration inside an all-glass microfluidic network. It relies on the microelectronic definition of the microfluidic channel in a top glass and on the microelectronic fabrication of the EWOD electrodes in a bottom glass. In this way, a very compact EWOD chip suitable for integration of thin film sensors and actuators has been developed [42].

A detailed description of a first developed prototype is reported in the two next subsections.

1.2.1   Device description

The fabricated device (a schematic representation is shown in Fig. 1.3) is a two-glass microfluidic network composed by a central chamber and two reservoirs, either acting as inlet or outlet.
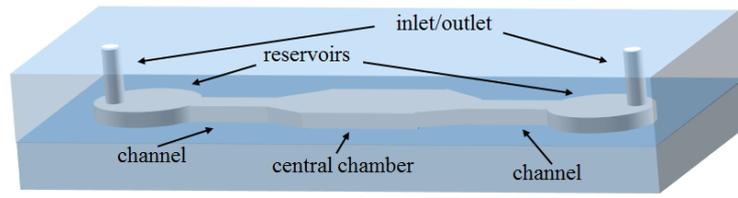
Figure 1.3. Schematic representation of the glass microfluidic network.

Each reservoir has an area of about 50 mm^2 and it is provided with a hole of 1 mm diameter, necessary to fill (or to empty) the structure. The central chamber, instead, has an area of about 60 mm^2. The channels that connect the reservoirs to the chamber are about 5 mm long and 1.2 mm wide. The height of the entire microfluidic network is 100 µm.

The cross section of the system is depicted in Fig. 1.4.
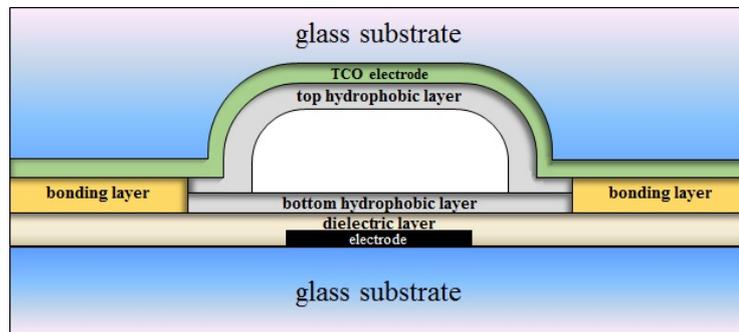
Figure 1.4. Cross section view of the device.

The electrowetting structure is integrated inside the microfluidic network avoiding droplet evaporation without using oil. On the top of the structure there is a common

electrode realized with a transparent conductive oxide (Indium Tin Oxide, ITO), covered by a hydrophobic layer. On the bottom surface of the channel, instead, there is a series of interdigitated electrodes, whose detailed geometry is reported in Fig. 1.5. The distance between two adjacent electrodes is 50 µm. A stack of insulating and hydrophobic surfaces covers the bottom metallic layer, obtaining a classical EWOD structure integrated inside the channel.
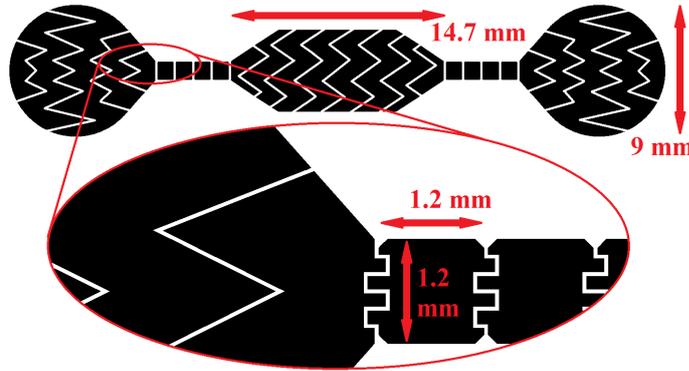
Figure 1.5. Detail of electrodes geometry.

1.2.2 Device fabrication

The developed chip is composed of two glasses (top and bottom) bonded together to obtain a closed configuration. A detailed description of the fabrication is reported below.

1.2.2.1 Bottom glass

The bottom glass is covered by a metallic layer, an insulating surface and a hydrophobic material. The last one has to be present only in the microfluidic network, in order to allow the bonding between the two glasses. A fabricated structure covered by water is shown in Fig. 1.6. The effect of the hydrophobic layer is evident: water covers only the area outside the channels, the chamber and the reservoirs.

Figure 1.6. Bottom glass: water covers the glass except for the electrodes that are covered by the hydrophobic layer.

Fabrication of the bottom glass foresees the following steps:

- glass cleaning using "piranha" solution;

- room temperature vacuum evaporation of a 30/150/30 nm-thick Cr/Al/Cr stacked layer, which acts as bottom EWOD electrode;

- patterning of the metal layer by conventional photolithography (using mask reported in Fig. 1.7a) and wet etching process;

- deposition by spin coating of a 2.6 µm-thick SU-8 3005 (from MicroChem, MA, USA) layer and its pattering to realize the dielectric layer (this layer covers all substrate except the contact pad);

- deposition by spin coating of a 66 nm-thick Teflon AF 2400 hydrophobic layer;

- patterning of the hydrophobic layer by sputter etching technique with argon at 200 W for 15 s (using the physic mask reported in Fig. 1.8).
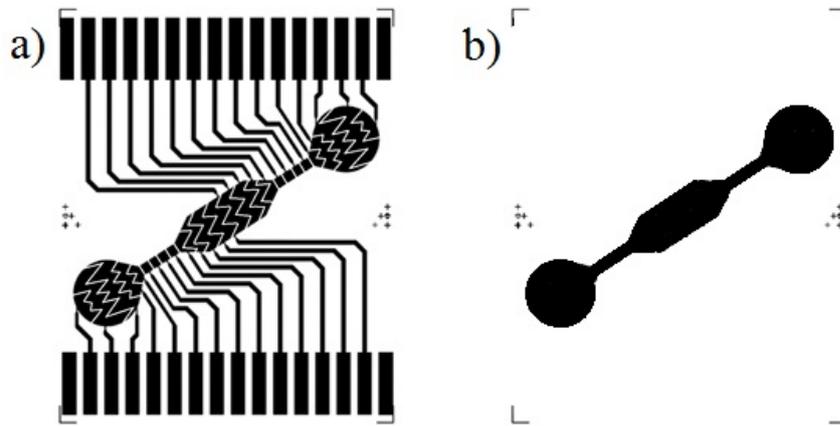
Figure 1.7. Bottom glass masks: electrode (a) and Teflon (b).
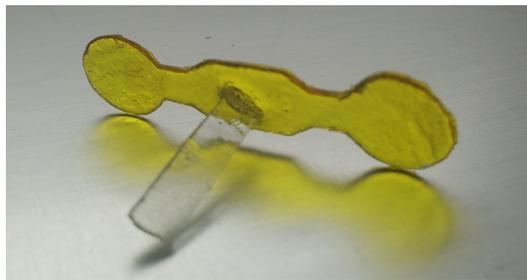
Figure 1.8. Physical mask used for Teflon etching.

During the Teflon baking we have reached the highest temperature process. Indeed, this process requires three steps: 10 min at 110 °C, 5 min at 245 °C and 15 min at 330 °C. High baking temperatures however causes photoresist and SU-8 oxidation and modifies SU-8 dielectric properties. In order to avoid this problem, the baking process was performed in vacuum with nitrogen flow.

1.2.2.2 Top glass

A picture of the top substrate is shown in Fig. 1.9. It hosts the channels, the reservoirs and the central chamber. An ITO layer covered by a hydrophobic surface acts as common electrode.

Figure 1.9. Top glass.

Fabrication of this glass has been implemented with the following steps:

- glass cleaning using "piranha" solution;

- deposition by magnetron sputtering of 30 nm-thick chromium as adhesive layer and 1.35 µm-thick Ti-W alloy layer acting as first masking layer for glass etching;

- deposition by spin coating of a 5 µm-thick SU-8 3005 layer acting as second masking layer;

- patterning of all masking layers by conventional photolithography and wet etching process;

- realization of the inlet and outlet holes using a diamond tip of 1 mm diameter;

- glass wet etching in HF 1:8 DW solution to obtain the 100 µm-height top microfluidic network;

- deposition by magnetron sputtering of 200 nm-thick ITO to realize the common electrode;

- deposition by spin coating of 66 nm-thick Teflon AF 2400 hydrophobic layer;

- patterning of the hydrophobic layer by sputter etching technique with argon at 200 W for 15 s (using, as in bottom glass fabrication, the mask reported in Fig. 1.7b).

Regarding the wet etching of glass, it is reported [73] that the best way to mask the sample is the use of a very thin film of chromium covered by gold. The first layer increases the mask adhesion since it grips very well on glass substrates. In order to lower the cost of this process, we had replaced the gold with the titanium/tungsten (10%–90%) alloy layer. Given the presence of titanium, that does not resist at HF chemical attack, the glass at the end of the process exhibits several trenches in the

masked areas (see Fig. 1.9). However, we found that this issue does not affect the successive technological steps.

The appropriate concentration of hydrofluoric acid has been chosen to obtain an etched surface as smooth as possible. In this way, the etching rate of HF 1:8 DW solution is about 2.3 µm/min. Therefore, the time needed to obtain 100 µm-height channel is about 45 min.

1.2.2.3   Bonding

The final step to complete the structure is the bonding between top and bottom glasses. The bonding is achieved interposing a 5 µm-thick SU-8 3005 layer between them. The detailed processing steps are the following:

- deposition by spin coating of a 5 µm-thick SU-8 3005 on the bottom substrate;

- coupling and alignment of the two glasses;

- soft bake of the structure under load of 2 kg;

- UV exposure;

- hard bake still under load of 2 kg.

During the spin coating deposition, the SU-8 does not adhere on the Teflon layer, leaving unchanged the structure inside the microfluidic network. The complete device is shown in Fig. 1.10.
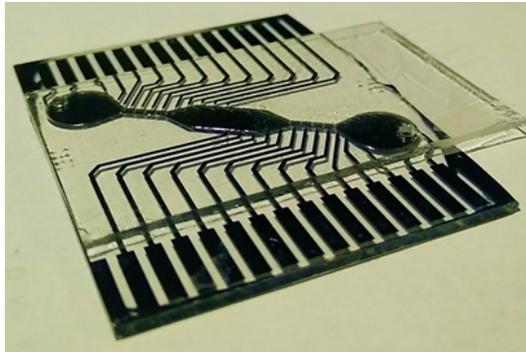
Figure 1.10. Fabricated device.

Developing this new kind of EWOD structure, a complete compatibility of the different technological steps and a very good robustness against mechanical stress have been reached.

1.3   EWOD electronics

The EWOD functionalities are managed by an electronic circuit that generates all the control signals to achieve the droplet movement and detects the presence of the droplet over the electrodes in order to verify the correctness of the fluid manipulation.

1.3.1 Electronics description

The electronic board controls and interfaces the LoC with a computer and it is composed by three main parts connected in a compact and modular system:

- a switching board, hosting a microcontroller, that distributes, in the required time sequence, the voltage to the electrodes;

- a low-power high-voltage generator that, starting from the 5 V of a computer USB connection, generates the voltage (ranging from 10 V up to 250 V) to be supplied to the electrodes;

- an electronic circuit able to perform the localization and the quantification of the fluid.

A graphical unit interface (GUI) developed in C++ controls all the parameters to be sent to the microcontroller through a USB connection.

A picture of the whole EWOD electronic system is shown in Fig. 1.11.
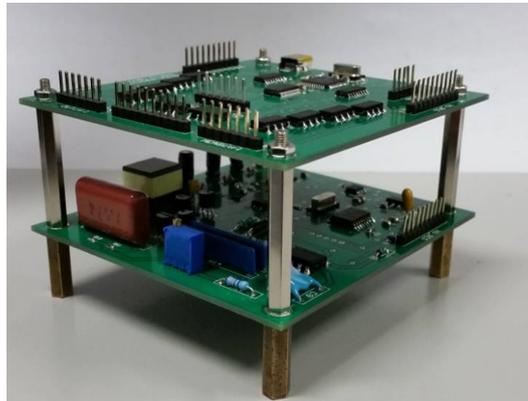
Figure 1.11. EWOD electronic system.

The upper board includes the switching module and the drop position sensing circuit, while the other one is the low-power high-voltage generator.

1.3.1.1 Switching module

The switching board is connected to the EWOD system by means of an edge card connector, which guarantees both electrical continuity between board and glass and the electrical insulation between adjacent contacts when the high voltage, supplied by the variable voltage generator, is applied to the electrodes. The electronic circuit of the main board includes an array of switches (part number AQW210S, GU-E PhotoMOS relay, PANASONIC EW) and a microcontroller (PIC18F4550, Microchip) which rules the switch activation timing, controls the functionalities of the variable voltage generator and handles the data communication with the computer via USB interface. Each electrode of the EWOD device is connected to a couple of switches whose status can be set in order to connect the electrode to high voltage, ground potential or floating potential (Fig. 1.12).

In this scheme, there are four possible combinations:
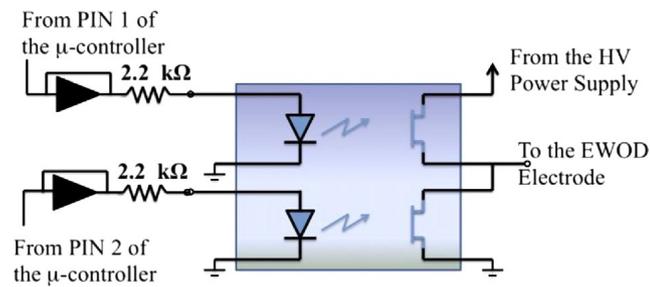
Figure 1.12. Schematic representation of the switches and their driving circuit.

1. if both relays are switched off, the electrode is physically disconnected from both voltage and ground, and is thus in floating configuration;

2. if only relay number 1 is active, the electrode is connected to the high voltage;

3. if only relay number 2 is active, the electrode is connected to the ground potential;

4. If both relays are active, a low impedance path between high voltage and ground is created, resulting in relay failure (unless the current of the external power supply is limited). This configuration must be avoided and managed with the microcontroller software.

As it can be seen in the figure, the output current of each pin has been limited to 1.2 mA by a 2.2 kΩ series resistance.

The Printed Circuit Board (PCB) layer including the switching module is depicted in Fig. 1.13.
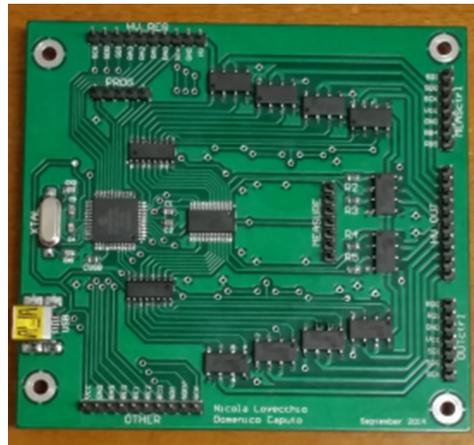
Figure 1.13. Switching module PCB layer.

1.3.1.2 Low-power high voltage generator board

This board generates a voltage from 10 V up to 250 V starting from the standard 5 V USB power supply without exceeding the maximum current consumption of 500 mA allowed by the USB standard.

The first part of the circuit is a flyback converter that raises the 5 V input voltage from a computer USB port up to 300 V. The operating principle of the flyback converter is schematically reported in Fig. 1.14.
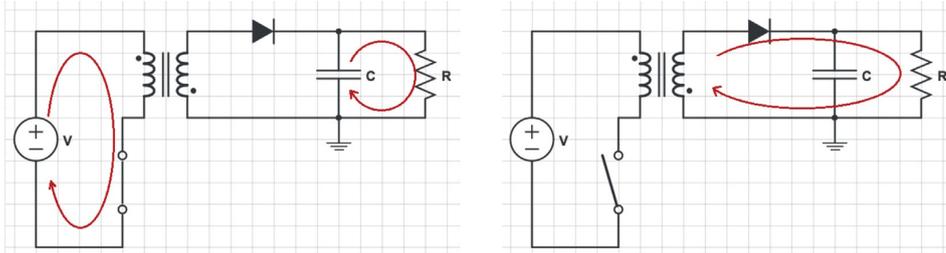
Figure 1.14. Schematic representation of the flyback circuit operation. The voltage generator V is provided by the USB port, while the voltage across the capacitor C drives the EWOD electrodes.

When the switch is closed, the transformer stores the magnetic energy in its primary coil that is instantly transferred to the secondary coil of the transformer when the switch is opened. This effect produces a current pulse that through a rectifier charges the capacitor "C" generating a high voltage drop across the capacitor.

For the design of the flyback converter, an integrated circuit from Linear Technology (part number LT3573) has been chosen. This component is a monolithic switching regulator specifically designed for isolated flybacks and, on its datasheet, is shown the typical applications scheme suitable to obtain 300 V output voltage (Fig. 1.15).
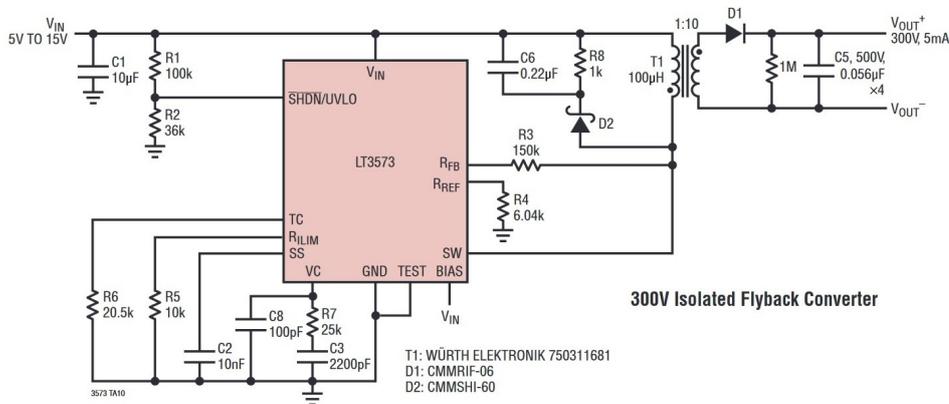
Figure 1.15. Typical application circuit for LT3573 isolated flyback converter.

This scheme has been modified to reduce the input power consumption. In particular, the 1 MΩ resistance in the upper right of Fig. 1.15 has been replaced by a load resistance of 5.1 MΩ in series with a 51 kΩ resistance. This substitution reduces output (and input) current and allows to read the output voltage with an Analog to Digital ADC. In fact, the voltage read on the voltage divider is about a hundred time smaller than the output one, so the ADC won't be damaged. Moreover, three cascaded RC filters (each R value is 1 kΩ and each C value is 100 µF) have been introduced between the power supply and the transformer input pin to prevent the

USB to pull a pulsed current from the primary winding of the transformer. This one, in fact, is driven by a transistor acting as a switch which is continuously switched on and off, thereby generating a pulsed current into the transformer. Finally, the four 56 nF output capacitors have been replaced by one 1 μF ceramic capacitor, whose leakage currents are much smaller than those present in electrolytic capacitors.

The output voltage of the flyback converter is the power supply (Vcc) of the voltage regulator circuit (Fig. 1.16).
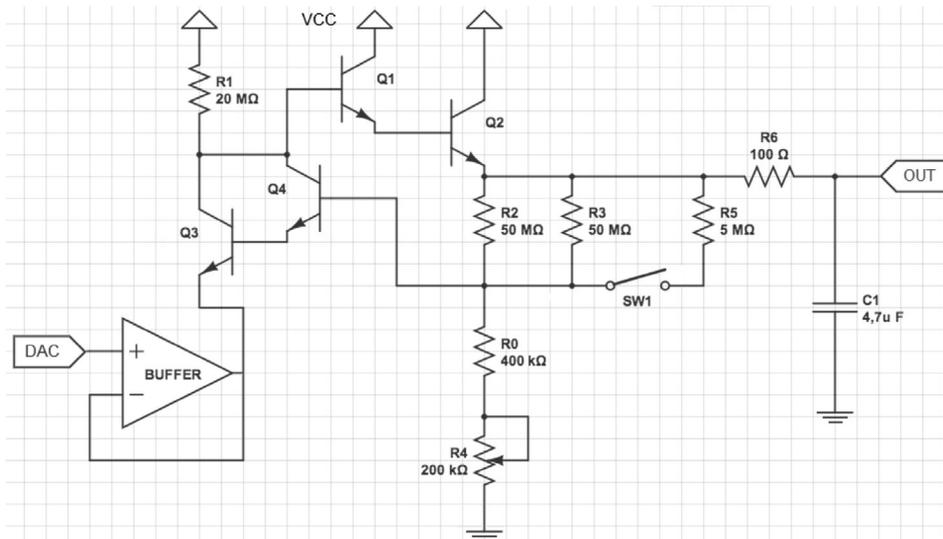
Figure 1.16. Voltage regulator circuit. Vcc is provided by the flyback circuit, while the output voltage (OUT) depends on the DAC output voltage.

This circuit provides an output voltage whose value depends on the output voltage of the Digital to Analog Converter (DAC). The DAC output voltage ranges from 0 to 4.096 V and its value is controlled by the microprocessor included in the switching board through a feedback loop. The actual output voltage value is acquired by the Analog to Digital Converter (ADC) embedded in the microcontroller. It actuates an iterative successive approximation procedure, which changes the value of the DAC voltage until the difference between the required and the actual output voltage is minimized. The required output voltage is set through the GUI.

The operating principle of the voltage regulator circuit is the following. The DAC voltage is buffered to avoid coupling effect with the transistor Q3 and it is reported to the voltage divider made of resistors R0, R4 and R2//R3. The current flowing through the resistors R0 and R4, up to a negligible current driven by the Darlington couple of transistors Q3 and Q4, flows in the resistor R2//R3 and generates the output voltage. The switch "SW1" (see Fig. 1.16) allows to change the gain (V_{OUT}/V_{DAC}) of the circuit by connecting the resistor R5 in parallel with the resistors R2 and R3 and thus changing the value of the voltage divider. Taking into account the value of the resistors reported in the circuit, when the switch is opened the gain V_{OUT}/V_{DAC} is 50.2 and the output voltage range is 45-250 V. When the switch is closed, the gain decreases down to 9.5 and the range is 10-49 V. In conclusion, the output voltage range is 10-250 V with worst-case step of 50 mV and ripple less than 200 mV in the entire range of variation, as will be shown in the

electronics characterization section.

A picture of the low-power high-voltage generator PCB is reported in Fig. 1.17.
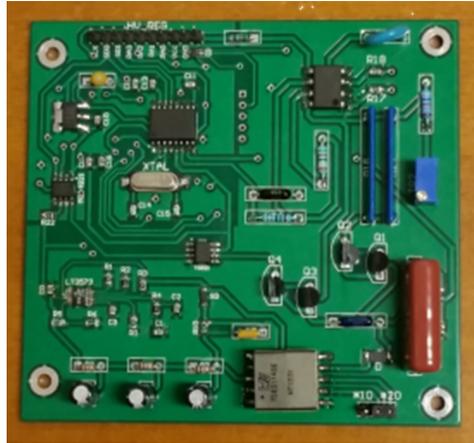
Figure 1.17. Picture of the controlled voltage generator PCB.

1.3.1.3 Drop position sensing circuit

In order to automate the handling and to verify the correctness of the fluid manipulation, it is necessary to know the position of the fluid drops. This automation can be achieved using sensors that determine the drop position measuring the equivalent capacitance of the EWOD electrode, since the presence of the fluid over the pad increases the capacitance value. This method can also be used to quantify the volume of each droplet during the dispensing, and then to detach drops of specified size from the reservoir.

In order to achieve these results, it has been developed an electronic circuit able to perform the measurement of capacitance variations using the "Frequency Shift Oscillator" method, which evaluates the oscillation frequency of an oscillator directly connected to the pad under test. If a droplet is located above the electrode to measure, the oscillator frequency decreases making feasible the localization and the quantification of the fluid [74].

The proposed circuit is shown in Fig. 1.18. Its core is an astable multivibrator composed by the operational amplifier U1 (in trigger configuration), the resistance R and the capacitor $C_{electrode}$, which represents the pad under measurement. Another operational amplifier (U2) decouples the output node from the electrode connection node.

The operational amplifier is the OPA830 (from Texas Instruments). It is a low power, wideband, voltage-feedback amplifier designed to operate on a single power supply (+3 V or +5 V) and it is characterized by high gain bandwidth product (110 MHz) and high slew rate (550 V/µs), that makes it ideal for this application. A PIC18F4550 microcontroller (the same of Section 1.3.1.1) counts the number of rising edges at the output of the circuit, in a 5 ms time window, to calculate the oscillation frequency.

The values of capacitances and resistances of the circuit have been designed considering the maximum frequency of oscillation that the microcontroller can detect
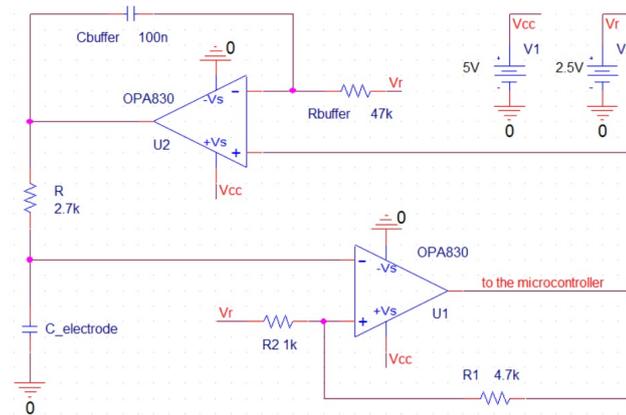
Figure 1.18. Schematic of the circuit sensing the drop position over an EWOD electrode.

(12 MHz) and the minimum capacitance variation to detect for sensing the droplet presence, which is about 1 pF.

Fig. 1.19 shows the electronic board layer of the drop position sensing circuit.

Figure 1.19. PCB layer of the drop position sensing circuit.

1.3.2   Electronics characterization

In this section, the simulation and measurement results are reported.

1.3.2.1   Low-power high voltage generator board

Some numerical simulations of the voltage regulation circuit (Fig. 1.16) have been carried out with OrCad Capture PSpice tool in order to verify its correctness before its fabrication. The input-output characteristic curves of the circuit are shown in Fig. 1.20.

After the physical implementation of the voltage regulation circuit, the ripple measurements have been carried out using a digital oscilloscope. In particular, two
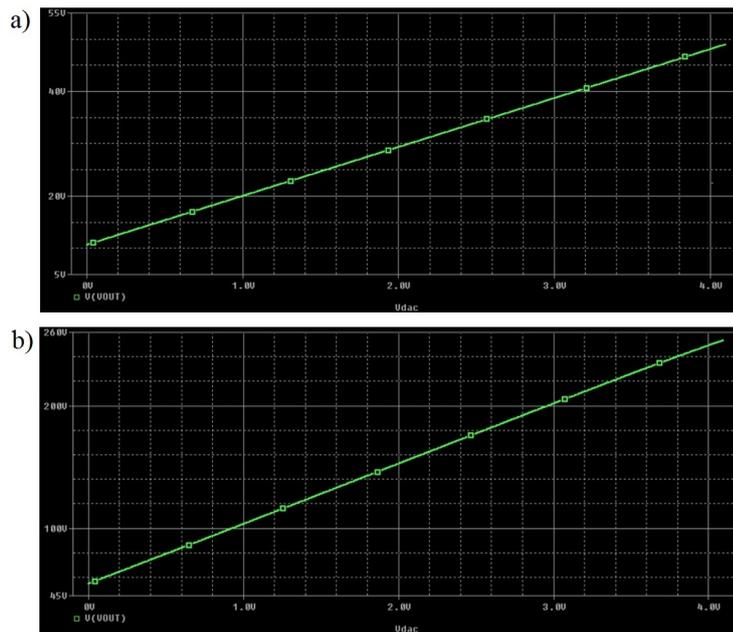
Figure 1.20. Simulated input-output characteristics of voltage regulator: low (a) and high (b) voltage range.

different output voltage values have been chosen (30 V and 200 V) in order to verify circuit behavior at low and high output voltage range.
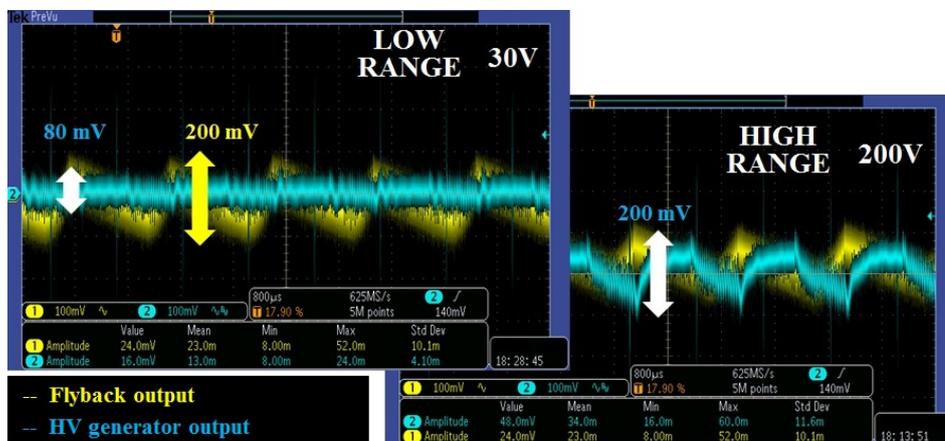
Figure 1.21. Measured ripple at the input and output of the voltage regulator circuit.

The output noise depends from the output voltage: at 30 V, an 80 mV noise is measured, while at 200 V a 200 mV ripple is observed (see Fig. 1.21). This difference is due to the feedback loop gain of the voltage regulator (Fig. 1.16), which decreases when output voltage is increased, so the output noise is not attenuated.

Finally, the output linearity has been verified. The measured input-output curves of the voltage regulator circuits are reported in Fig. 1.22.

The resolution of the employed DAC converter (MCP4821 from Microchip) is of 12 bits over a 4.096 mV range (1 mV precision). Taking into account the curve slope
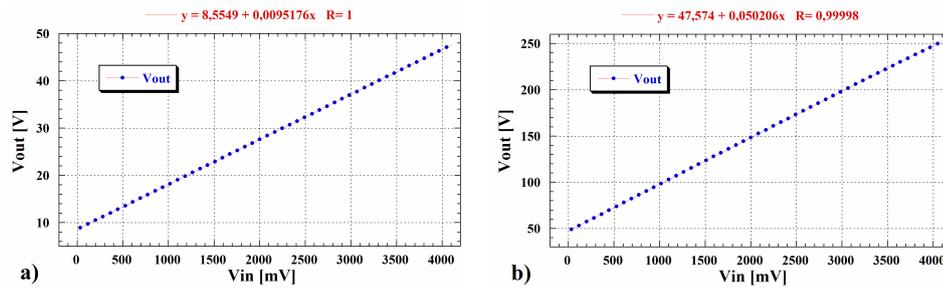
Figure 1.22. Measured input-output characteristics of voltage regulator: low (a) and high (b) voltage range.

values shown in Fig. 1.22, it is possible to obtain the output resolutions, which are 50.2 mV for the high range and 9.5 mV for the low range.

1.3.2.2 Drop position sensing circuit

During design step, the proposed circuit (Fig. 1.18) has been simulated using OrCAD Capture PSpice tool again. The oscillation frequency at output node is calculated through the Fast Fourier Transform (FFT) technique at different values of the electrode capacitance. These ones have been chosen according to typical capacitance values found in EWOD applications and estimating the parasitic capacitances of our measurement setups. An example of PSpice parametric simulation result is shown in Fig. 1.23.
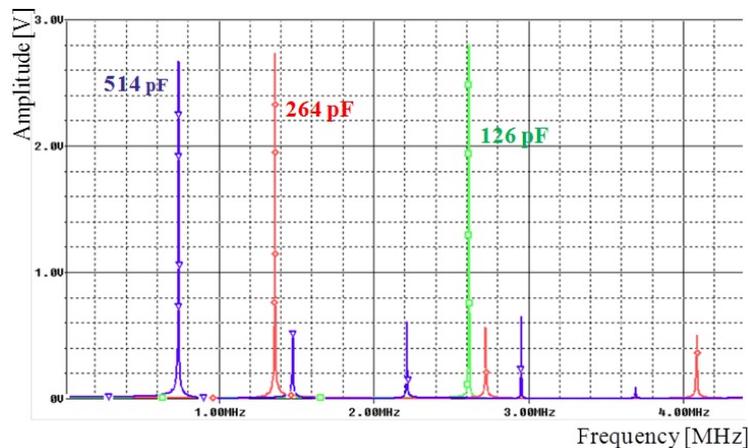
Figure 1.23. Example of PSpice parametric simulation that shows the FFT of the output signals. Higher peaks refer to the first harmonics, evaluated at different load capacitance which are indicated by the corresponding colors.

In particular, the highest peaks in the figure are the first harmonic components of the signal at the output of the operational amplifier U1 of Fig. 1.18. The numbers close to each peak are the corresponding electrode capacitance Celectrode value. The lowest peaks in the figure refer instead to the higher harmonics components of the signals.

To calculate the oscillation frequency at the circuit output, the microcontroller counts the rising edges and sends the obtained values to a PC using the USB connection. The developed GUI shows a real-time graph that represents the oscillation frequency during the measurements (Fig. 1.24). In particular, each step in the figure correspond to a different load capacitance.
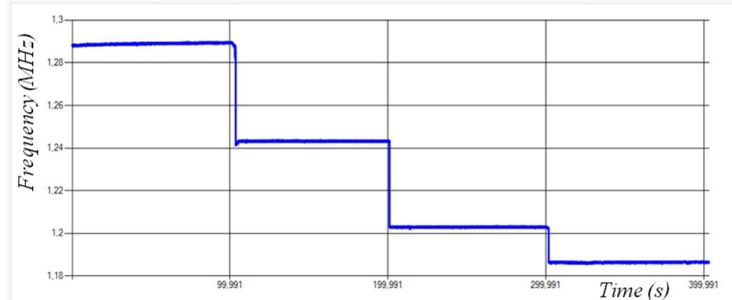
Figure 1.24. The GUI controls the electronic board while a real time graph shows the oscillation frequency during the measurements. Steps inside the figure correspond to different load capacitances.

The results of the measurements performed on the fabricated electronic circuit are shown as symbols in Fig. 1.25. The measured frequencies are determined by the combination of a set of known load capacitances (4.7 pF, 12 pF, 82 pF, 220 pF and 470 pF) and by the undesired parasitic capacitance, which is present at the output of the circuit (44 pF). This parasitic capacitance value has been evaluated by fitting, through simulation of the circuit reported in Fig. 1.18, the measured oscillation frequency in open circuit configuration.
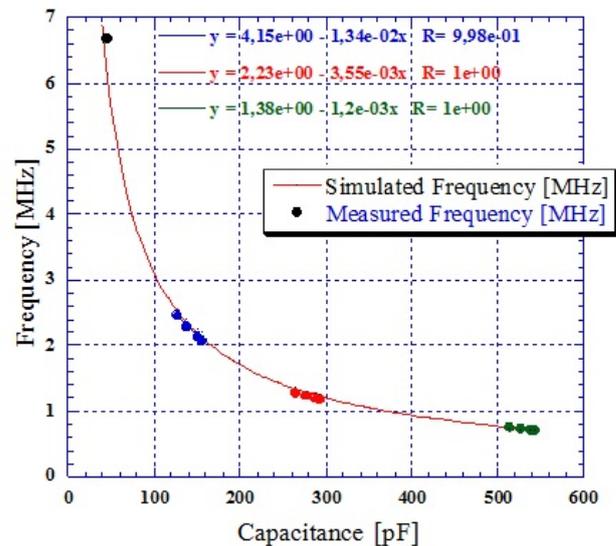
Figure 1.25. Simulated (continuous line) and measured (symbols) frequency as function of capacitance. Equations, indicated by the corresponding colors, are the linear fittings of groups of measured.

Equations inside Fig. 1.25 are the linear fittings of group of measured values.

The correspondence is indicated by the relative colors. The slope of each equation represents the local derivative of the tran-scharacteristic and therefore the sensitivity of the circuit at that specific point. Results show that sensitivity decreases with increasing load capacitance and that, for the investigated capacitance values, the obtained slopes are 13.4 kHz/pF, 3.55 kHz/pF and 1.2 kHz/pF.

In order to calculate the related values of minimum detectable capacitance, we must take into account the minimum frequency variation that the microcontroller can detect. This value is the inverse of the chosen time window, which is 5 ms and corresponds to 0.2 kHz. Dividing this frequency by the achieved sensitivities, we obtain respectively 0.015 pF, 0.056 pF and 0.167 pF. This last value, which represents our worst case, is still low enough for detecting the presence of a droplet over the EWOD electrode.

As can be seen from the calculations just carried out, the minimum detectable capacitance depends linearly on the selected time window. For this reason, the achieved values can be improved at expenses of reduced system speed.

Chapter 2

Thermal control system

This Chapter presents the integration of amorphous silicon (a-Si:H) p-i-n structure and thin film heaters on the same glass substrate combined with a compact electronic board able to drive the heaters and monitor the temperature by measuring the drop voltage across the diodes [55, 56]. All the technologies shown in this Chapter will be integrated with the developed EWOD-based microfluidic system in order to obtain the multifunctional platform that is the aim of this Thesis work.

The developed system, whose block diagram is depicted in Fig. 2.1, is constituted by the following components:

- an electronic board that controls the lab-on-chip temperature;

- a software that controls the electronic circuit board;

- a lab-on-chip device.
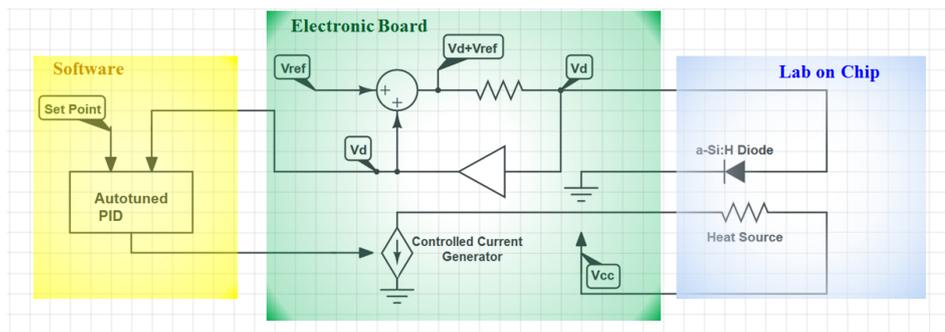
Figure 2.1. Block diagram of the thermal system.

A Graphical User Interface (GUI) controls all of the functionalities of the electronic board. In particular, the setpoint temperature (specified by the user) is achieved using a software Proportional-Integral-Derivative (PID) auto-tuned algorithm, which takes, as input, the temperature inferred by the diode. This is possible since the voltage across the diode varies linearly with the temperature when it is biased with a constant current. The output of the software is then used to provide a controlled current to the heater.

The following sections report the detailed descriptions of the electronic circuit board, the developed PID control and the lab-on-chip device. Finally, the last section describes the obtained experimental results.

2.1 Electronics

The electronic board controlling the whole thermal module includes:

- a power circuit that drives the heater with the current required to achieve the specified temperature;

- a power circuit that drives a fan used to enhance the cooling of the LoC during thermal cycles;

- an electronic circuit that biases the diode at a constant current and measures the diode voltage.

2.1.1 Heater and fan driving circuits

A simple current generator driven by a Digital to Analog Converter (DAC) has been used in order to pilot the thin film resistor. The schematic of this electronic board section is reported in Fig. 2.2.
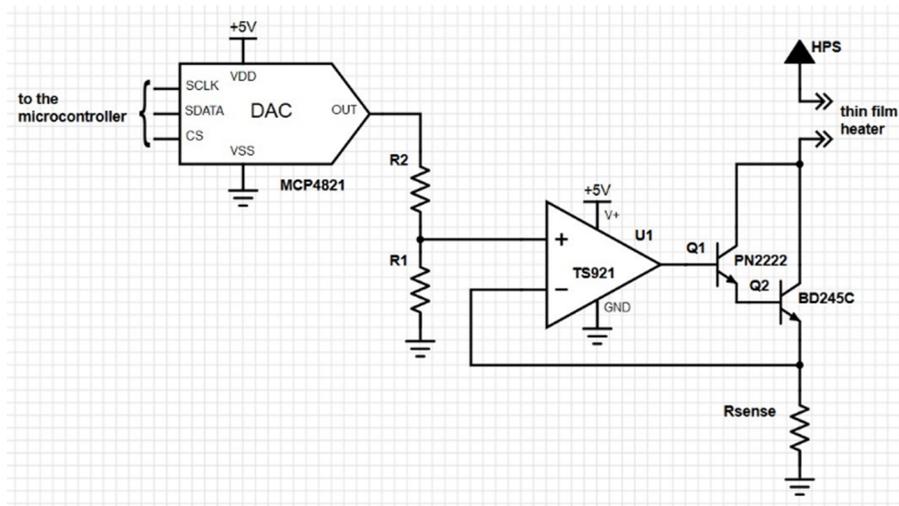
Figure 2.2. Schematic of the current generator that drives the heater.

Most of the current that flows in the heater comes from the collector of the transistor Q2 (BD245C from Bourns®) that is a NPN silicon power transistor with very high maximum continuous collector current (10 A) and a minimum forward current transfer ratio (h_{FE}) of 20. Taking into account this small value of the h_{FE}, the Darlington configuration was used adding to the circuit the transistor Q1 (PN2222 from Fairchild Semiconductor), which is a general-purpose small signal transistor.

The operational amplifier is the TS921 from STMicroelectronic. This is a rail-to-rail single BiCMOS operational amplifier that exhibits very low noise, low distortion

and low offset. The current provided to the heater is set by the MCP4821 converter (from Microchip), which is a single channel 12-bit DAC. The devices operate from a single 2.7 V to 5.5 V supply. A Serial Peripheral Interface allows to control the DAC through a PIC18F4550 microcontroller (also from Microchip). The device has a high precision internal voltage reference ($V_{ref} = 2.048$ V), and the user can configure the full-scale range to be 2.048 V or 4.096 V.

The value chosen for the sense resistance R_{sense} is 0.2 Ω, while the values of R1 and R2 are respectively 1 kΩ and 36 kΩ. With these values, a maximum driving current of about 550 mA has been achieved.

The same typology of circuit has been used to drive the fan that is necessary to quickly cool the LoC device when thermal cycles are required.

2.1.2 Temperature sensor driving circuit

The circuit that infers the heater temperature through the a-Si:H diode is depicted in Fig. 2.3. It drives the diode with a constant current in forward condition and at the same time measures the voltage across the diode (V_{diode} in the figure).
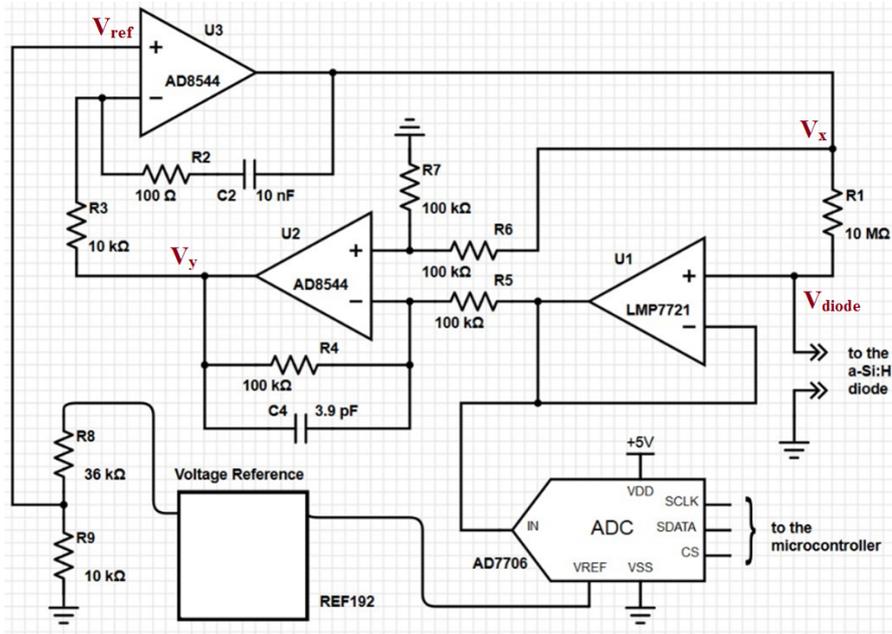
Figure 2.3. Schematic of the circuit which senses the temperature biasing with a constant forward current the a-Si:H diode.

The biasing at constant current is achieved as following. V_{diode} is reported unchanged at the output of the operational amplifier U1 and it is connected, together with the node called V_x, at the operational amplifier U2, mounted in differential configuration. The voltage at the output of U2, called V_y, is:

$$V_y = V_x - V_{diode} \tag{2.1}$$

since the resistance values of R4, R5, R6 and R7 are the same (see Fig. 2.3). The node V_y is then connected to the negative input of the operational amplifier U3

through resistor R3. Due to the virtual short-circuit, both input terminals of U3 are at the same potential thus obtaining V_y equal to V_{ref}. Combining this result with equation (2.1), it is possible to say that the difference between V_x and V_{diode} is constant and equal to V_{ref}. As a consequence, assuming negligible the input current of U1, the current through the a-Si:H is constant and equals the current through R1, whose value is:

$$I_{diode} = \frac{V_x - V_{diode}}{R1} = \frac{V_{ref}}{R1} \qquad (2.2)$$

A voltage reference of 2.5 V (provided by the REF192 from Analog Devices) is partitioned with the resistances R8 and R9 obtaining V_{ref} equal to:

$$V_{ref} = \frac{2.5\,V \cdot 10\,k\Omega}{10\,k\Omega + 36\,k\Omega} \approx 0.543\,V \qquad (2.3)$$

In this way, the current that flows in the diode is:

$$I_{diode} = \frac{V_{ref}}{R1} = 54.3\,nA \qquad (2.4)$$

The component chosen for the operational amplifier U1 is the LMP7721 (from Texas Instruments) since it is a very low input bias current (3 fA), rail-to-rail precision amplifier with a supply voltage range of 1.8 V to 5.5 V. Furthermore, it is characterized by low voltage noise (6.5 nV/$\sqrt{Hz}$) and low offset voltage temperature coefficient (-1.5 µV/°C) required to improve system sensitivity and accuracy. The low output resistance of this integrated circuit allows to drive correctly the AD converter, which digitalizes the voltage across the diode.

The operational amplifiers U2 and U3 are integrated in the same component, which is the AD8544 from Analog Devices. It is a quad rail-to-rail input and output, single-supply amplifier featuring very low supply current (45 µA for each amplifier) and low input bias current (4 pA). This amplifier operates from 2.7 V to 5 V supply.

In order to obtain a very high sensitivity, the AD7706 (from Analog Devices) has been chosen as Analog-to-Digital Converter (ADC). It is a 3-channel complete analog front end for low frequency measurement applications. This device employs a Σ-Δ conversion technique to realize up to 16 bits of no missing codes performance. The selected input signal is applied to a proprietary, programmable-gain (from 1 to 128) front end based on an analog modulator and the modulator output is processed by an on-chip digital filter.

The voltage reference generated by REF192, together with the ADC-gain of 4, were chosen for the converter, obtaining a minimum detectable signal V_{min} equal to:

$$V_{min} = \frac{2.5\,V}{2^{16} \cdot 4} \approx 9.5\,\mu V \qquad (2.5)$$

The ADC and the DAC included in the system are both controlled by the PIC18F4550 microcontroller (from Microchip) through the Serial Peripheral Interface (SPI). This PIC incorporates a fully featured Universal Serial Bus (USB) communications module that is compliant with the USB Specification Revision 2.0. This module allows to control all the functionalities of the electronic board with a common personal computer equipped by the developed GUI.

After designing the electronic system, a Printed Circuit Board (PCB) containing six identical copies of the basic circuit which reads the voltage across the diode has been developed. This configuration allows to control more diodes and therefore to monitor temperature distribution in a complex thermal system. Circuit layout is designed with Altium Designer 2010, and the realized double layer PCB is shown in Fig. 2.4.
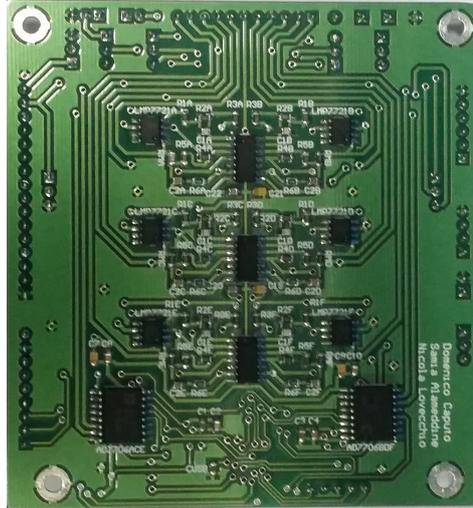
Figure 2.4. Printed Circuit Board controlling six temperature sensors. It was realized according to PC/104 standard and dimensions are 90x96 mm^2.

The circuit has been designed following the design rules of the PC/104 standard layout, obtaining a form factor of 90x96 mm^2. In the lower part of the board are positioned the AD converters used to digitalize the voltages across the diodes, while the microcontroller is located on the other side of the electronic board.

2.2 Thermal control algorithm

As mentioned in the introduction to this Chapter, in order to reach temperature stability during sample treatments a software auto-tuned Proportional-Integral-Derivative (PID) controller has been developed.

2.2.1 PID controller fundamental operation

A PID (or three term) controller allows to fulfill the requirements of a continuous modulated control in a lot of applications (especially in industrial control systems) thanks to its loop feedback mechanism [75]. The control is obtained by continuously calculating an error value $e(t)$ (defined as the difference between a reference value and a process variable) and applying a correction which minimizes the error signal. This correction is based on proportional (P, depending on the value of the error signal), integral (I, determined by the past values of the error signal), and derivative terms (D, which takes into account the variations of the error signal) which give their name to the controller.

Proportional, integrative and derivative modules affect the controller output, which automatically regulates a control variable $u(t)$, such as the current of a heater, to a new value determined by these control terms. Their generation and application principles are reported in the block diagram of Fig. 2.5.
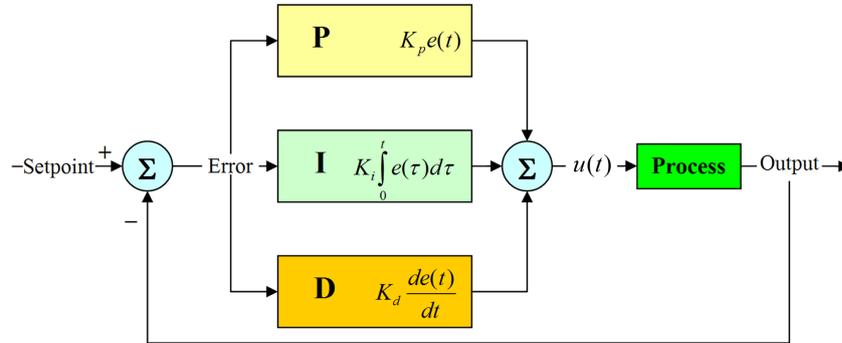
Figure 2.5. Block diagram of a PID controller in a feedback loop.

In this model:

- P is proportional to $e(t)$, calculated as the difference between the reference value (the setpoint) and the process value, thanks to the gain factor K_P. This term cannot be used alone to erase error signal, because if $e(t)$ becomes null there will be no correction, so it will always introduce an offset between the setpoint and the process value.

- I takes into account the past values of the error signal. If the proportional control leaves a residual error, this term attempts to eliminate it by cumulating (integrating) the historical values of $e(t)$. Integral correction factor will stop growing when the error signal is zero.

- D depends on the rate of error changes. It is a sort of anticipatory term, because it seeks to compensate $e(t)$ deviations before it becomes too large (proportional action) or lasts for too long (integrative action). In particular, D effects will be greater as error signal variations increase.

The overall control function can be expressed as:

$$u(t) = K_P \, e(t) + K_I \int_0^t e(\tau) \, d\tau + K_D \, \frac{de(t)}{dt} \tag{2.6}$$

where K_P, K_I, and K_D denote the non-negative coefficients for the proportional, integral, and derivative terms, respectively.

The digital implementation of a PID controller in a microprocessor requires the discretization of the three control terms. The integral one is discretized, with a sampling time Δt, as follows:

$$\int_0^{t_i} e(\tau) \, d\tau \approx \sum_{j=0}^{i} e(t_j) \, \Delta t \tag{2.7}$$

The first-order derivative term is approximated (by backward finite differences) as:

$$\frac{de(t_i)}{dt} \approx \frac{e(t_i) - e(t_{i-1})}{\Delta t} \tag{2.8}$$

Using approximations (2.7) and (2.8) into the equation (2.6), the discrete-time formula of PID can be obtained:

$$u_{i+1} = K_P \, e_i + K_I \sum_{j=0}^{i} e_j \, \Delta t + K_D \left[\frac{e_i - e_{i-1}}{\Delta t} \right] \tag{2.9}$$

where the generic e_k is used instead of $e(t_k)$.

PID performances depend on the specific control problem, and despite their large use they do not provide optimal control for some applications. The fundamental difficulty with PID control is that the feedback control system employs constant parameters with no direct knowledge of the process [76, 77]. For instance, optimal correction terms could be valid only for a specific setpoint and/or boundary conditions. Moreover, PID controllers are linear and symmetric and, consequently, their performances in non-linear systems can be different depending on experimental conditions.

Especially in the thermal control applications, as the developed one, the research of the optimal K gains is very difficult due to the non-linearity and asymmetry (active heating but passive cooling) of the system. Furthermore, various conditions (for example different start-point and/or setpoint temperature) result in different best K parameters. Moreover, the variability of boundary conditions, such as external air flux or environmental temperature, do not enable a preliminary system calibration. Considering all of these aspects, the designed PID controller tries to estimate in real time the K gains which ensure the desired temperature across the heater achieving a very adaptable system [78, 79].

2.2.2 Auto-tuned PID algorithm

The schematic diagram of the developed algorithm is shown in Fig. 2.6.
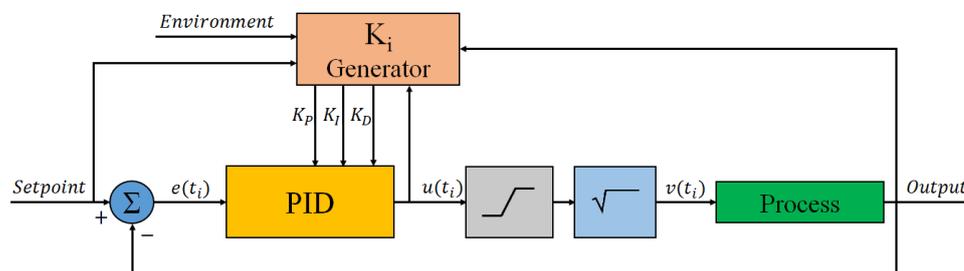
Figure 2.6. Block diagram of the auto-tuned PID controller in a feedback loop.

The block called "PID" evaluates, starting from the calculated error, a value that is proportional to the dissipated power of the heater using, for each cycle, the K gains estimated by the block "K$_i$ Generator".

The gray block ensures that the PID output is not negative (the current of the heater cannot be negative) and not very large, exceeding the maximum current of the heater. In particular, it limits $u(t_i)$ signal to the range 0 - J_{max}^2 (where J_{max} is the maximum current that can be provided to the heater).

Since in an ideal thermal system the temperature reached by Joule effect is proportional to the dissipated power (which is, in turn, proportional to current squared), the square root block (light blue box in the figure) has been introduced to permit the linearization of the whole process.

Finally, the block called "Process" represents the developed lab-on-chip device, which has been described in the Section 2.3. The input variable $v(t_i)$ is the current which flows into the heater, while the variable *Output* is the temperature inferred by the temperature sensor (represented by the voltage across the a-Si:H diode, as explained in the introduction of this Chapter).

A detailed description of the implemented functions in "PID" and "K$_i$ Generator" blocks is reported in the next Subsections.

2.2.2.1   PID evaluation

Respect to the classical discrete-time formula of PID (equation (2.9)), in this work the controller output $u(t_i)$ (see Fig. 2.6) is calculated taking into account the noise coming from the temperature sensor, which affects the PID input and makes unstable the whole feedback loop. In order to avoid this issue, the error is calculated as the average value of the last n values of temperature:

$$e_i = \frac{1}{n} \sum_{j=i-(n-1)}^{i} (T_{SP} - T_j) \qquad (2.10)$$

Consequently, the implemented PID formula is:

$$u_i = K_P \, e_{i-1} + K_I \sum_{j=0}^{i-1} e_j \, \Delta t + K_D \left[\frac{e_{i-1} - e_{i-(n+1)}}{n \, \Delta t} \right] \qquad (2.11)$$

where:

- n is the number of previous steps to consider in order to calculate the average error;

- $u_i = P/R = J^2$ is the square of the current to apply on the heater;

- e_i is the error calculated with the temperature acquired in the previous n steps;

- T_j is the read temperature at step j;

- T_{SP} is the setpoint temperature;

- Δt is the time step.

The K$_i$ parameters, as previously mentioned, are recalculated for each step by the "K$_i$ Generator" block (see Fig. 2.6).

2.2.2.2   PID parameters estimation

The core of the function able to calculate K_P, K_I and K_D is a finite state machine, whose time cycle is Δt, which is shown in Fig. 2.7.
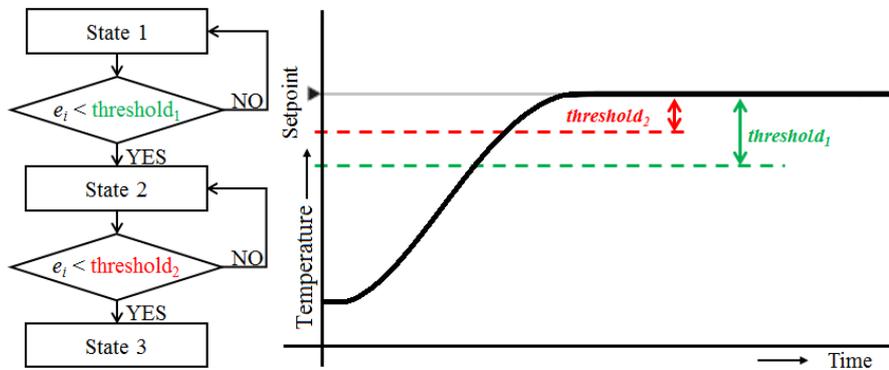
Figure 2.7. Finite state machine controlling the K parameters calculation. In each state, the three K gains are calculated in different way.

When the system starts to control the temperature, the K_i Generator stays into State 1 until the error signal is greater than the value "$threshold_1$". When this condition is not true anymore, K_i Generator switches to State 2, which was introduced, how it will be explained hereafter, in order to avoid sudden output variations. For this reason, the finite state machine stays into this state just for few seconds. Finally, the controller goes through the State 3 (when the error signal is below the "$threshold_2$"), where it stays until the setpoint is changed.

The temperature control works in either cooling or heating. The cooling is obtained through a fan, which is in on state only during State 1 when the starting temperature is higher than the setpoint. It is used to accelerate the cooling (only on/off state are driven), but not during the temperature stabilization process.

The two threshold values are defined by the user and allow to tune the PID response. The optimal thresholds must be chosen taking into account the response time of the system, which depends on the equivalent thermal mass of the LoC device. In particular, the threshold values will be lower when the system response is faster.

All of the K_i Generator parameters depend only on the geometrical and thermal characteristics of the LoC device under test, so they are easy to tune and do not change with variations of the setpoint and environmental conditions.

A detailed explanation of the three states and their functionalities are reported below.

State 1

The finite state machine stays into State 1 until error signal e_i is greater than the $threshold_1$. Since the temperature of the LoC is far away from the setpoint, no great control is needed and the proportional term of the PID device is the only one used. When heating, the output will be the maximum current, while in case of cooling the output is null. Hence, for this state, K_I and K_D are equal to zero and the PID output is equal to:

$$u_i = J^2 = K_P \cdot e_{i-1} \tag{2.12}$$

The K gains are fixed until the finite state machine stays in State 1; moreover, the value of K_P does not change even in the next states.

K_P optimal value has been found considering that:

1. the higher is the setpoint, the bigger will be the K_P;

2. the proportional control will always give a systematic error (an offset) that cannot be arbitrarily reduced due to the thermal inertia of the driven system. Indeed, increasing too much the proportional gain, the system will start to oscillate.

Statement 1 asserts that the control on the temperature must be stronger (taking into account the thermal inertia limits of the LoC) when the setpoint is far away from environmental temperature, but it has to be lighter in the opposite case, in order to avoid a very slow cooling if an overshoot occurs.

Statement 2 results from experimental observations. In particular, once the optimal K_P for a specific setpoint has been found, the new optimal K_P calculated for a different setpoint will give approximately the same offset error. Taking into account equation (2.12), this assertion can be mathematically expressed as:

$$\frac{J_1^2}{K_{P_1}} = \frac{J_2^2}{K_{P_2}} \tag{2.13}$$

where J_1^2 is the stationary current squared which flows into the heater in order to reach the *setpoint*$_1$ value less the error E (a parameter of the K_i Generator that must be set too in order to find the optimal K) and J_2^2 is the stationary current squared flowing into the heater to achieve the *setpoint*$_2$ less the same error value, as shown in Fig. 2.8.
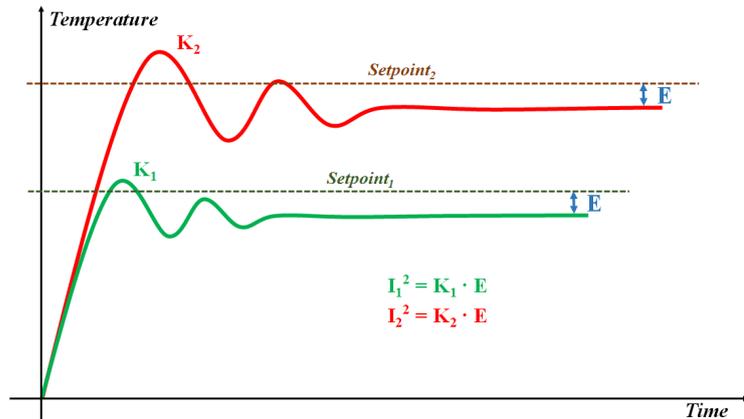
Figure 2.8. Example of pure proportional control responses. The curves refer to the same thermal process, but at different setpoints and K gains. Equations, indicated by the corresponding colors, refer to steady state conditions.

On the other hand, if the system has been calibrated, it is possible to find optimal K_P value from the estimated current needed to reach a specific setpoint, as shown below:

$$K_P = \frac{J_{est}^2}{E} \tag{2.14}$$

As a first approximation, it is possible to consider that the relation between the reached temperature variation and the squared current flowing into the heater is linear. In this way, the following relation has been found:

$$J_{est}^2 = \frac{J_{max}^2}{T_{max} - T_{env}}(T_{SP} - T_{env}) = \frac{J_{max}^2}{\Delta T_{max}} \cdot \Delta T_{SP} \tag{2.15}$$

where J_{max} is the maximum current value that can flow into the heater, T_{max} is the temperature reached by the system when the current J_{max} flows, T_{env} is the environmental temperature and T_{SP} is the setpoint.

The great advantage resulting from this linear approximation is that for the calibration of the system is sufficient just one preliminary measure, that is the value T_{max} corresponding to the current J_{max}. However, with some measures carried out on different systems (that is, considering different geometries of the heater and/or different glass substrate thicknesses), a best estimation has been found with a quadratic relation:

$$J_{est}^2 = \left(C_1 \cdot \frac{\Delta T_{SP}}{\Delta T_{max}} + C_2 \cdot \frac{\Delta T_{SP}^2}{\Delta T_{max}^2} \right) \cdot J_{max}^2 \tag{2.16}$$

where:

$$C_1 + C_2 = 1 \tag{2.17}$$

Combining (2.16) with (2.17), the current estimation function is:

$$J_{est}^2 = \left(C \cdot \frac{\Delta T_{SP}}{\Delta T_{max}} + (1 - C) \cdot \frac{\Delta T_{SP}^2}{\Delta T_{max}^2} \right) \cdot J_{max}^2 \tag{2.18}$$

where C is a form-factor parameter depending on the LoC geometrical characteristics.

It is worth noting, however, that the value obtained with (2.18) results from an approximation, so it will always be affected by an error which changes between different experiments.

In conclusion, when the K_i Generator is in the State 1, the K gains are set to the following values:

$$K_P = \frac{1}{E} \cdot \left(C \cdot \frac{\Delta T_{SP}}{\Delta T_{max}} + (1 - C) \cdot \frac{\Delta T_{SP}^2}{\Delta T_{max}^2} \right) \cdot J_{max}^2 \tag{2.19}$$

$$K_I = 0 \tag{2.20}$$

$$K_D = 0 \tag{2.21}$$

State 2

In the State 2, as in the previous one, the K gains remain fixed for all the time during which the machine stays into this state and, since the temperature is close to the setpoint, it is necessary to introduce the integrative and derivative terms.

When the steady state condition is reached, only the integrative term is different from zero because both the error and its derivative are null, and the control output will be:

$$u_i = J^2 = K_I \sum_{j=0}^{i-1} e_j \, \Delta t \tag{2.22}$$

Considering the estimated current (equation (2.18)), K_I has been set as:

$$K_I = \frac{J_{est}^2}{I_X} = J_{est}^2 \left(\sum_{j=0}^{X} e_j \, \Delta t \right)^{-1} \tag{2.23}$$

where subscript X represents the number of cycles before entering the State 2.

In order to avoid a sudden output change due to the introduction of this new term into the equation (2.11), it has been decided to set the derivative term calculated in X equal to the integral one and opposite in sign. In this way, the value of K_D is calculated as follows:

$$K_D = -\frac{J_{est}^2}{D_X} = -J_{est}^2 \left(\frac{e_X - e_{X-n}}{n \, \Delta t} \right)^{-1} \tag{2.24}$$

Using the equation (2.18), it is possible to obtain the whole equations of the State 2:

$$K_I = J_{max}^2 \cdot \left(C \cdot \frac{\Delta T_{SP}}{\Delta T_{max}} + (1-C) \cdot \frac{\Delta T_{SP}^2}{\Delta T_{max}^2} \right) \cdot \left(\sum_{j=0}^{X} e_j \, \Delta t \right)^{-1} \tag{2.25}$$

$$K_D = -J_{max}^2 \cdot \left(C \cdot \frac{\Delta T_{SP}}{\Delta T_{max}} + (1-C) \cdot \frac{\Delta T_{SP}^2}{\Delta T_{max}^2} \right) \cdot \left(\frac{e_X - e_{X-n}}{n \, \Delta t} \right)^{-1} \tag{2.26}$$

K_P value, as said before, does not change from State 1 during all the process, so it has not been calculated.

State 3

K_i Generator stays into State 3 until the end of process or a change of the setpoint. Unlike the previous states, here K_I and K_D change during every cycle, searching the optimal values which will stabilize system response.

K_D value resulting from State 2 is usually too high, making the control unstable. Moreover, the derivative effect is useful only for the initial oscillation around the

setpoint to reduce overshoots. For these reasons, K_D value is reduced by a percentage factor p_d during each cycle, until its value does not affect the output:

$$
\begin{aligned}
&if \ (K_D \cdot D_i > \bar{u}_i \cdot 0.01) \\
&\quad then \quad K_D = K_D \cdot p_d
\end{aligned}
\tag{2.27}
$$

where

$$
D_i = \frac{e_i - e_{i-n}}{n \, \Delta t}
\tag{2.28}
$$

is the derivative value at instant i, while

$$
\bar{u}_i = \frac{1}{n_2} \sum_{j=i-n_2}^{i} u_j
\tag{2.29}
$$

is the mean value calculated on the last n_2 output values, to which J^2 converges if the controller is working fine.

Also K_I is calculated by estimating the mean value of the current applied to the heater:

$$
K_I = \frac{\bar{u}_i}{I_i}
\tag{2.30}
$$

where

$$
I_i = \sum_{j=0}^{i} e_j \, \Delta t
\tag{2.31}
$$

is the value assumed by the integral at instant i.

Since also $\bar{u}_i$ can oscillate, its value does not change in every cycle, but every n_u cycles, in order to avoid the system instability:

$$
\bar{u}_i =
\begin{cases}
\frac{1}{n_2} \sum_{j=i-n_2}^{i} u_j & if(i \ \mathbf{mod} \ n_u = 0) \\
\bar{u}_{i-1} & otherwise
\end{cases}
\tag{2.32}
$$

In this way, oscillation of K_I values during the process has been avoided.

However, when $\bar{u}_i$ is recalculated, K_I could abruptly change, according to equation (2.30). In order to avoid this issue, it is better to change slowly, as showed in (2.33):

$$
\begin{aligned}
&for \ (a = 1, 2, 3) \\
&\quad if \ (K_I \cdot I_{i-1} > \bar{u}_i + K_I \cdot I_{i-1} \cdot p_a) \\
&\qquad then \quad K_I = \frac{K_I \cdot I_{i-1} \cdot (1 - p_a)}{I_i} \\
&\quad if \ (K_I \cdot I_{i-1} < \bar{u}_i - K_I \cdot I_{i-1} \cdot p_a) \\
&\qquad then \quad K_I = \frac{K_I \cdot I_{i-1} \cdot (1 + p_a)}{I_i}
\end{aligned}
\tag{2.33}
$$

With this algorithm, the integral contribution is increased by a percentage factor p_a if K_I is smaller than the optimal value, otherwise it is decreased by the same percentage. In particular, three different correction values are taken into account depending on the difference between K_I and the optimal value: a hard one (p_1), a medium one (p_2) and a soft one (p_3).

List of parameters

Fig. 2.9 summarizes the whole K_i Generator operation mode, which provides, for each cycle, the K gains for the PID controller (see Fig. 2.6).

only for the input cycle of State 1:

$$K_P = \frac{1}{E} \cdot \left(C \cdot \frac{\Delta T_{SP}}{\Delta T_{\max}} + (1-C) \cdot \frac{\Delta T_{SP}^2}{\Delta T_{\max}^2} \right) \cdot J_{\max}^2$$

$$K_I = 0$$

$$K_D = 0$$

only for the input cycle of State 2:

$$K_P = \frac{1}{E} \cdot \left(C \cdot \frac{\Delta T_{SP}}{\Delta T_{\max}} + (1-C) \cdot \frac{\Delta T_{SP}^2}{\Delta T_{\max}^2} \right) \cdot J_{\max}^2$$

$$K_I = J_{\max}^2 \cdot \left(C \cdot \frac{\Delta T_{SP}}{\Delta T_{\max}} + (1-C) \cdot \frac{\Delta T_{SP}^2}{\Delta T_{\max}^2} \right) \cdot \left(\sum_{j=0}^{X} e_j \, \Delta t \right)^{-1}$$

$$K_D = -J_{\max}^2 \cdot \left(C \cdot \frac{\Delta T_{SP}}{\Delta T_{\max}} + (1-C) \cdot \frac{\Delta T_{SP}^2}{\Delta T_{\max}^2} \right) \cdot \left(\frac{e_X - e_{X-n}}{n \Delta t} \right)^{-1}$$

for every cycle of State 3:

$$K_P = \frac{1}{E} \cdot \left(C \cdot \frac{\Delta T_{SP}}{\Delta T_{\max}} + (1-C) \cdot \frac{\Delta T_{SP}^2}{\Delta T_{\max}^2} \right) \cdot J_{\max}^2$$

$$\bar{u}_i = \begin{cases} \dfrac{1}{n_2} \displaystyle\sum_{j=i-n_2}^{i} u_j & \text{if } (i \bmod n_u = 0) \\ \bar{u}_{i-1} & \text{otherwise} \end{cases}$$

$$for\,(a=1,2,3)$$

$$if\,(K_I \cdot I_{i-1} > \bar{u}_i + K_I \cdot I_{j-1} \cdot p_a)$$
$$then\ K_I = \frac{K_I \cdot I_{i-1} \cdot (1 - p_a)}{I_i}$$

$$if\,(K_I \cdot I_{i-1} < \bar{u}_i - K_I \cdot I_{j-1} \cdot p_a)$$
$$then\ K_I = \frac{K_I \cdot I_{i-1} \cdot (1 + p_a)}{I_i}$$

$$if\,(K_D \cdot D_i > \bar{u}_i \cdot 0.01)$$
$$then\ K_D = K_D \cdot p_d$$

Figure 2.9. Mode of operation of the K_i Generator. On the left, it is shown the finite state machine which is the core of this block. On the right, implemented functions for each state have been reported.

A detailed description of the block input parameter is reported below:

- Δt is the time step. For the presented system, its value is 200 ms.

- n is the number of cycles considered in order to calculate the average error. Best values depend on the Δt of the controller and on the temperature noise. Typical n values are between 2 and 15; its value, however, must be empirically calibrated.

- J_{max} is the maximum current that the electronics can provide to the heater. Heating rate depends on this value.

- ΔT_{max} is the difference between the reached temperature when J_{max} is applied to the heater and room temperature. It must be measured.

- $threshold_1$ is the threshold value that determines the switch to State 2. Its value must be defined empirically and depends on the system response speed. Typical values are in the range 3 °C – 10 °C.

- $threshold_2$ is the threshold value that determines the switch to State 3. Its value must be defined empirically and depends on the system response speed. Typical values are in the range 0.5 °C – 5 °C.

- C is the coefficient of the current squared-differential temperature curve (see equation (2.18)). It depends on the geometrical and thermal characteristics of the system. It must be measured. Its values are between 0 and 1.

- E is the systematic error (offset) deriving from the proportional term. It depends on the geometrical and thermal characteristics of the system. Typical values are between 2 °C and 10 °C, and it must be empirically calibrated.

- n_2 is the number of cycles considered to evaluate the average output current. The best value depends on the oscillation period of the response and must be empirically calibrated. Typical values are between 20 and 200.

- n_u is the number of idle cycles set to calculate the new output average value. The best value depends on the oscillation period of the response. Typical values are between 5 and 30, and it must be empirically calibrated.

- p_d is the percentage factor used to reduce the K_D gain. This value depends on the system speed response. Typical values are between 1% and 10%, and it must be empirically calibrated.

- p_1 is the strong percentage factor used to modulate the K_I gain. Typical values are between 0.5% and 10%, and it must be empirically calibrated.

- p_2 is the medium percentage factor used to modulate the K_I gain. Typical values are between 0.1% and 5%, and it must be empirically calibrated.

- p_3 is the soft percentage factor used to modulate the K_I gain. Typical values are between 0.01% and 1%, and it must be empirically calibrated.

The variation ranges shown above have been obtained from the several experiments carried out during the algorithm optimization.

Despite the high number of parameters to set, system calibration lasts for only few hours and must be done only one time for every device. Moreover, the system response is stable even if there is a relatively high variation of the parameters, and therefore the K_i Generator is very easy to tune. It exhibits very good performances, as shown in the next subsection.

2.2.2.3 Auto-tuned PID performances

In order to demonstrate the efficacy of this algorithm, an example of thermal cycles is reported in both thermal response of the system (Fig. 2.10) and relative current flowing into the heater (Fig. 2.11).
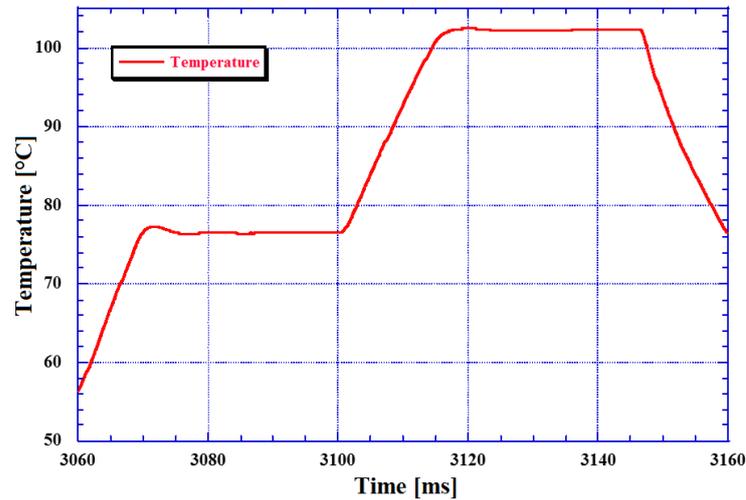
Figure 2.10. Example of developed PID response. Setpoints are 76 °C and 102 °C. The heating rate is the fastest until the setpoint value is reached, while the overshoot is less than 1.5 °C.
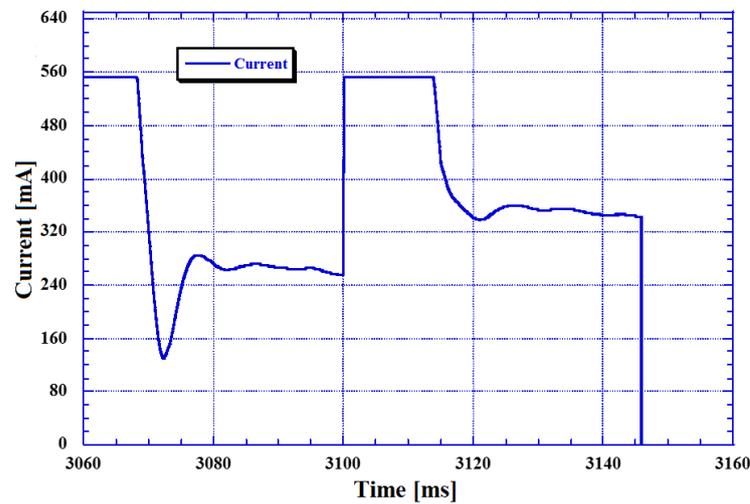
Figure 2.11. Heater current corresponding to the temperature evolution shown in Fig. 2.10. The current value is maximum until the setpoints are reached, while there are no sudden variations during the control.

These results were achieved using the *DARWIN'S* (described hereafter) through the parameters shown in the Table 2.1.

Table 2.1. List of the K_i Generator parameters used in DARWIN'S PID controller

Parameters	Values
Δt	200 ms
n	10
J_{max}	556 mA
ΔT_{max}	$\sim$ 130 °C
$threshold_1$	$\sim$ 4 °C
$threshold_2$	$\sim$ 1.4 °C
C	0.5
E	$\sim$ 4.5 °C
n_2	150
n_u	25
p_d	5%
p_1	0.5%
p_2	0.1%
p_3	0.025%

2.3   Lab-on-chip system: DARWIN'S

The developed LoC integrates on a single glass substrate different thin film technologies in order to develop a multifunctional platform suitable for on-chip thermal treatments and on-chip detection of biomolecules [80]. The whole structure, developed with a PhD colleague, is called *DARWIN'S* (DNA Amplification Reactor With Integrated Network (of) Sensors) or, generically, *System-on-Glass* (SoG): it has been designed taking into account the compatibility between the different manufacturing technologies and the characteristics of the substrate.

In particular, a 5x5 cm^2 glass substrate hosts:

- a thin metal film, placed on a transparent and conductive ground plane, acting as heating source;

- a set of a-Si:H diodes, acting as temperature sensors, to monitor the temperature distribution on the active area of the heater;

- a set of a-Si:H diodes, acting as photosensors, to monitor the luminescence provided by the analytes during the biomolecular recognition.

This Chapter reports only on the thermal treatment module including the thin film heater and the temperature sensors, while the a-Si:H photosensors will be treated in the Chapter 3.

A schematic cross section of the device is shown in Fig. 2.12.

2.3.1   Heater design, fabrication and characterization

The thin film metal resistor, deposited on a glass substrate, features an area comparable to the active area of the thermal treatment and low power consumption. The selected materials and thicknesses, determining the value of the electrical
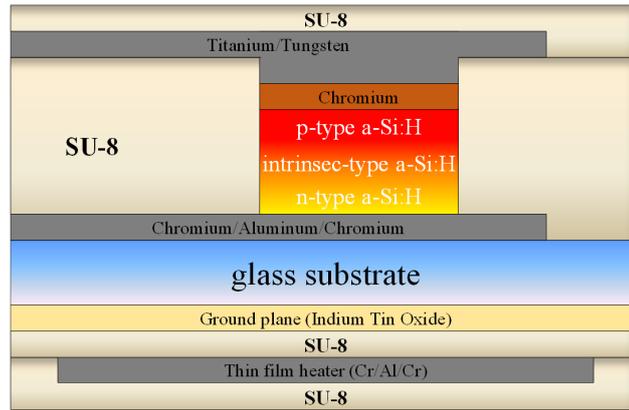
Figure 2.12. Schematic cross section of the lab-on-chip device.

resistance, are mainly defined by the power requirements (see Section 2.1), while the resistor geometry is determined by the specification of uniform spatial temperature distribution over the thermal process area. Starting from the results published in previous works [81], it has been developed a double concentric spiral with a heated area of about 120 mm^2.

The preliminary characterization of a first SoG prototype highlighted a crosstalk between the heater and the a-Si:H sensors. In particular, it has been found that the biasing of the heater affects the current of the thin film sensors, because the leakage current resulting from the voltage applied to the heaters interferes with the current flowing through the sensors (Fig. 2.13a). A ground plane has then been inserted between the thin film heaters and the glass to ensure an electrical path of this current to ground. Therefore, a layer of conductive material has been realized and covered with and insulation plane of SU-8 3005 before the heater fabrication (Fig. 2.13b). The ground plane has been fabricated with a transparent material, Indium Tin Oxide (ITO) to ensure a good alignment between the heater and the sensors.
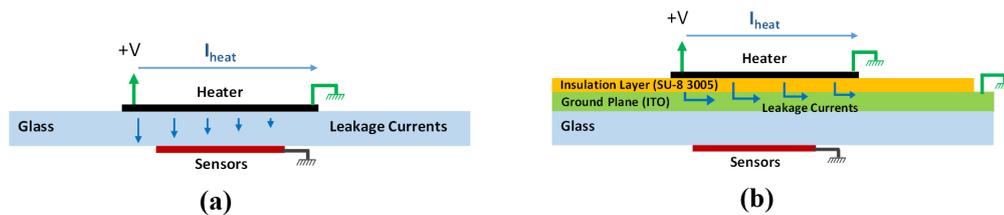
Figure 2.13. SoG scheme without (a) and with (b) the ground plane in ITO (green) and the insulation layer in SU-8 (yellow).

The heater geometry was designed using COMSOL Multiphysics software, coupling the electrical and the thermal problems with the Joule effect and obtaining the temperature profiles due to a potential difference applied across the resistor. Basing on the simulations results, the thin film heater has been fabricated through vacuum evaporation of a 100/600/100 nm-thick Cr/Al/Cr stacked layer and defined by conventional photolithography using the mask depicted in Fig. 2.14.
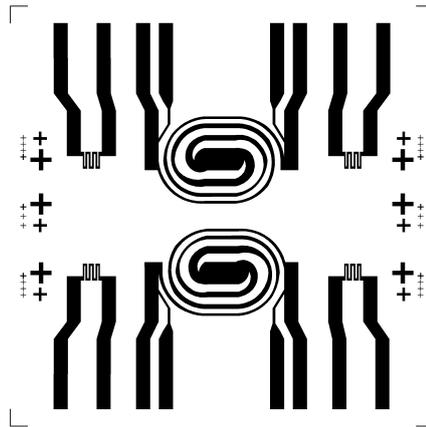
Figure 2.14. Heater mask.

The 5x5 cm^2 glass substrate hosts two mirrored heaters with elliptical shape. Each heater has four electrical contacts: the two external pads provide the current, while the voltage is measured between the internal ones. The obtained resistance was around 11 Ω. A picture of a fabricated chip including only the thin film heaters is shown in Fig. 2.15. In the picture, it is possible to see also, in lateral position with respect to the elliptical heater, another two meander-shaped heaters [82].
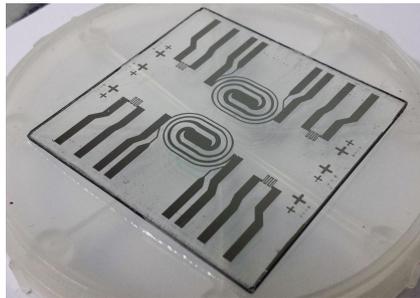
Figure 2.15. Picture of the fabricated heater prototype.

An infrared thermo-camera (FLIR A325) has been used to measure the thermal distribution over the heated area in steady state condition. Results obtained applying a voltage equal to 2.9 V to the heater are reported in Fig. 2.16 in color scale. The elliptical shape, where the temperature is uniform, reproduces the heater geometry. In particular, inside the area ($\approx$120 mm^2) defined by the dashed red line, an average temperature of 338 K with a standard deviation of $\pm$1 K is achieved.

2.3.2 Sensors fabrication and characterization

On the other side of the glass, the a-Si:H devices have been fabricated through Plasma Enhanced Chemical Vapor Deposition (PECVD) and standard microelectronic techniques (evaporation, sputtering, photolithography and etching). In particular, the fabrication steps are the following:

- vacuum evaporation of 30/150/30 nm-thick Cr/Al/Cr stacked layer, which acts as bottom contact of the diodes;
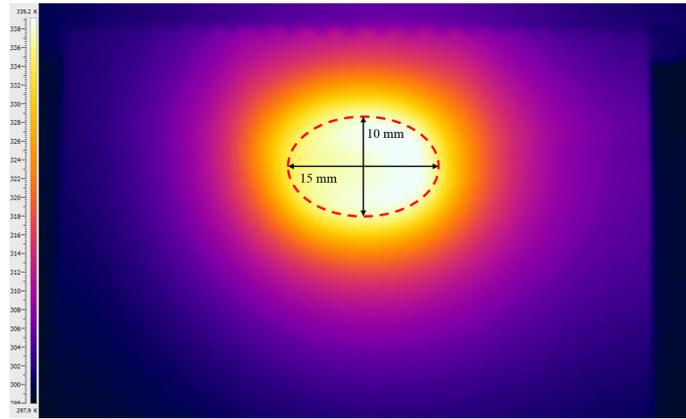
Figure 2.16. Measured temperature distribution over the heater area.

- patterning of the metal stack by conventional photolithography and wet etching process;

- deposition by PECVD of the a-Si:H 30/150/5 nm-thick n-type/intrinsic/p-type stacked structure. The deposition parameters of the PECVD process are reported in Table 2.2;

- deposition by vacuum evaporation of a 50 nm-thick chromium layer, which acts as top contact of the sensors;

- wet etching of the chromium and dry etching of the a-Si:H layers for the mesa patterning. The area of the temperature sensors is 0.8x0.8 mm^2;

- deposition by spin coating of a 5 µm-thick SU-8 3005 (from MicroChem, MA, USA) passivation layer and its pattering for opening via holes over the diodes;

- deposition by sputtering of a 150 nm-thick titanium/tungsten alloy layer and its patterning for the definition of the top contacts and the connection to the pad contacts;

- deposition by spin coating of a 5 µm-thick SU-8 3005 passivation layer.

Table 2.2. PECVD parameters used in the deposition of a-SiC:H n-i-p stacked structure. The gases are SiH$_4$ pure silane, PH$_3$ silane deluted (5%), B$_2$H$_6$ helium deluted (5%), CH$_4$ pure methane; P$_D$ is the process pressure; P$_{RF}$ is the radio-frequency power density; T$_D$ is the substrate temperature.

Layer Type	Material	SiH$_4$ ($sccm$)	PH$_3$ ($sccm$)	B$_2$H$_6$ ($sccm$)	CH$_4$ ($sccm$)	P$_D$ ($Torr$)	P$_{RF}$ (W/m^2)	T$_D$ ($°C$)
n	a-Si:H	40	10			0.3	250	200
i	a-Si:H	40				0.68	250	180
p	a-SiC:H	40		3	60	0.7	250	160

A picture of a fabricated chip including only the thin film sensors is shown in Fig. 2.17.
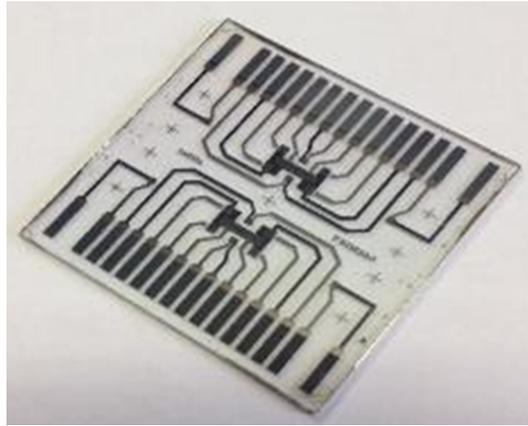
Figure 2.17. Picture of the fabricated prototype including thin film sensors.

The voltage-temperature characteristic of a-Si:H diodes was obtained combining the electronic system described in Section 2.1 and the FLIR A325 infrared thermo-camera. In particular, the average temperature of the diode under test has been monitored through the camera while the electronic board kept constant the temperature of the diode on the heater actuating the PID described in Section 2.2. An example of performed measurement is shown in Fig. 2.18.
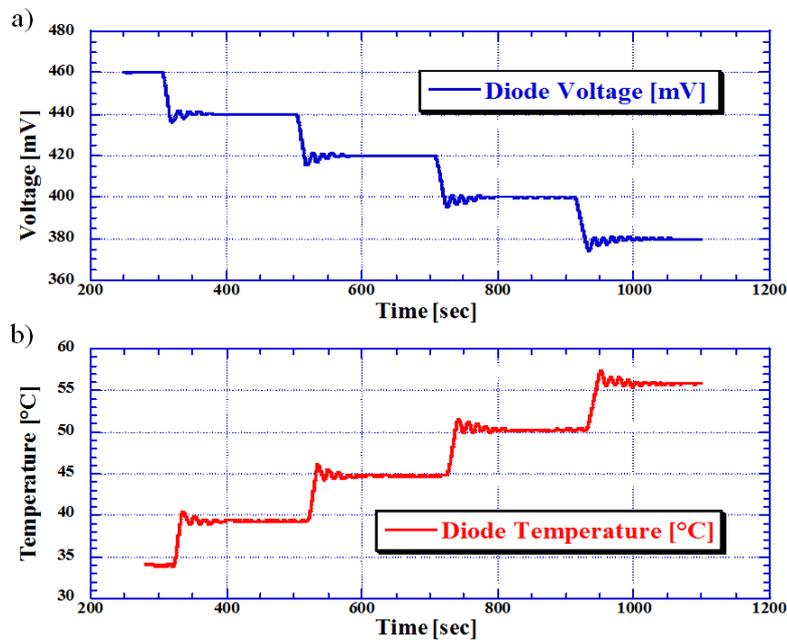
Figure 2.18. Example of measurement performed to determine the dependence of the diode voltage on temperature. The upper graph (a) shows the time evolution of the diode voltage measured by the electronic circuit described in Section 2.1, while the lower graph (b) shows the corresponding time evolution of the diode temperature recorded by the infrared thermo-camera. Steps in the graphs correspond to different temperatures controlled by the PID algorithm.

These measurements results are summarized in Fig. 2.19 for two diodes. Equations inside the figure are the linear fittings of the measured values. The slope of each line represents the diode thermal sensitivity, which is around 3.6 mV/°C for both diodes. Thermal sensitivity of the proposed circuit is directly dependent by this value. In order to calculate the related minimum detectable temperature variations, we must take into account the minimum voltage variation that the ADC can detect. Dividing the ADC resolution (see equation (2.5)) by the diodes sensitivities, the estimated system resolution is around $2.6 \cdot 10^{-3}$ °C.
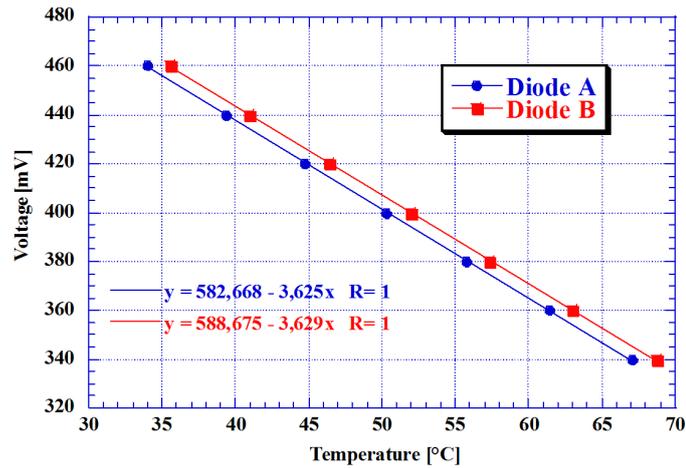
Figure 2.19. Measured voltage-temperature characteristics of different diodes in order to infer the fabrication process variations. Equations, indicated by the corresponding colors, are the linear fittings of measured values.

The accuracy of the system is instead dependent by the accuracy of the thermo-camera used to calibrate the diodes, which is ±2 °C, but this value can be improved using a most accurate instrument during the calibration.

2.3.3 Fabricated LoC

A picture of the fabricated device is shown in Fig. 2.20.
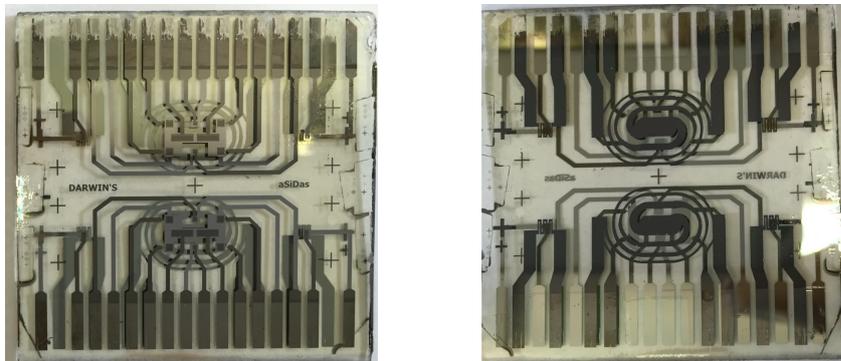
Figure 2.20. Fabricated device: sensor side (left) and heater side (right).

2.4   Experimental results

Using the developed system, two different experiments of DNA amplification has been performed.

2.4.1   On-chip Polymerase Chain Reaction

The LoC device presented in the Section 2.3 was used to perform the Polymerase Chain Reaction (PCR), one of the most useful and versatile processes in biological science. This technique provides amplification of specific nucleic acid sequences and finds applications in genome sequencing, molecular diagnosis of diseases, environmental testing, food technology, agriculture, and forensic science. The PCR mechanism is based on the sample thermal treatment. The standard three-temperature cycling technique has been accomplished. Each PCR cycle consists of the melting of the double-stranded DNA (about 95 °C), annealing of the specific primers to their target gene (usually between 50 and 65 °C), and extension of primers with thermo-stable polymerase enzymes such as Taq polymerase (near 72 °C).

A picture of the experimental setup for the implementation of the PCR is shown in Fig. 2.21.
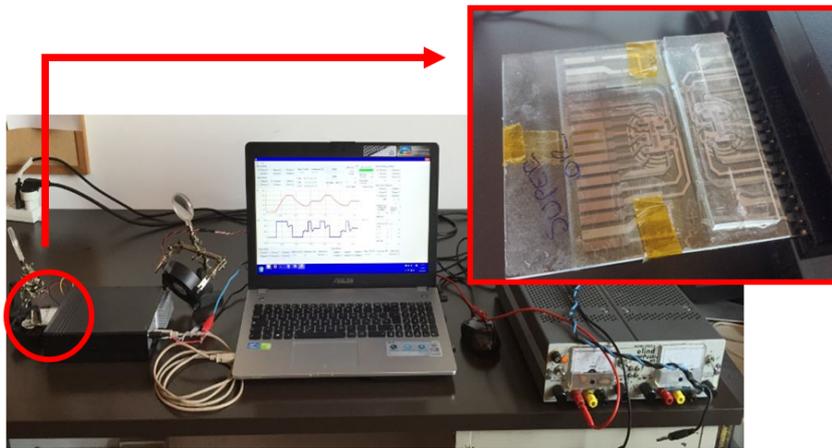
Figure 2.21. Experimental setup used for the implementation of the on-chip PCR. The PC is connected, through the USB, to the black box, which contains the home made electronics. Zoom refers to the LoC device that is thermally coupled to another glass hosting the PDMS microfluidic network.

The PCR experiment was implemented coupling the SoG with an appropriated microfluidic network fabricated on another glass substrate. The microfluidic network provides the sites where the thermal sample treatment occurs, the channels for the sample transportation and a set of micro valves for the fluid control. The chosen material for this network is polydimethylsiloxane (PDMS) due to its optical properties, rapid prototyping and biocompatibility. Indeed, PDMS is optically transparent down to 300 nm wavelength, isotropic and homogeneous and can be easily processed by soft lithography techniques. The glass hosting the microfluidic network has been placed over the SoG aligning by eye the microvalves and the

process chamber with the heaters (see zoom in Fig. 2.21). The thermal coupling between the two glasses has been improved by a mineral oil.

The integrated glass was then connected to the electronic board and the temperature control has been performed through the auto-tuned PID algorithm running on the PC. A picture of the developed GUI, which shows the implemented thermal cycles, is depicted in Fig. 2.22. From these data it is possible to infer that the heating rate is 2 °C/s, the cooling rate 1 °C/s and the ripple ±0.5 °C.
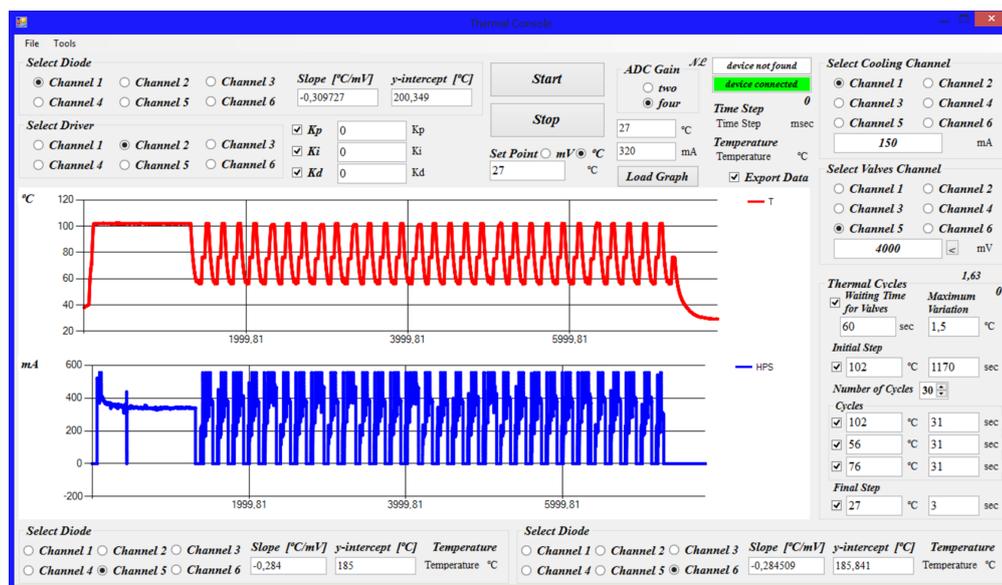
Figure 2.22. Graphical User Interface which controls the electronic board through the auto-tuned PID algorithm. The two inset graphs show the temperature (red curve) and the current driving the heater (blue curve) as a function of time.

PCR experiment has been implemented using a c-DNA obtained from a m-RNA of HPRT mouse myoblast gene. A 15 µl sample containing 4 parts of c-DNA, 1 part of primer/oligonucleotides and 5 parts of DNA polymerase and Sybr green were mixed in a vial. Subsequently 4 µl of this sample were inserted in the microchannels by using a Hamilton syringe. In order to obtain dsDNA denaturation and activation of the polymerase, the temperature was raised at 95 °C and kept constant for 20 min. Afterwards, 30 temperature cycles were applied to the sample using the following scheme: 30 s at 95 °C, 30 s at 55 °C and 30 s at 72 °C.

At the end of the process, the sample was collected from the PCR channel by using the Hamilton syringe and it was transferred in a standard PCR microplate. Analysis of amplified sample was carried out analyzing the solutions using the standard PCR operation system, in order to detect the fluorescent signal deriving from the amplified DNA. This is necessary to verify whether the PCR cycles occurred correctly into the device. The analysis was performed inserting the microplate in the PCR system and reading solely the fluorescence signal deriving from the microplate. To perform the analysis, 4 µl of the sample coming from the PCR chip after amplification and 4 µl of solution before the on-chip PCR experiment were spotted respectively in two different wells of the microplate.

The analysis (Fig. 2.23) showed that amplification occurred and the only
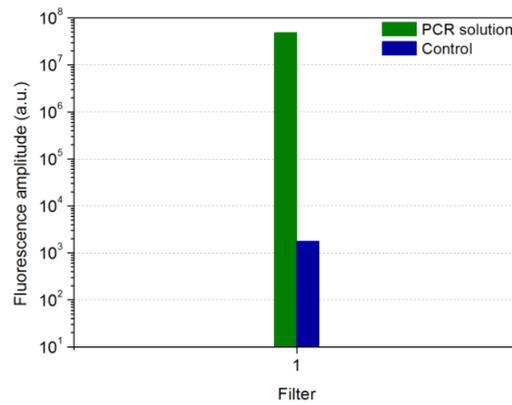
Figure 2.23. Fluorescent signal resulting from the spectrofluorometer after the successful DNA amplification.

fluorescent signal detectable was that in correspondence of the filter 1, matching the typical signal of the Sybr green (a fluorescent molecule) in presence of dsDNA. This fluorophore can emit luminescence exclusively if intercalated in the dsDNA due to the interaction with the base pairs, thus higher is the number of the dsDNA in the sample higher will be the fluorescent signal detected. This relation permits to establish the degree of amplification in a standard PCR process: the green bar in Fig. 2.23 represents the fluorescent signal of this molecule intercalated in the amplified DNA, while the blue one represents the signal of the only Sybr green solution. The PCR process using the SoG device was repeated twice in the microfluidic network leading, for both experiments, to the same amplification results.

A comparison between results obtained using this system and results obtained using a thermocycler, which is a standard instrument for this kind of analysis, is reported in Fig. 2.24.
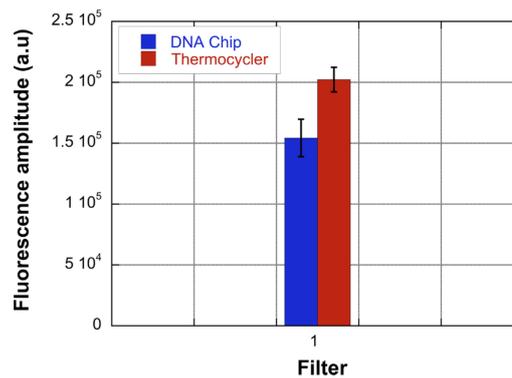
Figure 2.24. Comparison of fluorescence signals obtained with two different measurement techniques. The blue bar refers to the results get with the on-chip system, while the red one represents the signal obtained with a thermocycler.

This figure demonstrates that the developed system is able to successfully implement the PCR with amplification rate very close to those achieved with commercial instruments.

2.4.2   On-chip LAMP-BART reaction

Using *DARWIN'S* LoC including both a-Si:H photosensors and thermal treatments modules, an experiment of real-time PCR was performed. In particular, a loop-mediated isothermal amplification (LAMP) technique was optimized to specifically amplify parvovirus B19 DNA and coupled with Bioluminescent Assay in Real Time (BART) technology to provide real-time quantification of target DNA.

The LAMP-BART reaction was assembled and mixed off-chip before performing the real-time analysis using the SoG equipped with a PDMS microfluidic module, which schematic view is shown in Fig. 2.25.
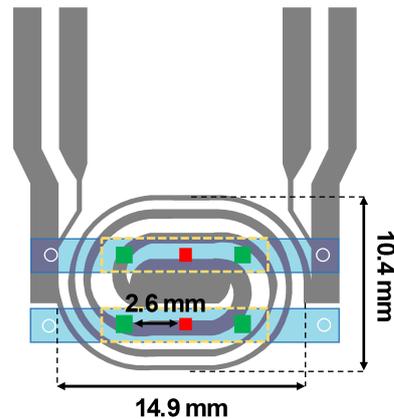
Figure 2.25.   Top view of the main parts of the LAMP-chip. The two microfluidic channels (light-blue rectangles) are aligned with the a-Si:H photosensors (green squares) and temperature sensors (red squares). The gray lines represent the profile of thin film heater, the white circles are the holes for the inlet and the outlet of each channel, and the dashed yellow rectangles represent the useful area of the microfluidic channel.

As a proof of concept, sample containing 10^7 or 10^5 B19V DNA copies were amplified and the photocurrent was recorded in real time. At the beginning of the measurement, the two-channel microfluidic network has been aligned with the a-Si:H sensors: one channel has been filled with the solution containing all the chemicals for the BART reaction including the target DNA and the other channel was used as reference by filling it with the reaction mixture without DNA (blank or control signal). The LAMP-chip designed with two separate reaction chambers represents a versatile system for parallel sample processing; possibly the unknown sample can be tested on duplicate to assess reproducibility or amplified together with a positive control of known DNA concentration allowing for a quantitative evaluation by interpolation on external calibration curve.

The microfluidic inlets and outlets have then been sealed with adhesive foil. Subsequently, through the developed software the diode temperature has been set to 65 °C and the PID algorithm has been launched.

The first result obtained is shown in Fig. 2.26, where the blue curve refers to a sensor aligned with the channel filled with the BART reaction and the red curve refers to a sensor aligned with the control channel.

This experiment thus demonstrates for the first time the ability to display on
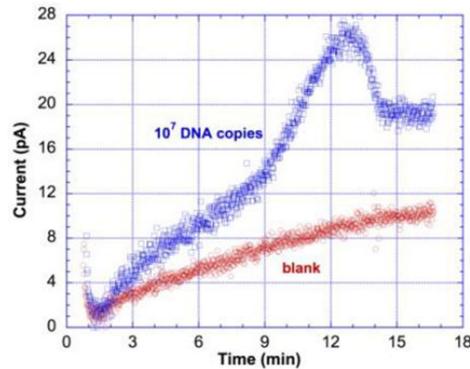
Figure 2.26. Measured photosensor current as a function of time. Only one channel has been filled with 10^7 viral genomes: the red curve is the blank signal (sensor current due to background mixture signal), while the blue curve refers to the total signal (sum of the currents due to temperature and to the BL emission).

a single integrated chip all the functions required to perform a real-time LAMP reaction with on-chip optical detection.

Fig. 2.27a reports the normalized signals of two photosensors monitoring the BART reaction in a sample containing 10^7 copies. We observe that the intensity peak occurs for the two photosensors at the same time, confirming the reproducibility of the whole process.
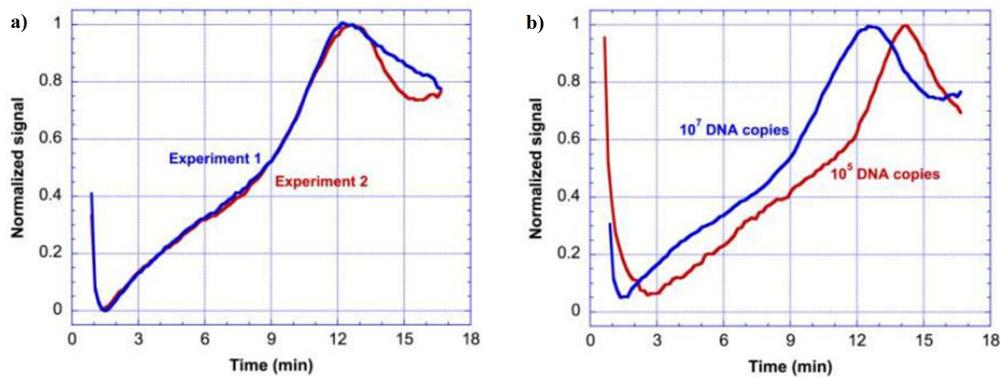
Figure 2.27. Comparison between different quantities of B19V DNA. a) Photocurrent signals of two photosensors monitoring the BART process with 10^7 B19V DNA copies. b) Photocurrent signals of two photosensors monitoring the BART process when one channel contains 10^7 B19V DNA copies and the other one 10^5 B19V DNA copies.

The dependence of the peak occurrence time on the initial amount of target DNA has been observed in the measurements performed. The time at which the peak occurs for the 10^7 target DNA results to be significantly lower than the one corresponding to 10^5 (see Fig. 2.27b), thus preliminary confirming the ability of the system to provide quantitative information. Furthermore, it is worth noting that also the time scale at which the peaks occur are in very good agreement with those found off-chip (Fig. 2.28).

The specificity of the reactions monitored in the two experiments reported above
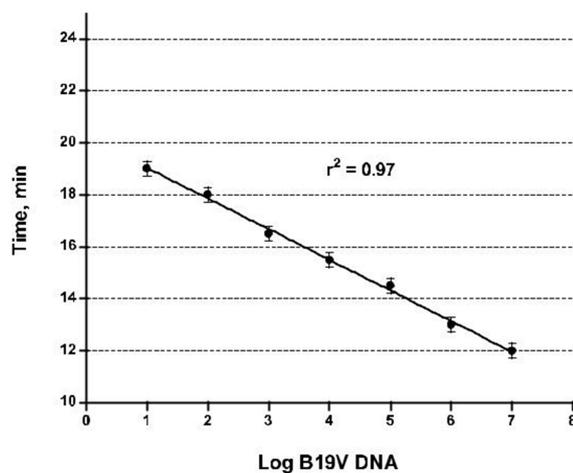
Figure 2.28. Semilogarithmic plot of the time-to-peak versus B19V DNA.

was confirmed with agarose gel electrophoresis and southern blot analysis.

As a final consideration, even though a larger campaign of tests has to be performed to achieve an exhaustive characterization, including a complete calibration curve obtained on the LAMP-chip and analysis of real samples, these results demonstrate the suitability of the presented lab-on-chip to detect viral genomes by LAMP-BART in a really compact and miniaturized system, whose future development can bring to a portable fully integrated device fulfilling the requirements of rapidity, sensitivity, specificity, and ability to provide quantitative information for an accurate early diagnosis of viral infections in a point-of-care environment.

Chapter 3

Optical detection system

This Chapter presents an optoelectronic system-on-glass (SoG) suitable for the detection of fluorescent molecules [71]. It integrates, on the same glass substrate, an array of amorphous silicon (a-Si:H) photosensors and a thin film interferential filter. The system can be directly coupled with another glass substrate hosting a polydimethylsiloxane (PDMS) based microfluidic network where the fluorescent phenomena occur.

The compatibility of the different technological steps to attain on the same glass substrate the photosensors and the filter determined the sequence, the selection of materials and the deposition parameters of the whole process. The electro-optical characterization of the photodiodes, performed after the filter deposition, demonstrated the efficacy of the filter in reducing the excitation light.

The proposed SoG, therefore, features a high miniaturization degree thanks to the on-chip detection performed by the a-Si:H photosensors and to the reduced distance between the fluorescent and the detection sites, which avoids the use of focusing optics.

The system has been successfully tested using the $[Ru(phen)_2(dppz)]^{2+}$ ruthenium complex, a fluorescent dye which works as DNA intercalating molecule [83].

3.1 System design and fabrication

The system, whose cross section is shown in Fig. 3.1, is composed of two optically coupled glass substrates.

The top glass hosts the microfluidic network in which flows the solution containing the fluorescent molecule. It is made by PDMS, which is a silicon-based organic polymer featuring optical transparency to visible light, biocompatibility and ease of fabrication. The choice of this material avoids, therefore, the alteration or the contamination of the sample solution.

The bottom substrate, instead, hosts on the bottom side an array of a-Si:H photosensors, and on the top side the interferential filter.

A detailed description of the design and fabrication steps for both filter and sensors is reported below.
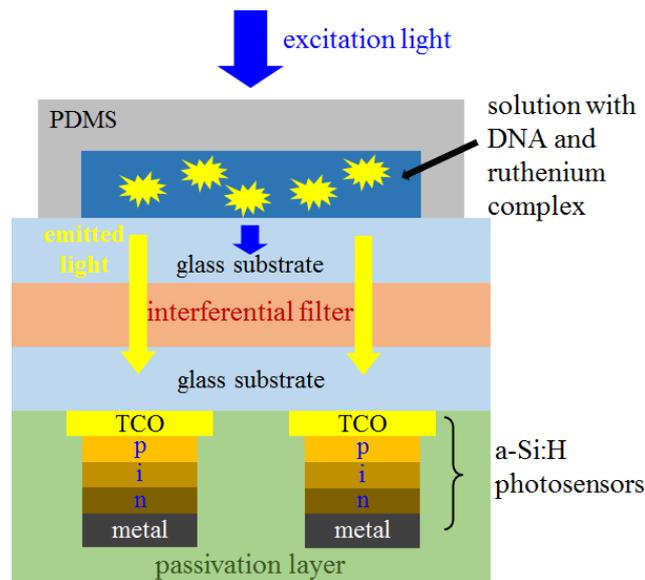
Figure 3.1. Cross section of the proposed system.

3.1.1   Amorphous silicon photodiodes

The a-Si:H photodiodes are arranged in an array of 6x5 sensors. Each sensor has an area equal to 2x2 mm^2.

The fabrication steps of the photodiodes are the following:

- deposition by magnetron sputtering of a 100 nm-thick Indium Tin Oxide (ITO) layer, which acts as transparent bottom contact of the diodes;

- patterning of the ITO layer by photolithography and wet etching processes;

- deposition by Plasma Enhanced Chemical Vapor Deposition (PECVD) of the a-Si:H 5/150/30 nm-thick p-type/intrinsic/n-type stacked structure. The deposition parameters of the PECVD process are reported in Table 3.1;

- deposition by vacuum evaporation of a 50 nm-thick chromium layer, which acts as top contact of the sensors;

- wet etching of the chromium and dry etching of the a-Si:H layers for the mesa patterning of the diodes;

- deposition by spin coating of a 5 µm-thick SU-8 3005 (from MicroChem, MA, USA) passivation layer and its pattering for opening via holes over the diodes;

- deposition by magnetron sputtering of a 150 nm-thick titanium/tungsten alloy layer and its patterning for the definition of the top contacts and of the connection to the pad contacts;

- deposition by spin coating of a 5 µm-thick SU-8 3005 passivation layer.

In order to collect the light coming through the glass, the chosen amorphous silicon structure is the p-i-n one. Indeed, the silicon p-type layer acts as a window

Table 3.1. PECVD parameters used in the deposition of a-SiC:H p-i-n stacked structure. The gases are SiH_4 pure silane, PH_3 silane deluted (5%), B_2H_6 helium deluted (5%), CH_4 pure methane; P_D is the process pressure; P_{RF} is the radio-frequency power density; T_D is the substrate temperature.

Layer Type	Material	SiH_4 $(sccm)$	PH_3 $(sccm)$	B_2H_6 $(sccm)$	CH_4 $(sccm)$	P_D $(Torr)$	P_{RF} (W/m^2)	T_D $(°C)$
p	a-SiC:H	40		3	60	0.7	250	160
i	a-Si:H	40				0.68	250	180
n	a-Si:H	40	10			0.3	250	200

layer, since the light has to be absorbed by the intrinsic region of the diode, which is the active layer of the device. For the same reason, the material chosen for the fabrication of the bottom contacts is the ITO, which is a transparent and conductive oxide. Due to the metallic top contact of the sensors, the light radiation coming from the other side will be rejected.

A picture of the fabricated device is shown in Fig. 3.2.
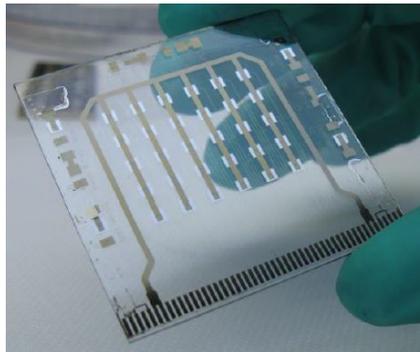
Figure 3.2. Picture of the fabricated prototype including only the photosensors array.

3.1.2   Interferential filter

The interferential filter is a long-pass filter constituted by alternating layers of zinc sulfide and magnesium fluoride. It has been designed with a freeware software (XOP with the IMD extension), and deposited by means of electron beam physical vapor deposition technique without any patterning process. Taking into account the technological steps for the a-Si:H photodiodes fabrication (Section 3.1.1) and the chemical nature of the interferential filter, the photodiodes have been fabricated first and the filter at the end. Careful attention has been paid to the deposition temperature of the filter to avoid any boron diffusion from the p-type layer, which temperature deposition is 160 °C (see Table 3.1), to the intrinsic region. Indeed, to preserve the functionality of the photosensors, previously fabricated on the same substrate, the filter deposition was performed at room temperature.

The system has been designed and tested for detecting the natural fluorescence of ruthenium complex $[Ru(phen)_2(dppz)]^{2+}$, a DNA intercalating dye. Its luminescence

is poor in aqueous solutions but has a sharp increase when the molecule is intercalated into the dsDNA. The absorption peak of the $[Ru(phen)_2(dppz)]^{2+}$ is around 450 nm, while his emission spectrum is centered at 610 nm, as showed in Fig. 3.3.
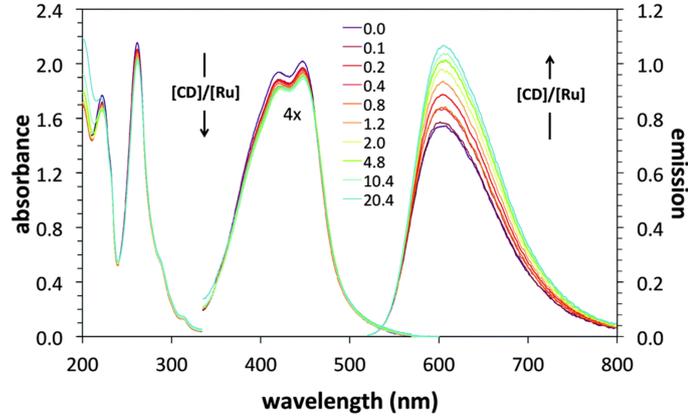
Figure 3.3. Absorbance and emission spectra of the ruthenium complex.

In order to excite the ruthenium complex, the radiation is provided by a blue light emitting diode (LED) (Roithner Lasertechnich APG2C1-450). This light has been filtered with a band pass filter in order to shrink the excitation spectrum. The obtained power density as a function of wavelength is reported in Fig. 3.4.
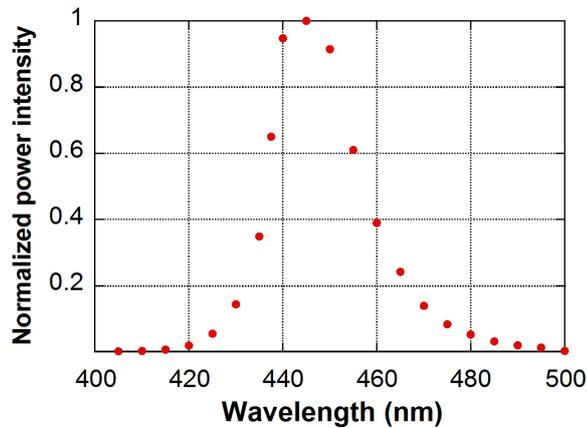
Figure 3.4. Normalized power intensity of excitation LED.

The thin film interferential filter has to transmit only the emission spectrum of the ruthenium complex rejecting at the same time the excitation wavelengths. This reduces the photosensors background signal and avoids the saturation of the read-out electronics. From simulation results, acheved with XOP, it has been found that a stacked structure of zinc sulfide (ZnS) alternating with magnesium fluoride (MgF$_2$) (see Fig. 3.5) satisfies the design requirements, as showed in Fig. 3.6.

3.1.3   Fabricated LoC

A picture of the whole fabricated SoG is shown in Fig. 3.7.

ZnS	27.5 nm
MgF$_2$	65.0 nm
ZnS	55.0 nm
MgF$_2$	65.0 nm
ZnS	27.5 nm
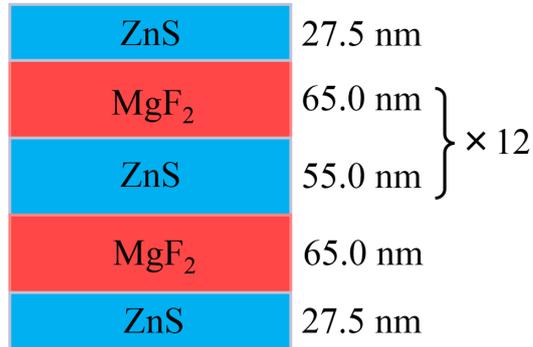
Figure 3.5. Interferential filter cross section.
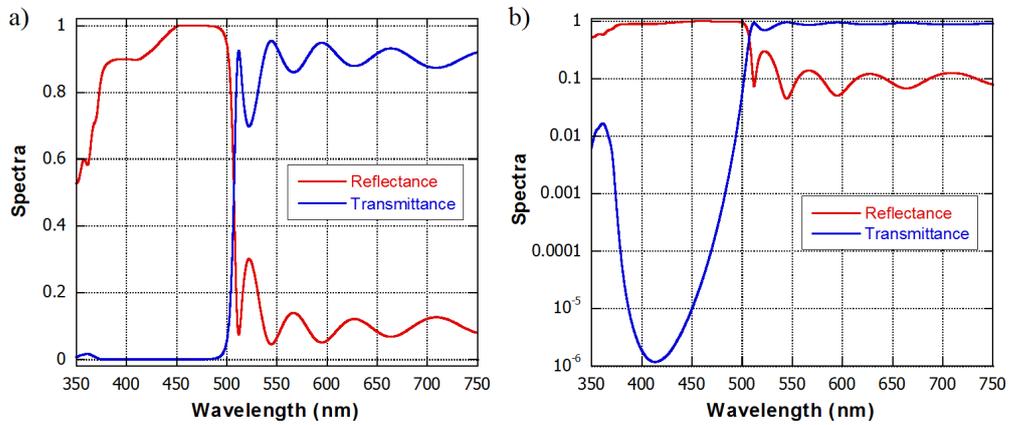
Figure 3.6. Modeled characteristics of the interferential filter. Transmittance (blue curve) and reflectance (red curve) trends showed in linear (a) and semilogarithmic (b) axes.
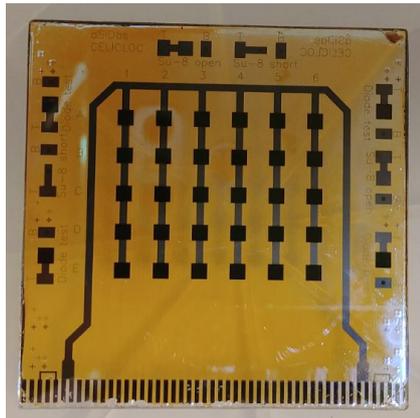
Figure 3.7. Fabricated device integrating a-Si:H photosensors and thin film interferential filter.

3.2   System characterization

Measurements, performed with a spectrophotometer in order to characterize the fabricated filter response, showed an excellent agreement with the modeled data: cut-off wavelength of 550 nm, transmittance higher than 80% for wavelength greater than 550 nm and lower than 0.02% for wavelength smaller than 490 nm (as shown in Fig. 3.8). In particular, the ratio between the transmittance at 610 nm and 450 nm is about 10^5.
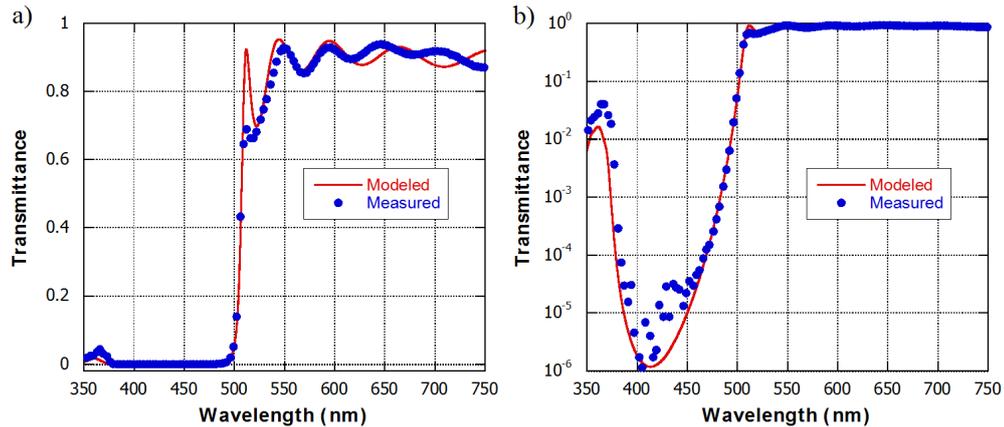
Figure 3.8. Modeled (red curve) vs. measured (blue dot) transmittance in linear (a) and semilogarithmic (b) axes.

Moreover, current-voltage curves of the photosensors have been measured in dark conditions before and after filter deposition (see Fig. 3.9) in order to check the compatibility of the different technological processes.
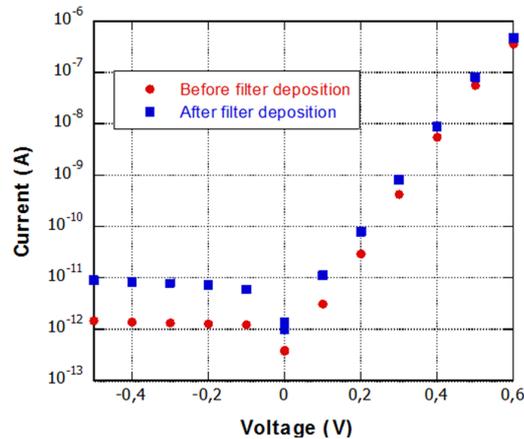
Figure 3.9. Current-voltage curve of a-Si:H photodiode before (red curve) and after (blue curve) the filter deposition.

Results show a very low degradation of sensor inverse current after the filter deposition process, but this increase will not affects the functionality of the device.

To demonstrate the efficacy of the filter in reducing the excitation light, the electro-optical characterization of the photodiodes was performed before and after

the filter deposition. The results show an excellent performance of the system that presents very little attenuation of the ruthenium complex fluorescence wavelength, as it can be seen in Fig. 3.10.
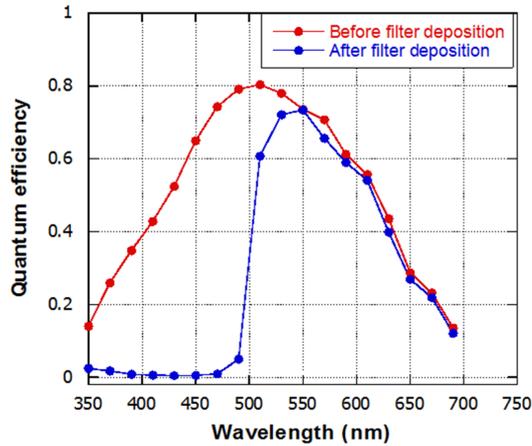
Figure 3.10. Quantum efficiency response of a-Si:H photodiode before (red curve) and after (blue curve) the filter deposition.

3.3 Experimental results

In this Section, results obtained in two different experiments are reported.

3.3.1 DNA detection

A preliminary experiment was performed in order to verify the functionality of the system in detecting dsDNA presence.

The photosensors read-out electronics, the excitation LED and the LoC introduced before (see Section 3.1) are contained in a black metallic box which shields the electromagnetic interferences, as shown in Fig. 3.11.
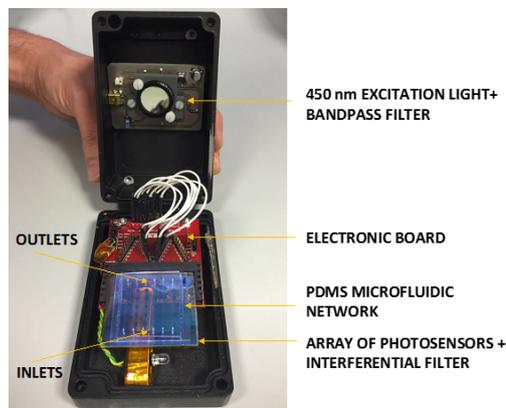
Figure 3.11. Picture of the system. The black metallic box shields the electromagnetic interferences.

The whole system has been tested using a buffer solution, a buffer solution of $[Ru(phen)_2(dppz)]^{2+}$ 0.1 mM, and a buffer solution containing both commercially available dsDNA 1.5 mM and $[Ru(phen)_2(dppz)]^{2+}$ 0.1 mM. The results (Fig. 3.12) show an increase of sensors photocurrent when dsDNA is present in the solution, demonstrating that the reported system is suitable for detecting the variation of the fluorescence intensity as the $[Ru(phen)_2(dppz)]^{2+}$ is intercalated within the dsDNA.
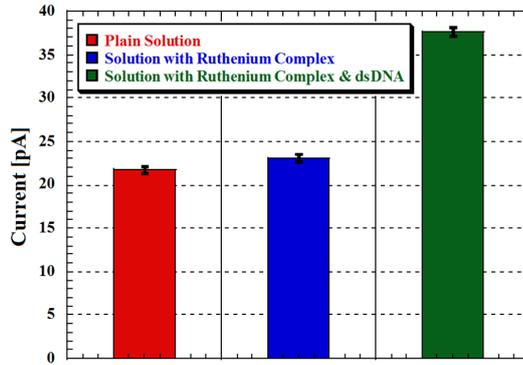
Figure 3.12. Sensors photocurrent at different solution conditions.

3.3.2 Real-Time PCR

Starting from the good results obtained in both on-chip DNA detection (Section 3.3.1) and amplification (Section 2.4.1), a new integrated system suitable for the implementation of the Real-Time Polymerase Chain Reaction (RT-PCR) has been developed. For this purpose, the presented technology for detection of fluorescence has been integrated on the DARWIN'S device to allow, at the same time, on-chip thermal treatments and optical detection of fluorescence.

Taking into account the structure of the DARWIN'S, the interferential filter has been deposited on the photosensors layer of the LoC, which is the only device side sensitive to the light. A picture of the fabricated device is reported in Fig. 3.13, while a schematic cross section of the whole SoG is shown in Fig. 3.14.
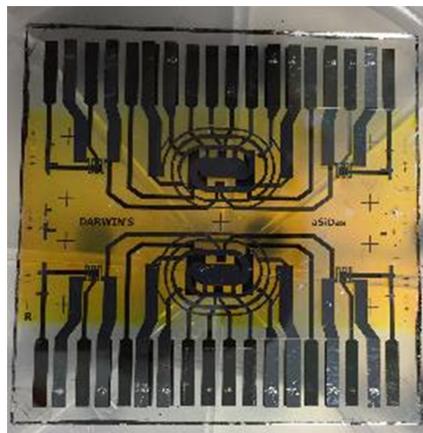
Figure 3.13. Fabricated device: the thin film interferential filter is deposited on DARWIN'S.
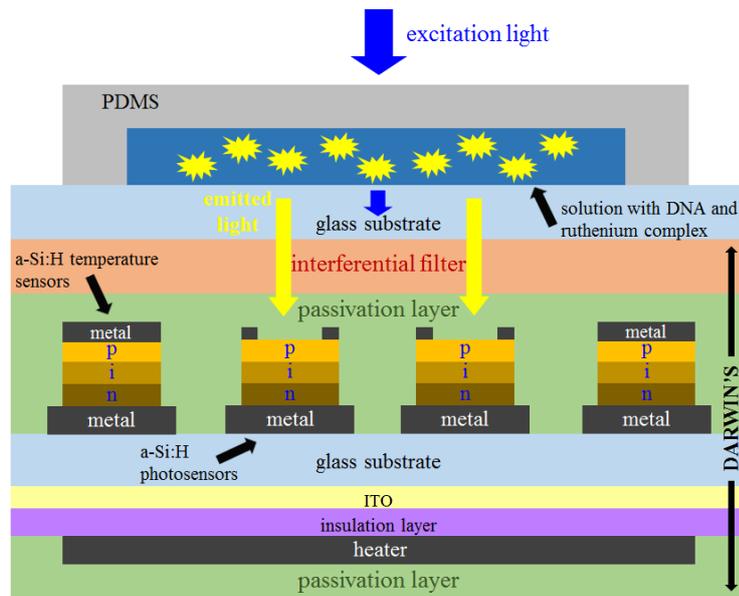
Figure 3.14. Cross section view of the whole system-on-glass.

A picture of the experimental setup is reported in Fig. 3.15. It includes:

- a metal black box, chosen to shield the electromagnetic interferences, which contains all the modules needed for the RT-PCR implementation;

- the electronic board able to perform thermal treatments (described in Section 2.1);

- the photosensors read-out electronics;

- an edge card connector needed to attach the SoG with the custom made electronics;
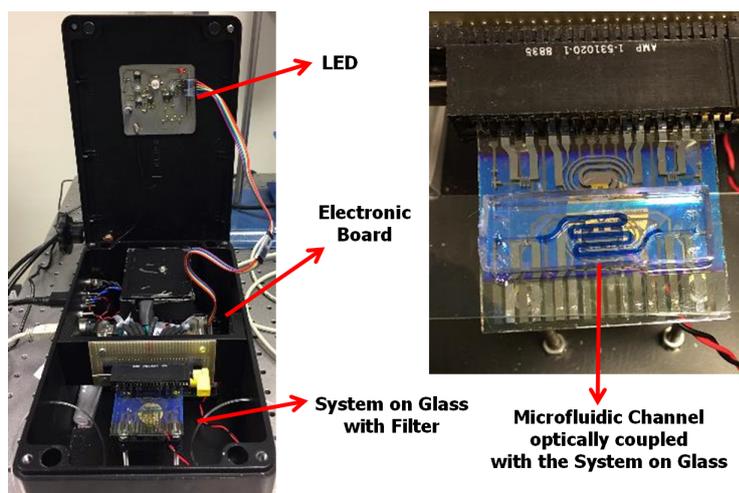
Figure 3.15. Real-Time PCR experimental setup: the metallic black box contains all the modules needed to perform the experiment.

- an electronic board hosting the excitation LED, which is placed on the box cover in correspondence of the LoC;

- the fan used to perform a fast cooling of the device, placed under the SoG.

The right part of the Fig. 3.15 shows the microfluidic network, which is filled with a blue solution in order to make visible the serpentine shaped chamber. The serpentine geometry was chosen in order to easily fill the chamber avoiding the insertion of air bubbles. This microfluidics is the same used in the experiment described in Section 2.4.1, and it is aligned with LoC photosensors as shown in Fig. 3.16.
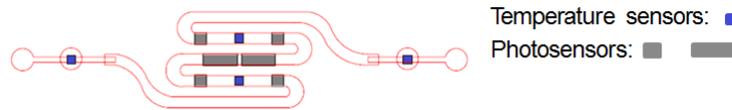
Figure 3.16. Microfluidic network alignment with sensors. The six phothodiodes have different dimensions: the four ones placed on the edges cover an area of 1100x1100 µm^2, while the two placed into the center feature an area of 3150x1100 µm^2. The temperature sensors have an area of 800x800 µm^2.

Two different photodiodes sizes have been considered in order to improve current sensing: the bigger is photodiodes covering area, the higher will be the detected photocurrent. However, the bigger are the photosensors the higher is the dark current, which can saturate read-out electronics in high temperature condition, since the diodes dark current increases exponentially with the temperature. In order to achieve a larger dynamic range of detected light intensities, different photodiodes sizes have been used.

A preliminary calibration of the whole system has been performed at room temperature using a $[Ru(phen)_2(dppz)]^{2+}$ 6x10-5 M and varying the dsDNA concentrations, as shown in Fig. 3.17.
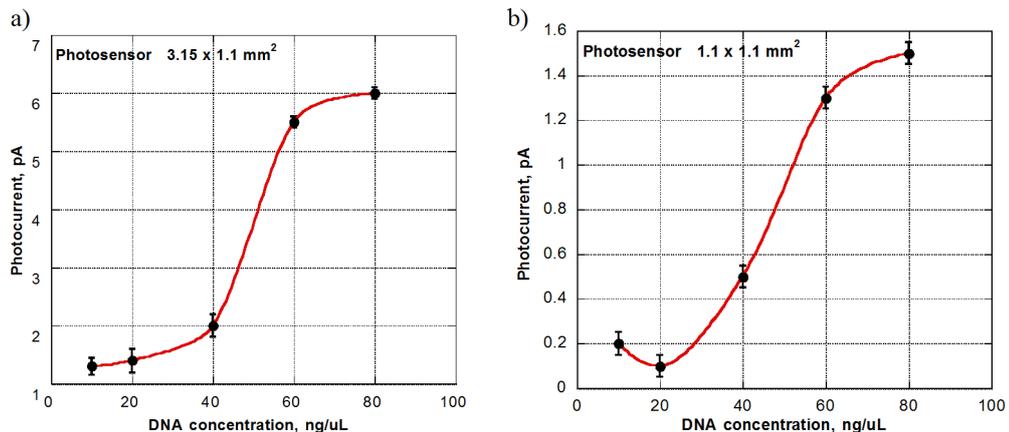
Figure 3.17. Photosensor current as a function of dsDNA concentration. Concentration of ruthenium complex is 6x10^{-5} M. Graphs refer to the different photodiodes size: 3.15x1.1 mm^2 area (a) and 1.1x1.1 mm^2 area (b).

Results in the figures show the increase of sensors photocurrent when DNA is present in the solution, having a concentration range between 10 and 80 ng/µl.

Experimental data demonstrate the success of the developed system in detecting the increase of the fluorescence intensity when the ruthenium complex is intercalated with the dsDNA and suggest its potential application for Real-Time PCR.

Chapter 4

EWOD based multifunctional platform

The aim of this thesis research project is the development of a multifunctional platform which performs all the operations needed to implement biomolecular analysis. In particular, luminescence phenomena detection (such as fluorescence, chemiluminescence, thermochemiluminescence), biomolecular thermal treatments and fluids handling between different reaction sites are the functionalities to implement on it. Fluids handling will take place thanks to the electrowetting phenomena, as shown in Chapter 1. Instead, thermal treatments will be achieved through thin film resistors and a:Si-H temperature sensors, as seen in Chapter 2. Finally, optical detection will be carried out with hydrogenated amorphous silicon (a:Si-H) photosensors. Moreover, it is possible to integrate thin film interferential filters within these modules in order to perform fluorescence quantitative analysis (Chapter 3). Indeed, this kind of analysis requires a light emitting source and an optical filter able to reject the excitation instead of the re-emitted light.

The schematic cross section of the structure to develop is depicted in Fig. 4.1:
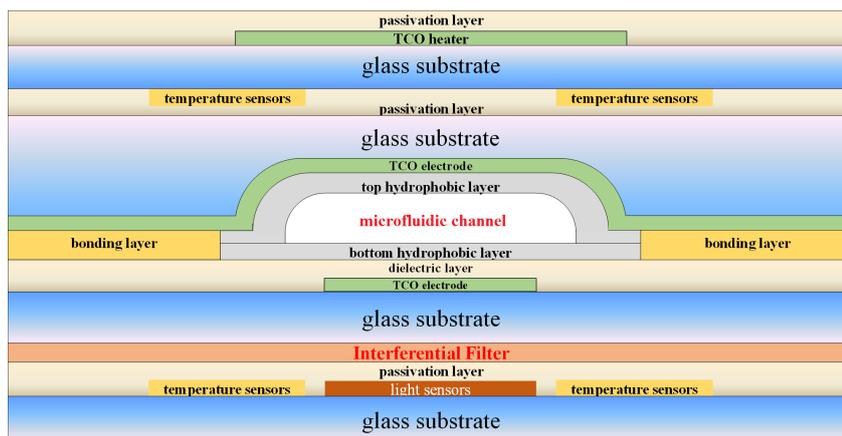
Figure 4.1. Schematic cross section view of the whole device.

As shown in Fig. 4.1, the lab-on-chip device consists of three glass substrates:

- the top one integrates a-Si:H temperature sensors and thin film heaters;

- the middle one consists of two bonded glass substrates forming the EWOD structure described in Chapter 1;

- the bottom one hosts a-Si:H photodiodes to detect the light emitted in the microfluidic channel and additional temperature sensors to better estimate the temperature of the analyte into the microfluidic network.

In the next sections, the top glass will be referred as "heater chip", while the bottom substrate "sensor chip".

It would be possible to integrate the heaters and the sensors even into the external layers of the EWOD structure. However, this kind of chip must be changed after every chemical or biomolecular analysis due to the microfluidic channel contamination. A modular system, such as the one proposed here, allows to replace only the microfluidic module, while the detection (sensor chip) and the thermal treatment (heater chip) modules can be reused.

In this Chapter, the final chip device will be presented, taking into account the results shown in the previous sections.

4.1 System design and chip contact method

When considering the proposed platform design, it is very important to pay particular attention to the chip contact method, which determines the device dimensions. Indeed, in order to ensure the possibility to contact all the layers, a useful design provides substrates with different dimensions, as shown schematically in Fig. 4.2. In this way, there will always be an uncovered edge which can be used to contact the corresponding layer.
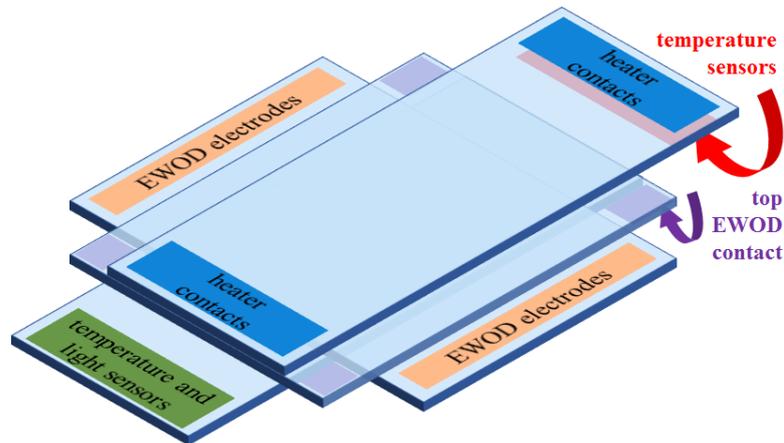
Figure 4.2. Schematic 3D view of the proposed multifunctional platform.

Thanks to this design, it is possible to contact the external substrates, which host the sensors and the heater, on the shorter edge, while the EWOD electrodes can be placed on the middle substrate along the perpendicular long edge. The hardest layer to contact is the one including the top common electrode of EWOD, since only the corners are still free. However, considering that this layer is completely covered

by ITO (see Chapter 1), just one contact point is enough to ensure a full control of the fluid handling.

In order to correctly choose the device size, the connector pitch and the number of pads needed to contact all the modules of the platform have to be taken into account. For the presented platform, the module that needs the larger number of contacts is the EWOD microfluidic, whose size depends on the number of the electrodes. Indeed, the higher is the number of site reactions, the higher will be the number of pads needed to handle the fluid.

Owing to the selected connector (5-5530843-4 Edge Card Connector from TE Connectivity Amp) and the designed microfluidic network (which will be shown in Section 4.2), the dimensions of the final device will be equal to 3.5x9 cm^2 for top and bottom glasses, while the EWOD structure, placed in the middle, will feature an area of 5x7 cm^2. A top and side view picture of the device, displaying the relative distance between the substrates, is shown in Fig. 4.3.
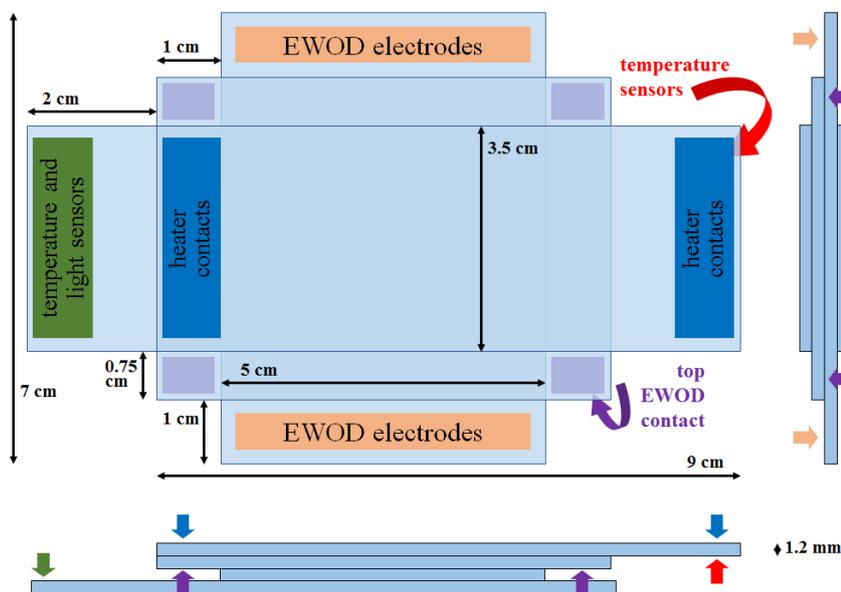
Figure 4.3. Schematic top and side view of the proposed platform showing substrates dimensions and positions.

The selected connector presents a 2.56 mm pitch and 1.6 mm large pads, therefore it is possible to place 4 pads per centimeter on the edges of the glass substrates. Considering all the dimensions mentioned before, there will be 20 pads per edge for the EWOD chip, for a total of 40 positions for the microfluidic network. Furthermore, sensors and heaters substrates are characterized by 14 pads per edge.

A schematic view of the printed circuit board (PCB) which will contact the designed LoC is shown in Fig. 4.4.

Since the substrates have different heights, some wedges (brown blocks in the figure) are placed under the connectors in order to correctly contact all the modules. Moreover, the showed black connectors have been derived from the previous ones cutting them transversely, as depicted in Fig. 4.5.
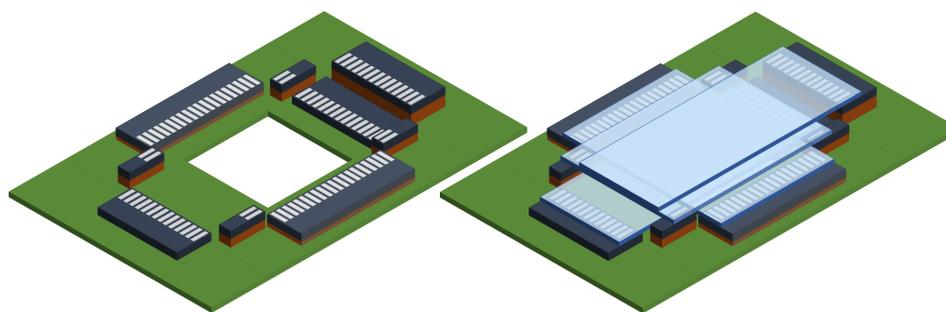
Figure 4.4. Schematic 3D view of the designed PCB bottom layer. Another PCB, complementary to the showed one, must be placed on the top of the LoC in order to contact the other layers.
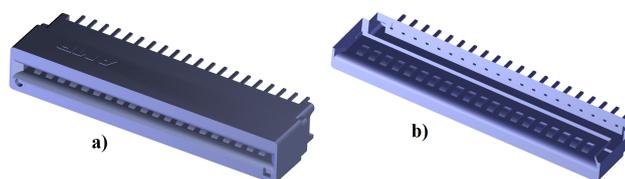
Figure 4.5. Edge card connector (5-5530843-4) 3D models: integral (a) and cut (b) versions.

4.2   EWOD chip

As said in the previous Chapters, the temperature uniformity requirements and the light and temperature sensors positions depend on the dimensions of the reaction chambers. For this reason, the electrowetting-based microfluidic network has been the first device of the multifunctional platform to be designed.

Though the strength of an electrowetting-based network resides in the easy handling of the biological samples within different LoC sites, the proposed device hosts only one reaction chamber for an easier development.

During the microfluidic network design, two distinct versions have been fabricated with a different number of reservoirs, while the position and the dimension of the reaction chamber remain unchanged in order to use both designs with the same heater and sensors chips.

4.2.1   Two reservoirs design

The first designed microfluidic chip hosts two reservoirs, a reaction chamber and two channels which allow the fluid handling between them. This structure is similar to the fabricated prototype showed in Chapter 1. It differs only for the higher number of electrodes in the channels due to the bigger dimension of the substrate. Moreover, in order to allow the light to reach the photosensors, the Cr/Al/Cr layer of the prototype presented in Chapter 1 has been replaced by ITO.

A 3D chip view is shown in Fig. 4.6a.

The octagonal chamber, whose dimensions are reported in Fig. 4.6b, covers an area of about 56 mm^2, while each round reservoir (Fig. 4.6c) covers an area of 64 mm^2. The distance between the electrodes is equal to 50 µm in the entire chip,
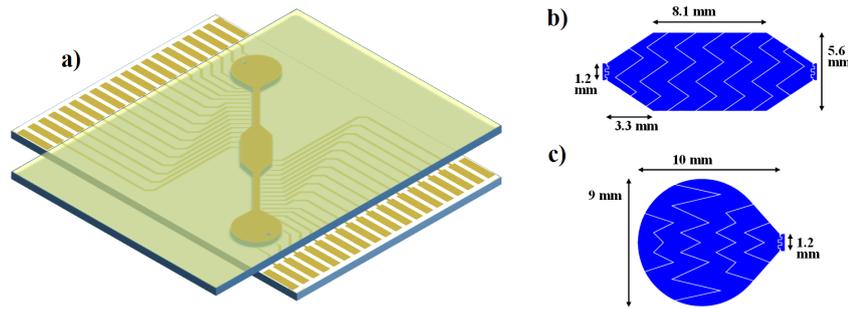
Figure 4.6. Two reservoirs EWOD design: a) 3D model; b) size details of chamber; c) size details of reservoirs.

while the width of the channel connecting the chamber to the reservoirs is 1.2 mm. Since the height of the microfluidic chamber is 100 µm, the reservoirs volume is 6.4 µl, while the chamber one is 5.6 µl. A detail of the interdigitated electrodes can be seen in Fig. 1.5.

For the fabrication of such network, three different photolithographic masks (shown in Fig. 4.7) have been used. Their drawing has been carried out with the graphic software AutoCad.

Bottom layer (mask #1)   Top layer (mask #2)   Teflon structures (mask #3)
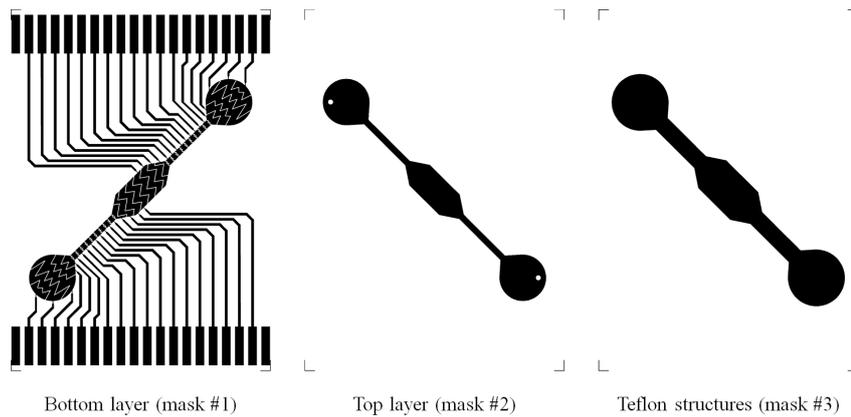
Figure 4.7. Two reservoirs EWOD masks.

From the top layer mask, it is clear the correct position of the via holes: it has to be ensured that the heater chip will not cover the vias when all the LoC modules are being connected.

Furthermore, as can be seen in the bottom mask, the pads placed on the edges of the bottom glass are not used for the connections. The reason for this choice lies in the hard damages that the edges of the substrates suffer during fabrication processes.

4.2.2 Four reservoirs design

In order to design a more complex microfluidic network, useful for applications requiring reagents mixing, a EWOD chip hosting four reservoirs has been developed.

Unlike the chip presented in the previous section, this version requires a number of electrodes higher than the available pads. For this reason, some pads have been interconnected, paying careful attention to avoid an unwanted displacement of the fluid. In order to avoid this issue, the connections have been designed as shown in Fig. 4.8.
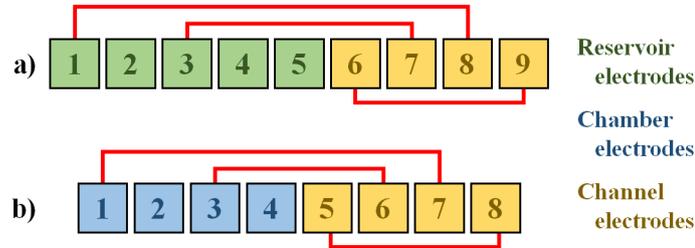
Figure 4.8. Schematic pad connections for reservoirs (a) and chamber (b). The color of the electrodes corresponds to the text color reported on the right part of the figure.

In particular, for the reservoirs the connection scheme is that presented in Fig. 4.8a, which allows the control of 9 electrodes (5 for the reservoir and 4 for the output channel) using only 6 pads. The similar scheme shown in Fig. 4.8b allows to control 8 electrodes (4 for the chamber and 4 for the output channel) using only 5 pads. If a voltage is applied to move the fluid between two adjacent pads, in the whole array there will not be other two adjacent electrodes activated. Moreover, intersections between connections have been avoided in order to fabricate this layout on one single layer.

The masks used for the fabrication of this microfluidic network are shown in Fig. 4.9.

Bottom layer (mask #1)   Top layer (mask #2)   Teflon structures (mask #3)
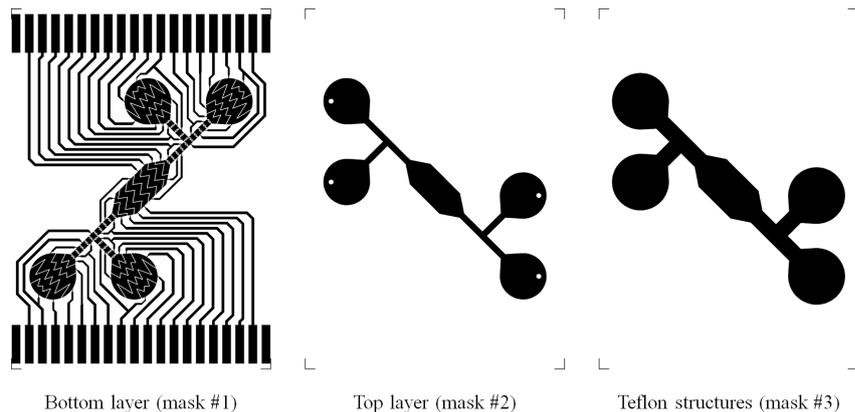
Figure 4.9. Four reservoirs EWOD masks.

Shape and dimensions of chamber and reservoirs are the same reported in the previous section.

4.3 Top chip

The top chip of the presented multifunctional platform hosts, on one side, the thin film heater suitable for thermal treatments, and on the other one, an array of temperature sensors, as shown in Fig. 4.1. In the next section a detailed description of the heater is presented, including COMSOL Multiphysics thermo-electrical simulations, while in Section 4.3.2, the temperature sensors design is shown.

4.3.1 Heater design

4.3.1.1 Operating principle

When an electric current flows into a conductor, there is a dissipation of energy as heat owing to the Joule effect depending on the intensity of the electric current. This effect is the principle of working of the thin film heater. It is possible to mathematically express the first Joule's law as follows:

$$P = V \cdot I \tag{4.1}$$

where P is the dissipated power, V is the voltage applied to the circuit and I is the intensity of the current. In case of a resistor, using the Ohm's law, this relationship can be rewritten as:

$$P = \frac{V^2}{R} = I^2 \cdot R \tag{4.2}$$

The resistance value depends on the choice of the metals, of the film thicknesses and of the geometry according to the relation:

$$R = \rho \cdot \frac{L}{h \cdot s} \tag{4.3}$$

where ρ is the electrical resistivity of the used material, L is the resistive path length, h is the section thickness and s is the width.

The energy dissipated in the form of heat increases with the increase of the current flowing through the resistor, whose dependence on the temperature is usually linearized with the expression:

$$R = R_0 \cdot [1 + \alpha(T - T_0)] \tag{4.4}$$

where R_0 is the value of the resistance at a given temperature T_0 and α is the coefficient of thermal resistance depending on the type of material. Using (4.3), the equation (4.4) can also be expressed in term of resistivity as given below:

$$\rho = \rho_0 \cdot [1 + \alpha(T - T_0)] \tag{4.5}$$

where ρ_0 is the metal resistivity at the temperature T_0.

The thermal behavior can also be expressed in terms of dissipated power as shown below:

$$\Delta P = H \cdot \frac{d\Delta T}{dt} + G\Delta T \tag{4.6}$$

where ΔP is the change in power dissipated within the system, H is the heat capacity and G is the thermal conductance to the surrounding medium.

4.3.1.2 COMSOL Multiphysics

Even if the power dissipated in a heater due to the Joule effect is a well known phenomenon, it is difficult to analytically solve the temperature distribution in the entire device. For this reason, COMSOL Multiphysics software has been used to design the thin film heater.

COMSOL Multiphysics is a finite element numerical simulator able to couple different physical phenomena. To simulate the device composed of a thin film heater deposited on a glass substrate, the electrostatic problem and the heat transfer problem have been coupled. The first one was used to calculate the electric field (E) and the current density (J) in the structure when an electric potential (V) is applied to a conductive thin film. The second one was used to calculate the temperature field in the device when a specific heat flux (Q_{DC}) is applied to the structure. The coupling between the two problems is ensured by the following relation:

$$Q_{DC} = J \cdot E \qquad (4.7)$$

where Q_{DC} is the heat flux and it is the input variable of the thermal problem, J is the current density and E is the electric field. J and E are the output variables of the electrostatic problem which has as input only the voltage applied to the heater. In addition, the temperature dependence of the resistivity has been included in the simulation. This can be expressed by equation (4.5), where T_0 is the room temperature, ρ_0 is the resistivity at room temperature, α is the thermal coefficient of the material and T is the operating temperature expressed in Celsius degrees. This equation further concatenates the modules used in the simulations because the electrostatic model depends on the heat transfer model.

The thermal module determines the heat transfer in the structure taking into account conduction, convection and radiation contributions. In particular, the contribution by convection has been evaluated considering an external natural convection whose heat transfer coefficient (h) depends on the surface A, on the atmospheric pressure P_a and on the external temperature T_{ext} ($h = h_{air}(A, P_a, T_{ext})$).

4.3.1.3 Heater geometry and materials

The selected materials and thicknesses, determining the value of the electrical resistance, are mainly defined by the power requirements (see Section 2.1.1), while the resistor geometry is determined by the specification of the uniformity of the spatial temperature distribution over the thermal process area.

The heater geometry, chosen after several simulations, includes four parallel arms made in ITO connected together by a Cr/Al/Cr stacked layer, whose dimensions are reported in Fig. 4.10.

ITO was chosen since it is a transparent material, allowing the excitation light to reach the chamber above, while the stacked layer of Cr/Al/Cr allows to avoid thermal dissipation on the connection arms due to its low resistance.
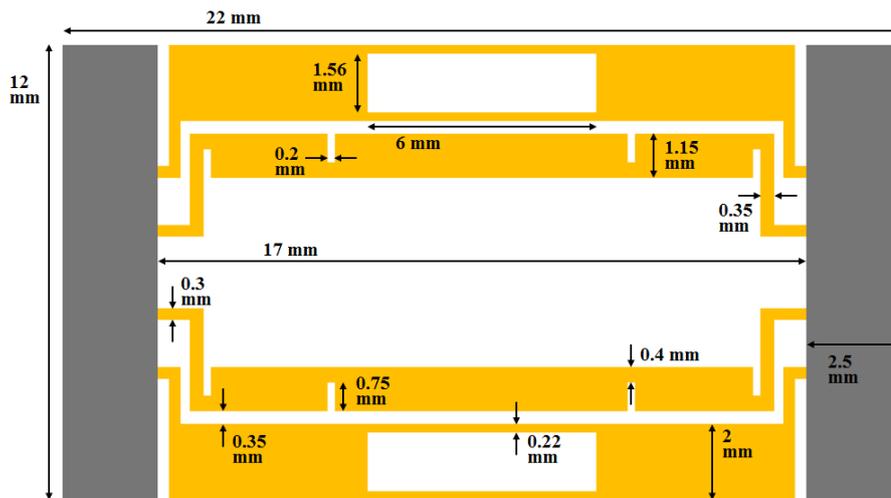
Figure 4.10. Heater geometry. The yellow regions are made in ITO while the gray parts are Cr/Al/Cr stacked layers.

The heater geometry has been placed in correspondence of the active area, which is determined by the microfluidic chamber shape. The simulated structure is shown in Fig. 4.11a, together with the position of the chamber (b) and temperature sensors (c).
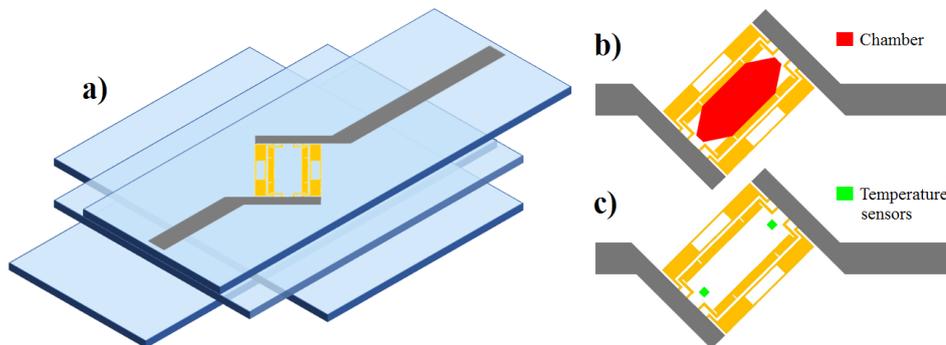
Figure 4.11. Details of heater position: a) 3D model of whole platform; b) Chamber position; c) Temperature sensors positions.

The temperature sensors positions are chosen in order to avoid a shadowing effect on the chamber. Indeed, fluorescence detection is achieved by illuminating the chip from above; for this reason, the sensors are placed on the edges of the active area. As previously described, the chamber is positioned two glasses under the heater, while the temperature sensors are placed on the same glass substrate, but on the other side. The other temperature sensors, which are positioned on the bottom glass of the whole structure, are aligned with the showed ones.

In Table 4.1 are reported the simulation parameters, which include all material parameters, obtained through their characterization, and design parameter, such as the thicknesses of the layers chosen in order to achieve the desired resistance value (see Section 2.1.1).

Table 4.1. Simulation parameters of the heater chip.

Chromium conductivity	$\sigma_{chromium}$	$7.96{\cdot}10^6$	[S/m]
Chromium thermal resistance coefficient	$\alpha_{chromium}$	$2.886 \cdot 10^{-3}$	[1/K]
Chromium layer thickness	$h_{chromium}$	$300{\cdot}10^{-10}$	[m]
Aluminum conductivity	$\sigma_{aluminum}$	$4.106{\cdot}10^7$	[S/m]
Aluminum thermal resistance coefficient	$\alpha_{aluminum}$	$3.224 \cdot 10^{-3}$	[1/K]
Aluminum layer thickness	$h_{aluminum}$	$600{\cdot}10^{-10}$	[m]
Aluminum emission coefficient	$\varepsilon_{aluminum}$	0.15	
ITO conductivity	σ_{ITO}	$0.309{\cdot}10^{-6}$	[S/m]
ITO thermal resistance coefficient	α_{ITO}	0	[1/K]
ITO layer thickness	h_{ITO}	$7500{\cdot}10^{-10}$	[m]
ITO emission coefficient	ε_{ITO}	0.3	
Glass thermal conductivity	k_{glass}	1.12	[W/(m·K)]
Glass density	ρ_{glass}	2200	[kg/m3]
Glass heat capacity at constant pressure	Cp_{glass}	830	[J/(kg·K)]
Glass emission coefficient	ε_{glass}	0.95	

4.3.1.4 Simulation results

The result of a first steady state simulation shows that the temperature uniformity of the active area, evaluated as the difference between maximum and minimum values, is about 1.2 °C when the average temperature is 95 °C, as it can be seen in Fig. 4.12.
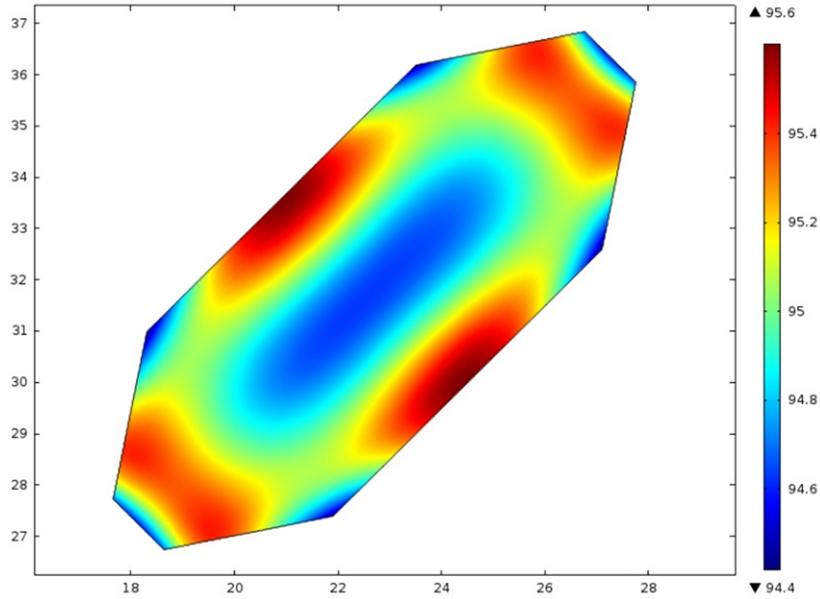
Figure 4.12. Chamber temperature distribution in steady state condition.

In Table 4.2 are summarized the simulation results obtained with different applied voltages, showing temperature uniformity, average temperature, current flowing into the heater and dissipated power. Obtained resistance value is 37.6 Ω.

The value of 19 V represents the maximum voltage available for the electronics. The other voltage values have been chosen as a reference for the three-temperature

Table 4.2. Steady state simulation results as a function of different applied voltages.

V_{in} [V]	I [mA]	P [W]	T_{avg} [°C]	ΔT_{unif}
19	505.2	9.6	192.7	5.5
11.31	300.7	3.4	95.1	1.2
9.13	242.7	2.2	72.2	0.5
7.24	192.5	1.4	55.2	0.4

Polymerase Chain Reaction (see Section 2.4.1).

Time dependent simulations have also been performed in order to evaluate the transient response of the system. In particular, the average temperature trend of the sensors has been assessed. Fig. 4.13a reports the average temperature evolution of the chamber compared with the temperature sensors (placed above and below the EWOD layer) evolution.
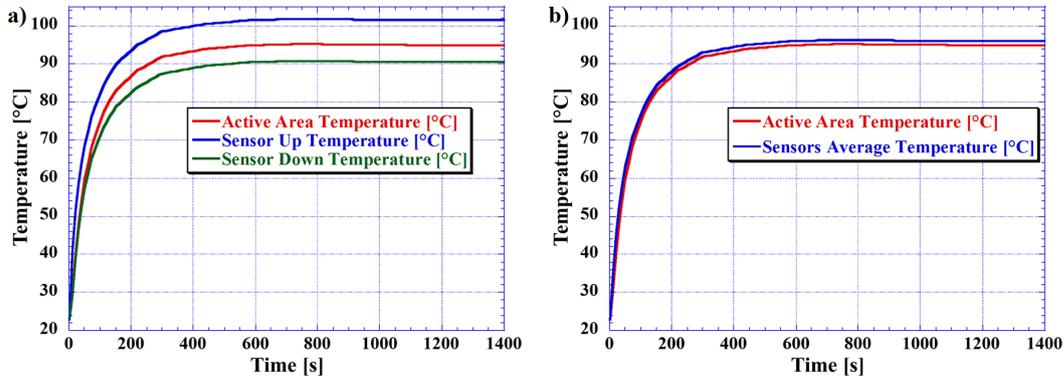
Figure 4.13. Comparison between sensors and chamber average temperatures: a) up and down sensors temperature reported separately; b) average temperature between the two sensors.

As it can be seen in the first graph, the system is not completely symmetric, suggesting that the chamber estimated temperature calculated as the average value of the temperature read by the two sensors (placed respectively one glass layer above and one below the chamber) is affected by an error. This one is represented by the difference between the two curves of graph (b). The temperature error as a function of time is reported in Fig. 4.14 for both sensors and for their average value.

Data reported in Figg. 4.13 and 4.14 refers to the average chamber temperature of 95 °C, which was considered as the worst case of operation of the system. When the chamber temperature is lower, the obtained estimation errors decrease significantly.

4.3.2   Sensors design

The temperature sensors are metal/p-type/intrinsic/n-type/metal stacked structures deposited on a glass substrate by means of the following fabrication steps:

- deposition by magnetron sputtering of a Ti-W alloy layer, which acts as bottom contact of the diodes;
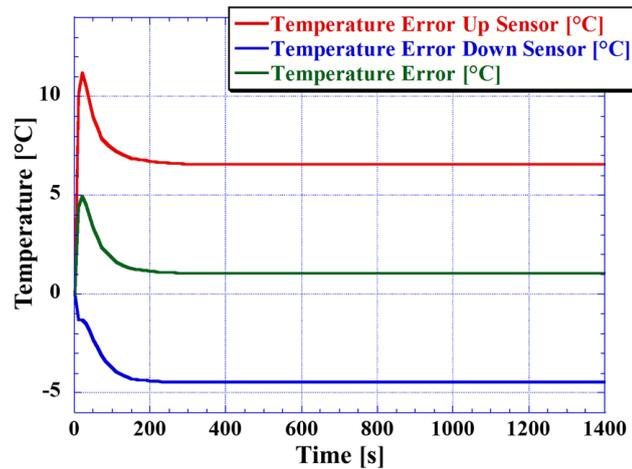
Figure 4.14. Temperature error as a function of time. Red and blue curves refer to the error of single sensor respect to the chamber. Green curve shows the error when considering the average temperature of the two sensors.

- patterning of the metal layer by conventional photolithography and wet etching process;

- PECVD of the a-Si:H p-type/intrinsic/n-type stacked structure;

- deposition by vacuum evaporation of a chromium layer, which acts as top contact of the sensors;

- wet etching of the chromium and dry etching of the a-Si:H layers for the mesa patterning of the diodes;

- deposition by spin coating of a 5 µm-thick SU-8 3005 (from MicroChem, MA, USA) passivation layer and its pattering for opening via holes over the diodes;

- vacuum evaporation of a Cr/Al/Cr stacked layer and its patterning for the definition of the top contacts and of the connection to the pad contacts;

- deposition by spin coating of a 5 µm-thick SU-8 3005 passivation layer.

Unlike the sensors structure shown in Section 2.3.2, the a-Si:H structure presented here is a p-i-n instead of a n-i-p one. For the DARWIN'S device, the only available structure was the n-i-p one, because it was necessary to have the photosensitive layer on the external side of the glass. For the temperature sensors, this constraint is no more required; moreover, a p-i-n structure is easier to fabricate thanks to the higher n-layer thickness, which less suffers the damage due to the fabrication steps subsequent to the deposition one.

As shown in Fig. 4.15, there are six temperature sensors: two (the blue squares) are placed within the active area and four (the magenta squares) outside. These external four sensors allow to carry out fabrication processes measurements.

The diodes position was designed according to the microfluidic chamber placement, while their electrical contacts have been patterned following the specifications
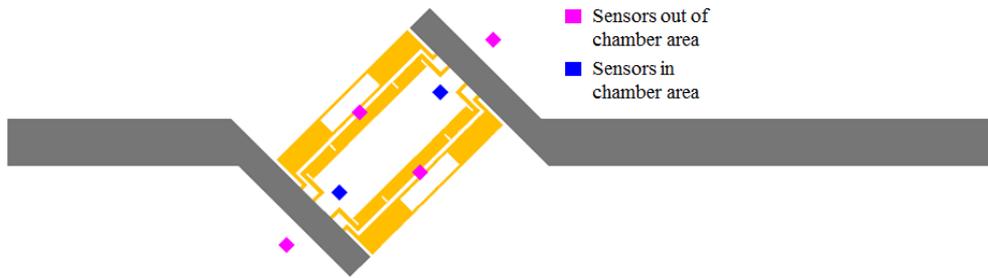
Figure 4.15. "Heater chip" temperature sensors position.

of the card edge connector used for biasing and read out of the sensors. The exact dimensions of the diodes are 1000x1000 µm^2.

The fabrication of the chip requires the four photolithographic masks reported in Fig. 4.16.

Bottom layer (mask #1) Sensors structures (mask #2) Passivation layer (mask #3) Top layer (mask #4)
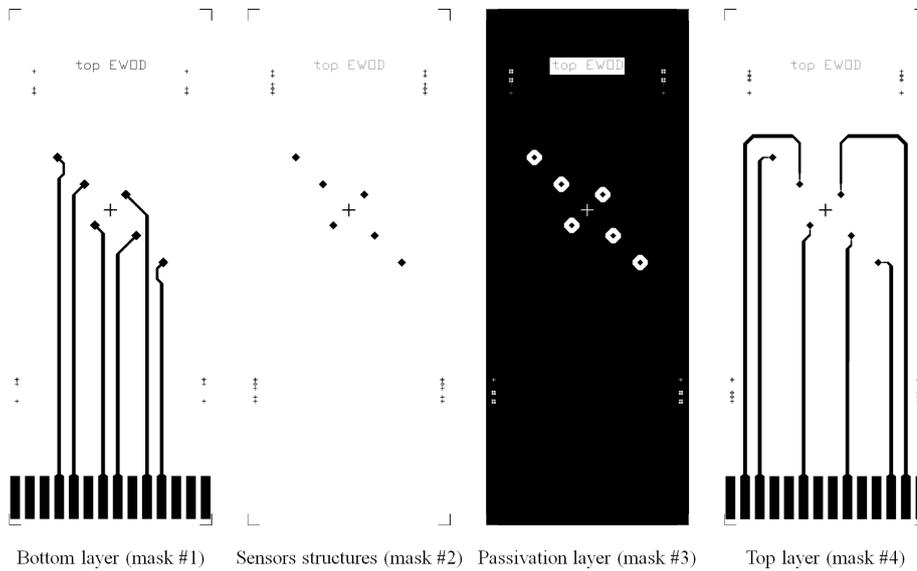
Figure 4.16. "Heater chip" masks designed with AUTOCAD software.

To create an alignment for the subsequent layers, a marker set was also designed at the edges of the structure. These markers have the standard form of a symmetrical cross, as it is possible to see in Fig 4.17 together with their dimensions.
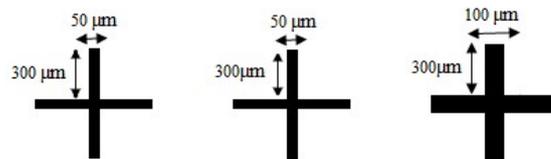
Figure 4.17. Alignment markers.

The aligned masks on the AutoCAD interface are shown in Fig. 4.18. In blue is reported the bottom contact of the sensors, in white the mesa, in orange the SU-8

via holes and in red the top metal contact.
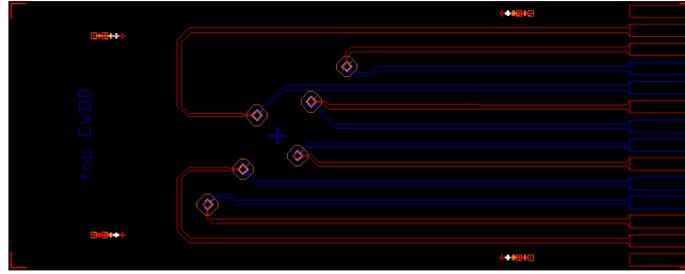
Figure 4.18. "Heater chip" AUTOCAD interface showing all the layers used for the sensors fabrication.

4.4   Bottom chip

For this chip, the sensors are metal/n-type/intrinsic/p-type/metal stacked structures. The fabrication steps are the following:

- deposition by vacuum evaporation of a Cr/Al/Cr stacked layer, which acts as bottom contact;

- patterning of the metal layer by conventional photolithography and wet etching process;

- PECVD of the a-Si:H n-type/intrinsic/p-type stacked structure;

- deposition by magnetron sputtering of a ITO layer, which acts as top contact of the sensors, and its patterning through the lift-off process;

- dry etching of the a-Si:H layers for the mesa patterning of the diodes;

- deposition by spin coating of a 5 µm-thick SU-8 3005 (from MicroChem, MA, USA) passivation layer and its pattering for opening via holes over the diodes;

- deposition by magnetron sputtering of a Ti-W alloy layer and its patterning for the definition of the top contacts and of the connection to the pad contacts;

- deposition by spin coating of a 5 µm-thick SU-8 3005 passivation layer.

As shown in Fig. 4.19, there are six photosensors (green squares) and two temperature sensors (light blue squares).

The temperature sensors position is the same of those placed in the heater chip, while the photosensors are placed in correspondence of the central part of the heater. The exact dimensions of the photodiodes are 1200x1200 µm^2 and 1200x3250 µm^2.

The masks reported in Fig. 4.20 are respectively for the metal bottom contact, the mesa of the sensors, the insulation layer and the metal top contact.

The aligned masks on the AutoCAD interface are shown in Fig. 4.21. In blue is reported the bottom contact of the sensors, in white the mesa, in orange the SU-8 via holes and in red the top metal contact.
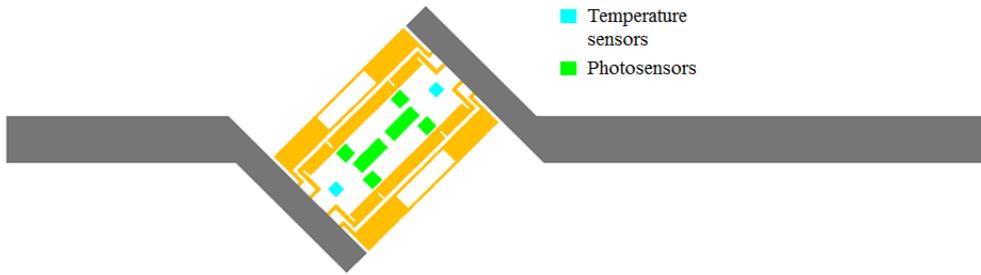
Figure 4.19. "Sensors chip" temperature sensors position.

Bottom layer (mask #1)   Sensors structures (mask #2)   Passivation layer (mask #3)   Top layer (mask #4)
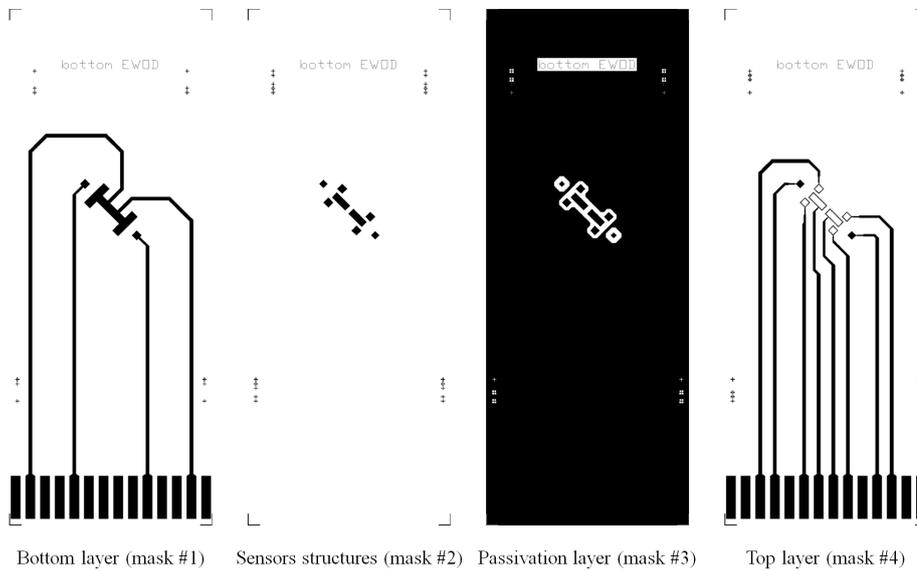
Figure 4.20. "Sensors chip" masks designed with AUTOCAD software.
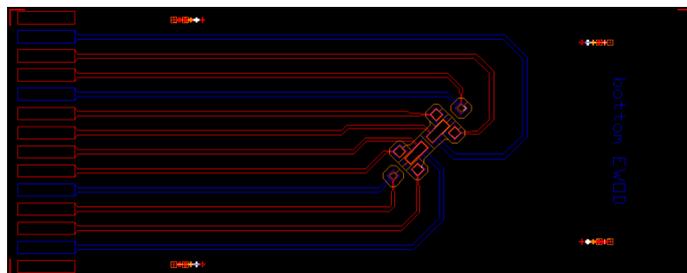
Figure 4.21. "Sensors chip" AUTOCAD interface showing all the layers used for the sensors fabrication.

Conclusions

Aim of this PhD thesis is the design and development of an ElectroWetting On Dielectrics (EWOD) based multifunctional platform which integrates, on the same lab-on-chip, three different modules for the microfluidics, sample treatment and detection. The project includes also the development of all the electronics, including firmware and software, needed to control the system.

The microfluidic module is based on the EWOD movement technique. Several integration problems have been taken into account, in particular those regarding the coupling of EWOD structure with other functional modules, such as light and temperature amorphous silicon sensors. In this context, a new electrowetting system has been designed and fabricated. In particular, the fabricated device is a two-glass microfluidic network composed of a central chamber and two reservoirs, either acting as inlet or outlet. The bottom substrate hosts the EWOD electrodes, while the microfluidic channel is fabricated on the surface of the top substrate, which includes also the common electrode and the hydrophobic layer. Then, top and bottom substrates are bonded together. Moreover, the achieved compact structure could host, on the external surfaces, the actuators and sensors needed to make several biochemical analyses.

Particular attention has been paid on the development of all the electronics needed to control the different functional modules of the system, such as the electronic board able to move droplets of liquid by means of the EWOD. The electronic board controls and interfaces the LoC with a computer and it is composed of three main parts connected in a compact and modular system: a switching board, that distributes through a microcontroller the voltage to the electrodes; a low-power high-voltage generator that generates the voltage to apply to the electrodes starting from the USB computer connection; an electronic circuit that localizes and quantifies the fluid droplets. Moreover, a graphical unit interface (GUI) has been developed in C++ to control all the parameters to be sent to the microcontroller through a USB connection.

In addition to the EWOD based microfluidic network, a thermal control module for the sample treatment including a LoC and the hardware, firmware and software of an electronic board able to precisely control thermal cycles of the system has been developed. The LoC integrates, on the same substrate, thin film heaters and temperature sensors, while the electronic board includes a set of electronic circuits that biases the diodes at constant current and reads the diode voltages, and a set of power circuits that drives the heater with the current required to achieve the specified temperature.

In order to obtain the setpoint temperature specified by the user through a

Graphic User Interface, the electronic board drives the heater using a software Proportional-Integral-Derivative auto-tuned algorithm, which takes, as input, the temperature inferred by the diodes and regulates the current of the heater to reach the desired setpoint.

Finally, regarding the detection module, in order to study biochemical application requiring the use of fluorescent dye, the design and development of a system combining a thin film interferential filter and light sensor placed on the same substrate have been carried out. The filter rejects the excitation light, while the photosensors absorb the re-emitted radiation. In this way, the system features a high miniaturization degree thanks to the on chip detection performed by the a-Si:H photosensors and, at the same time, avoids the use of focusing optics as a result of the reduced distance between the fluorescent and the detection sites.

In order to demonstrate the compatibility between filter and photosensors, the interferential filter has been designed for the detection of DNA. In particular, the ruthenium complex $[Ru(phen)_2(dppz)]^{2+}$ is used as DNA intercalating dye. The compatibility of the different technological steps to attain on the same glass substrate the photosensors and the filter determined the sequence, the selection of materials and the deposition parameters of the whole process. The electro-optical characterization of the photodiode, performed after the filter deposition, demonstrated the efficacy of the filter in reducing the excitation light and in presenting a very little attenuation of the ruthenium complex fluorescence.

The devices presented in this PhD thesis have been exploited in order to perform several experiments. In particular, the three-temperatures Polymerase Chain Reaction (PCR) technique for DNA amplification has been successfully implemented using the developed thermal system. The lab-on-chip (called DARWIN'S) utilized in this experiment contains thin film heaters and amorphous silicon diodes (acting as light and temperature sensors) and all the microfluidics needed to implement the PCR.

Using the same lab-on-chip, the Real-Time Isothermal PCR has also been achieved. In this experiment, the electronics suitable to the thermal control and the electronic able to acquire the photocurrents generated by the light sensors have been utilized in parallel.

Instead, the optical system has been tested using a buffer solution, a buffer solution of $[Ru(phen)_2(dppz)]^{2+}$ 0.1 mM, and a buffer solution containing both $[Ru(phen)_2(dppz)]^{2+}$ 0.1 mM and dsDNA 1.5 mM. The results show an increase of sensor photocurrent when dsDNA is present in the solution, demonstrating that the reported system is suitable for detecting the variation of the fluorescence intensity as the $[Ru(phen)_2(dppz)]^{2+}$ is intercalated within the dsDNA.

Moreover, the system has been used for the implementation of the Real-Time PCR integrating the thin film interferential filter with the DARWIN'S device. In particular, the system has been calibrated in order to quantify the increase of the current read by the photosensors as a function of dsDNA concentration.

Thanks to the encouraging results obtained so far, a final device including all the modules developed before has been designed.

As a future development of this PhD project, the fabrication and testing of this platform is aimed for the achievement of a "true" lab-on-chip biomolecular analysis system.

List of Publications

JOURNALS

1. D. Caputo, G. de Cesare, **N. Lovecchio**, A. Nascetti, E. Parisi, R. Scipinotti, "Polydimethylsiloxane material as hydrophobic and insulating layer in electro-wetting-on-dielectric systems", Microelectronics Journal, vol. 45, no. 12, pp. 1684–1690, 2014.

2. D. Caputo, A. de Angelis, **N. Lovecchio**, A. Nascetti, R. Scipinotti, G. de Cesare, "Amorphous silicon photosensors integrated in microfluidic structures as a technological demonstrator of a "true" Lab-on-Chip system". Sensing and Bio-Sensing Research, vol. 3, pp. 98–104, 2015.

3. G. Petrucci, D. Caputo, **N. Lovecchio**, F. Costantini, I. Legnini, I. Bozzoni, A. Nascetti, G. de Cesare, "Multifunctional System-on-Glass for Lab-on-Chip applications", Biosensors and Bioelectronics, vol. 93, pp. 315–321, 2017.

4. F. Costantini, G. Petrucci, **N. Lovecchio**, M. Nardecchia, A. Nascetti, G. de Cesare, L. Tedeschi, C. Domenici, A. Ruggi, P. Placidi, A. Scorzoni, D. Caputo, "Integrated Sensor System for DNA Amplification and Separation Based on Thin Film Technology", IEEE Transactions on Components, Packaging and Manufacturing Technology, 2018, article in press.

CONFERENCES

1. D. Caputo, G. de Cesare, **N. Lovecchio**, R. Scipinotti, A. Nascetti, "Electro-wetting-on-dielectric system based on polydimethylsiloxane", 5th IEEE International Workshop on In Advances in Sensors and Interfaces (IWASI), pp. 99–103, 2013.

2. **N. Lovecchio**, D. Caputo, A. Nascetti, G. Petrucci, M. Carpentiero, G. de Cesare, A. Zahra, "Drop position sensing in digital microfluidics based on capacitance measurement", 18th IEEE Conference on Sensors and Microsystems (AISEM), 2015.

3. A. Zahra, D. Caputo, A. Nascetti, G. Petrucci, **N. Lovecchio**, R. Scipinotti, G. de Cesare, "Thermally actuated microfluidic system for lab on chip applications", 18th IEEE Conference on Sensors and Microsystems (AISEM), 2015.

4. G. Petrucci, D. Caputo, A. Nascetti, **N. Lovecchio**, E. Parisi, S. Alameddine, G. de Cesare, A. Zahra, "Thermal characterization of thin film heater for lab-on-chip application", 18th IEEE Conference on Sensors and Microsystems (AISEM), 2015.

5. M. Nardecchia, **N. Lovecchio**, P. R. Llorca, D. Caputo, G. de Cesare, A. Nascetti, "2-D digital microfluidic system for droplet handling using Printed Circuit Board technology", 18th IEEE Conference on Sensors and Microsystems (AISEM), 2015.

6. **N. Lovecchio**, G. Petrucci, D. Caputo, S. Alameddine, M. Carpentiero, L. Martini, E. Parisi, G. de Cesare, A. Nascetti, "Thermal control system based on thin film heaters and amorphous silicon diodes", 6th IEEE International Workshop on In Advances in Sensors and Interfaces (IWASI), pp. 277–282, 2015.

7. M. Carpentiero, D. Caputo, J. Gambino, **N. Lovecchio**, G. de Cesare, A. Nascetti, "Array of differential photodiodes for thermal effects minimization in biomolecular analysis", 6th IEEE International Workshop on In Advances in Sensors and Interfaces (IWASI), pp. 17–20, 2015.

8. D. Caputo, F. Costantini, **N. Lovecchio**, V. Viri, M. Tucci, P. Mangiapane, A. Ruggi, A. Nascetti, G. de Cesare, "Highly miniaturized system for on-chip detection of DNA", 20th International Conference on Miniaturized Systems for Chemistry and Life Sciences (MicroTAS), 2016.

9. D. Caputo, E. Parisi, A. Nascetti, M. Mirasoli, M. Nardecchia, **N. Lovecchio**, G. Petrucci, A. Roda, G. de Cesare, "Integration of amorphous silicon balanced photodiodes and thin film heaters for biosensing application", Procedia Engineering, vol. 168, pp.1434–1437, 2016.

10. M. Nardecchia, E. Bellini, P.R. Llorca, D. Caprini, **N. Lovecchio**, G. Petrucci, D. Caputo, G. de Cesare, A. Nascetti, "Integration of capillarity and EWOD technologies for autonomous and low-power consumption micro-analytical systems", Procedia Engineering, vol. 168, pp.1370–1373, 2016.

11. **N. Lovecchio**, G. Sacco, G. Petrucci, V. Di Fiore, C. Toti, G. de Cesare, D. Caputo, M. Nardecchia, F. Costantini , A. Nascetti, "Integration of electrowetting technology inside an all-glass microfluidic network", 7th IEEE International Workshop on In Advances in Sensors and Interfaces (IWASI), pp. 224–227, 2017.

12. F. Costantini, G. Petrucci, **N. Lovecchio**, M. Nardecchia, V. Di Fiore, G. de Cesare, A. Nascetti, D. Caputo, A. Ruggi, P. Placidi, A. Scorzoni, L. Tedeschi, C. Domenici, "Lab-on-glass system for DNA treatments", 7th IEEE International Workshop on In Advances in Sensors and Interfaces (IWASI), pp. 241–245, 2017.

13. D. Caputo, G. Petrucci, V. Di Fiore, A. Buzzin, M. Nardecchia, L. Cevenini, E. Michelini, M. Mirasoli, A. Roda, **N. Lovecchio**, F. Costantini, A. Nascetti,

G. de Cesare, "Integrated system based on thin film technologies for cell-based bioluminescence assays", in Multidisciplinary Digital Publishing Institute Proceedings, vol. 1, no. 4, p. 513, 2017.

14. **N. Lovecchio**, D. Caputo, G. Petrucci, A. Nascetti, M. Nardecchia, F. Costantini, G. de Cesare, "Amorphous silicon temperature sensors integrated with thin film heaters for thermal treatments of biomolecules", Sensors, Springer Proceedings of the Third National Conference on Sensors (CNS), pp. 183–193, 2017.

15. M. Nardecchia, P. Rodríguez Llorca, G. de Cesare, D. Caputo, **N. Lovecchio**, A. Nascetti, "Design, fabrication and testing of a capillary microfluidic system with stop-and-go valves using ewod technology", Sensors, Springer Proceedings of the Third National Conference on Sensors (CNS), pp. 200–208, 2017.

16. G. Petrucci, **N. Lovecchio**, M. Nardecchia, C. Parrillo, F. Costantini, A. Nascetti, G. de Cesare, D. Caputo, "Enhancement in PDMS-based microfluidic network for on chip thermal treatment of biomolecules", 19th IEEE Conference on Sensors and Microsystems (AISEM), pp. 99–106, 2017.

17. **N. Lovecchio**, F. Costantini, V. Viri, M. Nardecchia, G. Petrucci, M. Tucci, P. Mangiapane, A. Nascetti, G. de Cesare, D. Caputo, "Optoelectronic system-on-glass for on-chip detection of fluorescence", 19th IEEE Conference on Sensors and Microsystems (AISEM), pp. 143–149, 2017.

18. M. Nardecchia, D. Paglialunga, G. Petrucci, **N. Lovecchio**, Costantini, G. de Cesare, D. Caputo, A. Nascetti, "Autonomuous microfluidic capillary network for on chip detection of chemiluminescence", 19th IEEE Conference on Sensors and Microsystems (AISEM), pp. 295–302, 2017, to be published.

19. A. Pietrelli, V. Ferrara, B. Allard, F.Buret, I. Bavasso, **N. Lovecchio**, F. Costantini, F. Khaled, "Microbial fuel cell: performance and applications", World Academy of Science, Engineering and Technology, International Journal of Energy and Power Engineering, 19th International Conference on Fuel Cell Technology (ICFCET), vol. 4, no. 11, 2017.

Bibliography

[1] Stephen C Jakeway, Andrew J de Mello, and Emma L Russell. Miniaturized total analysis systems for biological analysis. *Fresenius' journal of analytical chemistry*, 366(6):525–539, 2000.

[2] Petra S Dittrich, Kaoru Tachikawa, and Andreas Manz. Micro total analysis systems. latest advancements and trends. *Analytical chemistry*, 78(12):3887–3908, 2006.

[3] P Abgrall and AM Gue. Lab-on-chip technologies: making a microfluidic network and coupling it into a complete microsystem- a review. *Journal of Micromechanics and Microengineering*, 17(5):R15, 2007.

[4] D Caputo, G De Cesare, C Manetti, A Nascetti, and R Scipinotti. Smart thin layer chromatography plate. *Lab on a Chip*, 7(8):978–980, 2007.

[5] Jong Wook Hong and Stephen R Quake. Integrated nanoliter systems. *Nature biotechnology*, 21(10):1179–1183, 2003.

[6] Aaron R Hawkins and Holger Schmidt. *Handbook of optofluidics*. CRC Press, 2010.

[7] Christopher P Price, Larry J Kricka, et al. Improving healthcare accessibility through point-of-care technologies. *Clinical Chemistry*, 53(9):1665–1675, 2007.

[8] Andréas Manz, N Graber, and H áM Widmer. Miniaturized total chemical analysis systems: a novel concept for chemical sensing. *Sensors and actuators B: Chemical*, 1(1-6):244–248, 1990.

[9] Stephen R Quake and Axel Scherer. From micro-to nanofabrication with soft materials. *Science*, 290(5496):1536–1540, 2000.

[10] B-H Jo, Linda M Van Lerberghe, Kathleen M Motsegood, and David J Beebe. Three-dimensional micro-channel fabrication in polydimethylsiloxane (pdms) elastomer. *Journal of microelectromechanical systems*, 9(1):76–81, 2000.

[11] Janelle R Anderson, Daniel T Chiu, Rebecca J Jackman, Oksana Cherniavskaya, J Cooper McDonald, Hongkai Wu, Sue H Whitesides, and George M Whitesides. Fabrication of topologically complex three-dimensional microfluidic systems in pdms by rapid prototyping. *Analytical chemistry*, 72(14):3158–3164, 2000.

[12] Michael W Toepke and David J Beebe. Pdms absorption of small molecules and consequences in microfluidic applications. *Lab on a Chip*, 6(12):1484–1486, 2006.

[13] E Eteshola and D Leckband. Development and characterization of an elisa assay in pdms microfluidic channels. *Sensors and Actuators B: Chemical*, 72(2):129–133, 2001.

[14] Teruo Fujii. Pdms-based microfluidic devices for biomedical applications. *Microelectronic Engineering*, 61:907–914, 2002.

[15] Pierre-Alain Auroux, Dimitri Iossifidis, Darwin R Reyes, and Andreas Manz. Micro total analysis systems. 2. analytical standard operations and applications. *Analytical chemistry*, 74(12):2637–2652, 2002.

[16] Leslie Y Yeo, Hsueh-Chia Chang, Peggy PY Chan, and James R Friend. Microfluidic devices for bioapplications. *small*, 7(1):12–48, 2011.

[17] Vladimir Gubala, Leanne F Harris, Antonio J Ricco, Ming X Tan, and David E Williams. Point of care diagnostics: status and future. *Analytical chemistry*, 84(2):487–515, 2011.

[18] Mark A Burns, Brian N Johnson, Sundaresh N Brahmasandra, Kalyan Handique, James R Webster, Madhavi Krishnan, Timothy S Sammarco, Piu M Man, Darren Jones, Dylan Heldsinger, et al. An integrated nanoliter dna analysis device. *Science*, 282(5388):484–487, 1998.

[19] Anna J Tüdős, Geert AJ Besselink, and Richard BM Schasfoort. Trends in miniaturized total analysis systems for point-of-care testing in clinical chemistry. *Lab on a Chip*, 1(2):83–95, 2001.

[20] Andrea W Chow. Lab-on-a-chip: Opportunities for chemical engineering. *AIChE Journal*, 48(8):1590–1595, 2002.

[21] Soeren Schumacher, Jörg Nestler, Thomas Otto, Michael Wegener, Eva Ehrentreich-Förster, Dirk Michel, Kai Wunderlich, Silke Palzer, Kai Sohn, Achim Weber, et al. Highly-integrated lab-on-chip system for point-of-care multiparameter analysis. *Lab on a Chip*, 12(3):464–473, 2012.

[22] Tibor Chován and András Guttman. Microfabricated devices in biotechnology and biochemical processing. *TRENDS in Biotechnology*, 20(3):116–122, 2002.

[23] Katie M Horsman, Joan M Bienvenue, Kiev R Blasier, and James P Landers. Forensic dna analysis on microfluidic devices: a review. *Journal of forensic sciences*, 52(4):784–799, 2007.

[24] Vijay Srinivasan, Vamsee K Pamula, and Richard B Fair. An integrated digital microfluidic lab-on-a-chip for clinical diagnostics on human physiological fluids. *Lab on a Chip*, 4(4):310–315, 2004.

[25] Chong H Ahn, Jin-Woo Choi, Gregory Beaucage, Joseph H Nevin, Jeong-Bong Lee, Aniruddha Puntambekar, and Jae Y Lee. Disposable smart lab on a chip for point-of-care clinical diagnostics. *Proceedings of the IEEE*, 92(1):154–173, 2004.

[26] Mark B Romanowsky, Adam R Abate, Assaf Rotem, Christian Holtze, and David A Weitz. High throughput production of single core double emulsions in a parallelized microfluidic device. *Lab on a Chip*, 12(4):802–807, 2012.

[27] Patrick St-Louis. Status of point-of-care testing: promise, realities, and possibilities. *Clinical biochemistry*, 33(6):427–440, 2000.

[28] Marco Nardecchia, Enrica Bellini, Pablo R Llorca, Davide Caprini, Nicola Lovecchio, Giulia Petrucci, Domenico Caputo, Giampiero de Cesare, and Augusto Nascetti. Integration of capillary and ewod technologies for autonomous and low-power consumption micro-analytical systems. *Procedia Engineering*, 168:1370–1373, 2016.

[29] M Nardecchia, P Rodríguez Llorca, G de Cesare, D Caputo, N Lovecchio, and A Nascetti. Design, fabrication and testing of a capillary microfluidic system with stop-and-go valves using ewod technology. In *Convegno Nazionale Sensori*, pages 200–208. Springer, 2016.

[30] Stefan Haeberle and Roland Zengerle. Microfluidic platforms for lab-on-a-chip applications. *Lab on a Chip*, 7(9):1094–1110, 2007.

[31] Benjamin Shapiro, Hyejin Moon, Robin L Garrell, and Chang-Jin "CJ" Kim. Equilibrium behavior of sessile drops under surface tension, applied external fields, and material variations. *Journal of Applied Physics*, 93(9):5794–5811, 2003.

[32] Domenico Caputo, Giampiero De Cesare, Nicola Lovecchio, Riccardo Scipinotti, and Augusto Nascetti. Electrowetting-on-dielectric system based on polydimethylsiloxane. In *Advances in Sensors and Interfaces (IWASI), 2013 5th IEEE International Workshop on*, pages 99–103. IEEE, 2013.

[33] Domenico Caputo, Giampiero de Cesare, Nicola Lo Vecchio, Augusto Nascetti, Emanuele Parisi, and Riccardo Scipinotti. Polydimethylsiloxane material as hydrophobic and insulating layer in electrowetting-on-dielectric systems. *Microelectronics Journal*, 45(12):1684–1690, 2014.

[34] Marco Nardecchia, Nicola Lovecchio, and Pablo Rodriguez Llorca. 2-d digital microfluidic system for droplet handling using printed circuit board technology. In *AISEM Annual Conference, 2015 XVIII*, pages 1–4. IEEE, 2015.

[35] Richard B Fair. Digital microfluidics: is a true lab-on-a-chip possible? *Microfluidics and Nanofluidics*, 3(3):245–281, 2007.

[36] Frieder Mugele and Jean-Christophe Baret. Electrowetting: from basics to applications. *Journal of Physics: Condensed Matter*, 17(28):R705, 2005.

[37] Supin Chen, Muhammad Rashed Javed, Hee-Kwon Kim, Jack Lei, Mark Lazari, Gaurav J Shah, R Michael van Dam, Pei-Yuin Keng, et al. Radiolabelling diverse positron emission tomography (pet) tracers using a single digital microfluidic reactor chip. *Lab on a Chip*, 14(5):902–910, 2014.

[38] Yiyan Li, R Jacob Baker, and Dominic Raad. A highly efficient and reliable electrowetting on dielectric device for point-of-care diagnostics. In *Circuits and Systems Conference (DCAS), 2015 IEEE Dallas*, pages 1–4. IEEE, 2015.

[39] Michael G Pollack, Vamsee K Pamula, Vijay Srinivasan, and Allen E Eckhardt. Applications of electrowetting-based digital microfluidics in clinical diagnostics. *Expert review of molecular diagnostics*, 11(4):393–407, 2011.

[40] Yiyan Li, R Jacob Baker, and Dominic Raad. Improving the performance of electrowetting on dielectric microfluidics using piezoelectric top plate control. *Sensors and Actuators B: Chemical*, 229:63–74, 2016.

[41] Daniel Brassard, Lidija Malic, François Normandin, Maryam Tabrizian, and Teodor Veres. Water-oil core-shell droplets for electrowetting-based digital microfluidic devices. *Lab on a Chip*, 8(8):1342–1349, 2008.

[42] Nicola Lovecchio, Giulia Sacco, Giulia Petrucci, Valeria Di Fiore, Chiara Toti, Giampiero de Cesare, Domenico Caputo, Marco Nardecchia, Francesca Costantini, and Augusto Nascetti. Integration of electrowetting technology inside an all-glass microfluidic network. In *Advances in Sensors and Interfaces (IWASI), 2017 7th IEEE International Workshop on*, pages 224–227. IEEE, 2017.

[43] Sung Kwon Cho, Hyejin Moon, and Chang-Jin Kim. Creating, transporting, cutting, and merging liquid droplets by electrowetting-based actuation for digital microfluidic circuits. *Journal of microelectromechanical systems*, 12(1):70–80, 2003.

[44] Xiaoyu Hu, Marcel Mibus, Giovanni Zangari, Carl Knospe, and Michael L Reed. Interrogation of droplet configuration during electrowetting via impedance spectroscopy. *Journal of Microelectromechanical Systems*, 24(6):2092–2100, 2015.

[45] Hong Ren, Richard B Fair, and Micheal G Pollack. Automated on-chip droplet dispensing with volume control by electro-wetting actuation and capacitance metering. *Sensors and Actuators B: Chemical*, 98(2):319–327, 2004.

[46] Tsung-Min Hsieh, Ching-Hsing Luo, Fu-Chun Huang, Jung-Hao Wang, Liang-Ju Chien, and Gwo-Bin Lee. Enhancement of thermal uniformity for a microthermal cycler and its application for polymerase chain reaction. *Sensors and Actuators B: Chemical*, 130(2):848–856, 2008.

[47] Vincent Miralles, Axel Huerre, Florent Malloggi, and Marie-Caroline Jullien. A review of heating and temperature control in microfluidic systems: techniques and applications. *Diagnostics*, 3(1):33–67, 2013.

[48] F Costantini, G Petrucci, N Lovecchio, M Nardecchia, V Di Fiore, G de Cesare, A Nascetti, D Caputo, A Ruggi, L Tedeschi, et al. Lab-on-glass system for dna treatments. In *Advances in Sensors and Interfaces (IWASI), 2017 7th IEEE International Workshop on*, pages 241–245. IEEE, 2017.

[49] Alex IK Lao, Thomas MH Lee, I-Ming Hsing, and Nancy Y Ip. Precise temperature control of microfluidic chamber for gas and liquid phase reactions. *Sensors and Actuators A: Physical*, 84(1):11–17, 2000.

[50] Kazuhiko Tsutsumi, Akira Yamashita, and H Ohji. The experimental study of high tcr pt thin films for thermal sensors. In *Sensors, 2002. Proceedings of IEEE*, volume 2, pages 1002–1005. IEEE, 2002.

[51] A Scorzoni, M Tavernelli, P Placidi, P Valigi, and A Nascetti. Accurate analog temperature control of a thin film microheater on glass substrate for lab-on-chip applications. In *SENSORS, 2014 IEEE*, pages 1216–1219. IEEE, 2014.

[52] D Caputo, G De Cesare, A Nascetti, and R Scipinotti. a-si: H temperature sensor integrated in a thin film heater. *physica status solidi (a)*, 207(3):708–711, 2010.

[53] Domenico Caputo, Giampiero De Cesare, Massimo Nardini, Augusto Nascetti, and Riccardo Scipinotti. Monitoring of temperature distribution in a thin film heater by an array of a-si: H temperature sensors. *IEEE Sensors Journal*, 12(5):1209–1213, 2012.

[54] Domenico Caputo, Emanuele Parisi, Augusto Nascetti, Mara Mirasoli, Marco Nardecchia, Nicola Lovecchio, Giulia Petrucci, Francesca Costantini, Aldo Roda, and Giampiero de Cesare. Integration of amorphous silicon balanced photodiodes and thin film heaters for biosensing application. *Procedia Engineering*, 168:1434–1437, 2016.

[55] Nicola Lovecchio, Giulia Petrucci, Domenico Caputo, Samia Alameddine, Matteo Carpentiero, Luca Martini, Emanuele Parisi, Giampiero De Cesare, and Augusto Nascetti. Thermal control system based on thin film heaters and amorphous silicon diodes. In *Advances in Sensors and Interfaces (IWASI), 2015 6th IEEE International Workshop on*, pages 277–282. IEEE, 2015.

[56] Nicola Lovecchio, Domenico Caputo, Giulia Petrucci, Augusto Nascetti, Marco Nardecchia, Francesca Costantini, and Giampiero de Cesare. Amorphous silicon temperature sensors integrated with thin film heaters for thermal treatments of biomolecules. In *Convegno Nazionale Sensori*, pages 183–193. Springer, 2016.

[57] Giampiero De Cesare, Augusto Nascetti, and Domenico Caputo. Amorphous silicon pin structure acting as light and temperature sensor. *Sensors*, 15(6):12260–12272, 2015.

[58] Nuno Miguel Matos Pires, Tao Dong, Ulrik Hanke, and Nils Hoivik. Recent developments in optical detection technologies in lab-on-a-chip devices for biosensing applications. *Sensors*, 14(8):15458–15479, 2014.

[59] Domenico Caputo, Giampiero De Cesare, Luisa Stella Dolci, Mara Mirasoli, Augusto Nascetti, Aldo Roda, and Riccardo Scipinotti. Microfluidic chip with integrated a-si: H photodiodes for chemiluminescence-based bioassays. *IEEE Sensors Journal*, 13(7):2595–2602, 2013.

[60] Mara Mirasoli, Augusto Nascetti, Domenico Caputo, Martina Zangheri, Riccardo Scipinotti, Luca Cevenini, Giampiero De Cesare, and Aldo Roda. Multiwell cartridge with integrated array of amorphous silicon photosensors for chemiluminescence detection: development, characterization and comparison with cooled-ccd luminograph. *Analytical and bioanalytical chemistry*, 406(23):5645–5656, 2014.

[61] Domenico Caputo, Annalisa de Angelis, Nicola Lovecchio, Augusto Nascetti, Riccardo Scipinotti, and Giampiero de Cesare. Amorphous silicon photosensors integrated in microfluidic structures as a technological demonstrator of a "true" lab-on-chip system. *Sensing and Bio-Sensing Research*, 3:98–104, 2015.

[62] Matteo Carpentiero, Domenico Caputo, Juri Gambino, Nicola Lovecchio, Giampiero De Cesare, and Augusto Nascetti. Array of differential photodiodes for thermal effects minimization in biomolecular analysis. In *Advances in Sensors and Interfaces (IWASI), 2015 6th IEEE International Workshop on*, pages 17–20. IEEE, 2015.

[63] Francesca Costantini, Cristiana Sberna, Giulia Petrucci, Massimo Reverberi, Fabio Domenici, Corrado Fanelli, Cesare Manetti, Giampiero De Cesare, Maria DeRosa, Augusto Nascetti, et al. Aptamer-based sandwich assay for on chip detection of ochratoxin a by an array of amorphous silicon photosensors. *Sensors and Actuators B: Chemical*, 230:31–39, 2016.

[64] G De Cesare, A Nascetti, R Scipinotti, A Zahra, and D Caputo. On-chip detection performed by amorphous silicon balanced photosensor for lab-on chip application. *Sensing and Bio-Sensing Research*, 3:53–58, 2015.

[65] Jiseok Lim, Philipp Gruner, Manfred Konrad, and Jean-Christophe Baret. Micro-optical lens array for fluorescence detection in droplet-based microfluidics. *Lab on a Chip*, 13(8):1472–1475, 2013.

[66] Joshua W Parks, Michael A Olson, Jungkyu Kim, D Ozcelik, H Cai, R Carrion Jr, JL Patterson, RA Mathies, AR Hawkins, and H Schmidt. Integration of programmable microfluidics and on-chip fluorescence detection for biosensing applications. *Biomicrofluidics*, 8(5):054111, 2014.

[67] Gihan Ryu, Jingsong Huang, Oliver Hofmann, Claire A Walshe, Jasmine YY Sze, Gareth D McClean, Alan Mosley, Simon J Rattle, Donal DC Bradley, et al. Highly sensitive fluorescence detection system for microfluidic lab-on-a-chip. *Lab on a Chip*, 11(9):1664–1670, 2011.

[68] Qiang Xi, Dian-Ming Zhou, Ying-Ya Kan, Jia Ge, Zhen-Kun Wu, Ru-Qin Yu, and Jian-Hui Jiang. Highly sensitive and selective strategy for microrna

detection based on ws2 nanosheet mediated fluorescence quenching and duplex-specific nuclease signal amplification. *Analytical chemistry*, 86(3):1361–1365, 2014.

[69] Hongying Zhu, Serhan O Isikman, Onur Mudanyali, Alon Greenbaum, and Aydogan Ozcan. Optical imaging techniques for point-of-care diagnostics. *Lab on a Chip*, 13(1):51–67, 2013.

[70] SAM Martins, G Moulas, JRC Trabuco, GA Monteiro, V Chu, JP Conde, and DMF Prazeres. Monitoring intracellular calcium in response to gpcr activation using thin-film silicon photodiodes with integrated fluorescence filters. *Biosensors and Bioelectronics*, 52:232–238, 2014.

[71] Domenico Caputo, Francesca Costantini, Nicola Lovecchio, Vittorio Viri, Mario Tucci, Pietro Mangiapane, Albert Ruggi, Giulia Petrucci, Augusto Nascetti, and Giampiero de Cesare. Highly miniaturized system for on-chip detection of dna. In *20th International Conference on Miniaturized Systems for Chemistry and Life Sciences, MicroTAS 2016*. Chemical and Biological Microsystems Society, 2016.

[72] Philip Day, Andreas Manz, and Yonghao Zhang. *Microdroplet technology: principles and emerging applications in biology and chemistry*. Springer Science & Business Media, 2012.

[73] Francis EH Tay, Ciprian Iliescu, Ji Jing, and Jianmin Miao. Defect-free wet etching through pyrex glass using cr/au mask. *Microsystem technologies*, 12(10-11):935–939, 2006.

[74] Nicola Lovecchio, Domenico Caputo, Augusto Nascetti, Giulia Petrucci, Matteo Carpentiero, Giampiero De Cesare, and Andleeb Zahra. Drop position sensing in digital microfluidics based on capacitance measurement. In *AISEM Annual Conference, 2015 XVIII*, pages 1–4. IEEE, 2015.

[75] Karl Johan Åström and Tore Hägglund. *PID controllers: theory, design, and tuning*, volume 2. Isa Research Triangle Park, NC, 1995.

[76] Chang C Hang, Karl Johan Åström, and Weng Khuen Ho. Refinements of the ziegler–nichols tuning formula. *IEE Proceedings D (Control Theory and Applications)*, 138(2):111–118, 1991.

[77] Ming Ge, Min-Sen Chiu, and Qing-Guo Wang. Robust pid controller design via lmi approach. *Journal of process control*, 12(1):3–13, 2002.

[78] André Pomerleau, André Desbiens, Daniel Hodouin, et al. Development and evaluation of an auto-tuning and adaptive pid controller. *Automatica*, 32(1):71–82, 1996.

[79] Chanchal Dey and Rajani K Mudi. An improved auto-tuning scheme for pid controllers. *ISA transactions*, 48(4):396–409, 2009.

[80] Giulia Petrucci, Domenico Caputo, Nicola Lovecchio, Francesca Costantini, Ivano Legnini, Irene Bozzoni, Augusto Nascetti, and Giampiero de Cesare. Multifunctional system-on-glass for lab-on-chip applications. *Biosensors and Bioelectronics*, 93:315–321, 2017.

[81] Giulia Petrucci, Domenico Caputo, Augusto Nascetti, Nicola Lovecchio, Emanuele Parisi, Samia Alameddine, Giampiero de Cesare, and Andleeb Zahra. Thermal characterization of thin film heater for lab-on-chip application. In *AISEM Annual Conference, 2015 XVIII*, pages 1–4. IEEE, 2015.

[82] Andleeb Zahra, Domenico Caputo, Augusto Nascetti, Giulia Petrucci, Nicola Lovecchio, Riccardo Scipinotti, and Giampiero De Cesare. Thermally actuated microfluidic system for lab on chip applications. In *AISEM Annual Conference, 2015 XVIII*, pages 1–4. IEEE, 2015.

[83] Andrew W McKinley, Per Lincoln, and Eimer M Tuite. Sensitivity of [ru (phen) 2 dppz] 2+ light switch emission to ionic strength, temperature, and dna sequence and conformation. *Dalton Transactions*, 42(11):4081–4090, 2013.